APPENDIX IX

MATES V

FINAL REPORT

Regional Modeling Analyses

Table of Contents

Appendix IX

Regional Modeling Analyses

IX.1 Introduction

The MATES V regional modeling analysis is presented in Chapter 4 of the main report. This appendix provides the analyses to complement and support the regional modeling demonstration. These include characterization and validation of the meteorological input data, development of the MATES V modeling emissions inventory, development of boundary conditions, model performance, and risk analysis.

The Comprehensive Air Quality Model with Extensions enhanced with a reactive tracer modeling capability (CAMx RTRAC, Ramboll Environment and Health, 2018) provided the dispersion modeling platform and chemistry used to simulate annual impacts of both gaseous and aerosol toxic compounds in the Basin. The version of the RTRAC "probing tool" in CAMx used in the modeling simulations includes an air toxics chemistry module to treat the formation and destruction of reactive air toxic compounds.

Numerical modeling was conducted on a domain that includes Coachella Valley, the entire Orange and Los Angeles Counties and populated areas of Riverside and San Bernardino Counties (Figure IX-1-1). Compared to the MATES IV domain, the MATES V domain is extended further east by 40 kilometers. The 2016 Air Quality Management Plan (AQMP) is the basis for the toxics emissions inventory developed for MATES V with updates incorporated for several source categories. The 2018 inventory used for the MATES V modeling analysis is projected from the 2012 baseline emissions inventory in the 2016 AQMP for area and off-road sources while the point source emissions are based on the 2018 Annual Emissions Reports (AER). Emissions from ocean-going vessels (OGV) from the 2018 CARB SIP update (CARB, 2018) are used. On-road emissions are updated based on the latest CARB's on-road emissions model, EMFAC 2017 (CARB, 2017) and travel activity data from Southern California Association of Governments 2016 Regional Transportation Plan (SCAG, 2016).

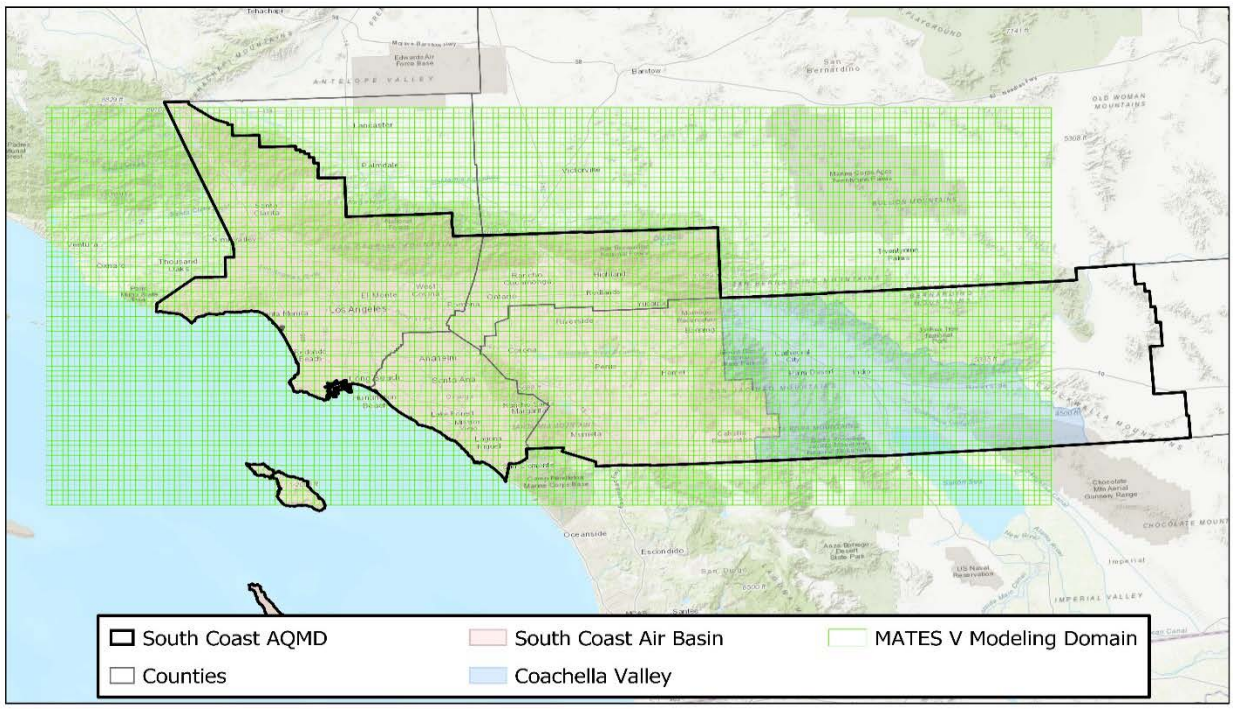

Figure IX-1-1.
MATES V Modeling Domain

Grid-based, hourly meteorological fields were generated from the Weather Research Forecast (WRF) mesoscale model (Skamarock, 2008). The National Centers for Environmental Prediction (NCEP) North American Regional Reanalysis (NARR) field was employed as initial and lateral boundary values for the WRF modeling. Four Dimensional Data Assimilation (FDDA) was conducted using grid analysis data, so the NARR data was enhanced with available surface and vertical sounding data. The WRF model was simulated for the period of May 1, 2018 to April 30, 2019, which provided the dispersion platform for the chemical transport modeling using CAMx.

IX.2 Background

The modeling system used for MATES air toxics cancer risk simulations has evolved over the past decades. The MATES II (South Coast AQMD, 2000) analysis used the Urban Airshed Model with TOX (UAMTOX) chemistry to simulate the advection and accumulation of toxic compound emissions throughout the Basin. UAMTOX was simulated for 2 km by 2 km grid domain that overlaid the Basin. The analysis relied on the 1997-1998 emissions projection from the 1997 AQMP and meteorological data fields for 1997-1998 generated from objective analysis using a diagnostic wind model. These tools were consistent with those used in both the 1997 and 2003 AQMP attainment demonstrations.

For the MATES III analysis (South Coast AQMD, 2007), the regional modeling dispersion platform and chemistry simulations progressed from the UAMTOX model to CAMx RTRAC. The second major change in the MATES III modeling analysis was the incorporation of the

Mesoscale Meteorological Model 5 (MM5, Grell, 1994) to drive the meteorological data simulation. At that time, MM5 was the state-of-the-art meteorological model used in numerous regional modeling analyses, worldwide. The transition to CAMx and MM5 was made based on suggestions from peer review for the 2003 AQMP modeling efforts.

The CAMx-MM5 modeling platform from MATES III was updated to the CAMx-WRF coupled system in MATES IV. The WRF, a state-of-the-science meteorological modeling tool, offers a variety of user options to cover atmospheric boundary layer parameterizations, turbulent diffusion, cumulus parameterizations, land surface-atmosphere interactions, which can be customized to specific geographical and climatological situations. South Coast AQMD performed extensive sensitivity tests and developments to improve the WRF performance for the South Coast Air Basin, of which geographical and climatological characteristics impose great challenges in predicting complex meteorological structures associated with air quality episodes.

MATES V simulations continued to rely on CAMx-WRF modeling system. Same as previous MATES, RTRAC algorithms available in CAMx continued to serve to track chemically active toxic elements individually to assess the contribution of each source category. The RTRAC algorithm provides a flexible approach for tracking the emission, dispersion, chemistry, and deposition of multiple gas- and particle-phase species that are not otherwise included in the model's chemistry mechanisms.

IX.3 Meteorological modeling

This section provides various analysis about meteorological conditions occurring during the MATES V study period compared to the MATES IV period and climatological average conditions. Detailed evaluation on WRF performance against available measurements were discussed as well.

IX.3.1 Comparison of observed meteorological elements during MATES V and past 20-year averages

The meteorological elements including annual average temperature, relative humidity, wind speed and annual total rain at 15 weather stations located in the region were used to evaluate weather patterns during the MATES V period with climatology using data from 2000 to 2019. The 15 weather stations are Los Angeles International Airport (LAX), Santa Monica Municipal Airport (SMO), Hawthorne Municipal Airport (HHR), Torrance Municipal Airport (TOA), Long Beach Airport (LGB), John Wayne Airport (SNA), Fullerton Municipal Airport (FUL), San Gabriel Valley Airport (EMT), Chino Airport (CNO), Ontario International Airport (ONT), Riverside Municipal Airport (RAL), March Air Reserve Base (RIV), Palm Springs International Airport (PSP), Burbank Bob Hope Airport (BUR) and (Van Nuys Airport) VNY. The results are shown in Figures IX-3-1 through IX-3-4.

As shown in Figure IX-3-1, the annual average temperatures during MATES V and the past 20-year average time periods are in reasonable agreement across most of the stations. The largest difference occurs at SMO station where the average temperature during MATES V period is ~0.8°C higher than the past 20-year average temperature. The second largest difference occurs at

VNY station with the MATES V average temperature being ~0.7°C higher than past 20-year average. The minimum difference is seen at HHR station with marginal difference between the two datasets (0.003°C). Of the 15 total stations, there are 5 stations (TOA, EMT, RAL, RIV and BUR) that show a lower temperature during MATES V compared to the past 20-year average.

As seen from Figure IX-3-2, most stations (11 out of 15 stations) have slightly higher relative humidity during the MATES V period compared to the past 20-year average. The largest annual average relative humidity (RH) difference between the two datasets occurs at BUR station where the MATES V period average is 6.6% higher than 20-year average; the minimum difference is seen at SMO station with 20-year average value being only 0.2% higher. The highest and lowest average relative humidity are at the LAX and PSP stations, respectively, according to both datasets.

The wind speed annual averages are also higher during MATES V period at most of the stations (11 out of 15). The ONT station shows the greatest difference where the MATES V average is 0.34 (m/s) higher than the past 20-year average (see Figure IX-3-3).

Among all the meteorological elements, the most notable difference between the two datasets appears to be related to total annual average rainfall (Figure IX-3-4). As shown in Figure IX-3-4, the average annual rainfall during the MATES V period is significantly higher than the 20-year average in all stations. These differences are due to unusually higher amounts of rain during the spring of 2019. The difference between the two datasets ranges from 2.6 inches at ONT station to 8.9 inches at CNO station.

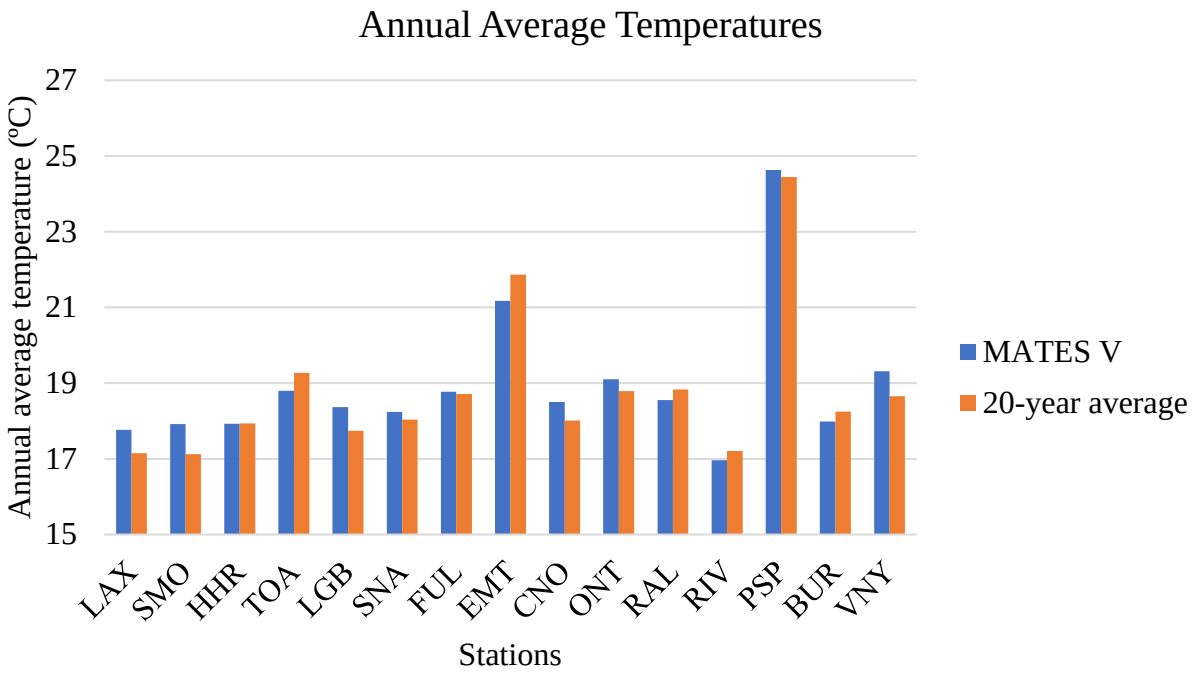

Figure IX-3-1.
Annual average temperature at each station during MATES V and past 20-year averages

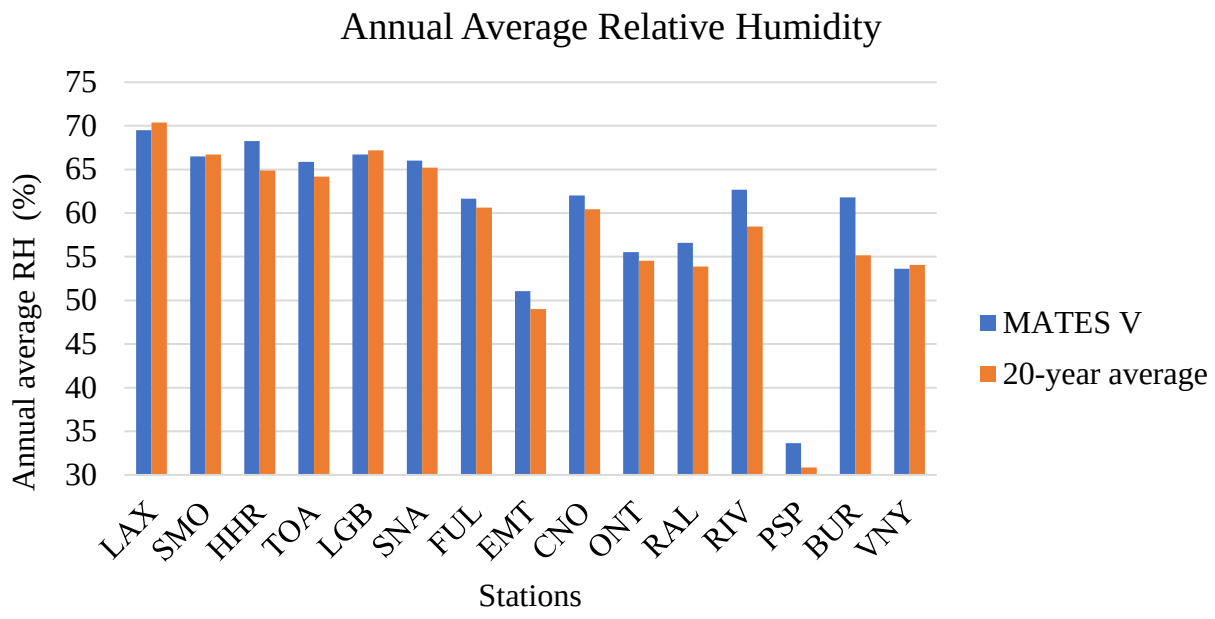

Figure IX-3-2.
Annual average relative humidity at each station during MATES V and past 20-year averages

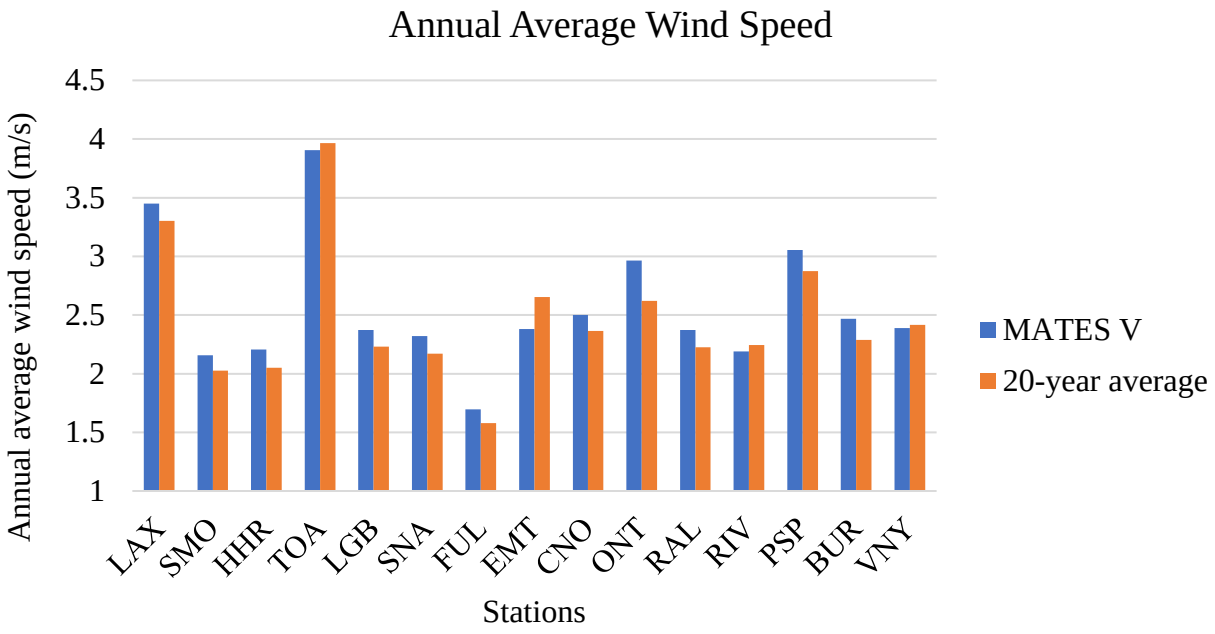

Figure IX-3-3.
Annual average wind speed at each station during MATES V and past 20-year averages

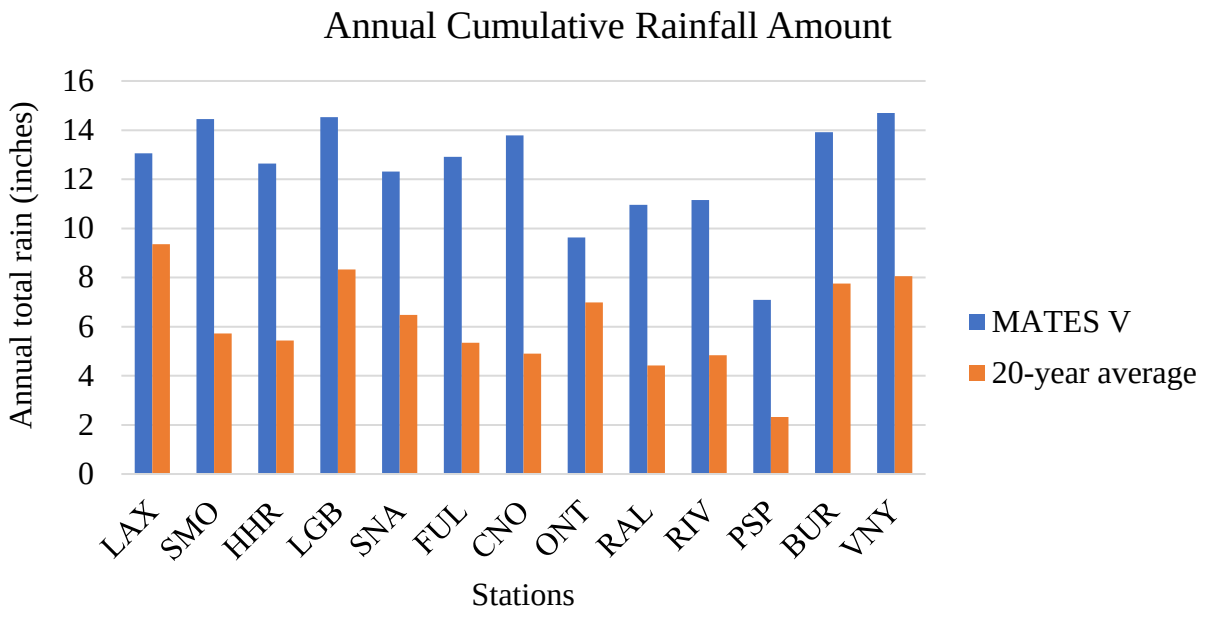

Figure IX-3-4.
Annual cumulative rainfall amount at each station during MATES V and past 20-year averages

IX.3.2 Comparison of meteorological fields between MATES IV and MATES V

Various meteorological parameter averages, including the annual average temperature, relative humidity (RH), wind speed and annual total rain at 15 weather stations in the South Coast Air Basin for the MATES IV and MATES V periods are shown in Figure IX-3-5 through IX-3-8. The MATES IV period (July 2012 through June 2013) is characterized as a dry year based on the observational data analysis in MATES IV report.

The largest difference between the MATES IV and MATES V period averages is related to annual total rain; the MATES V averages show higher values in all stations, as mentioned previously, due to the fact that an unusually high amount of rain occurred during spring 2019. The annual average temperature, annual average RH, and annual average wind speed values do not show significant differences between MATES IV and MATES V. The maximum difference in annual average temperature occurs at BUR station where MATES V is ~0.97 (°C) less than MATES IV. The maximum difference in annual RH occurs at BUR station where MATES V is 8.5 (%) higher than MATES IV. MATES IV averages show higher values for annual average wind speed at most of the stations (Figure IX-3-7); maximum difference occurs at ONT station with MATES V being 0.58 (m/s) higher than MATES IV.

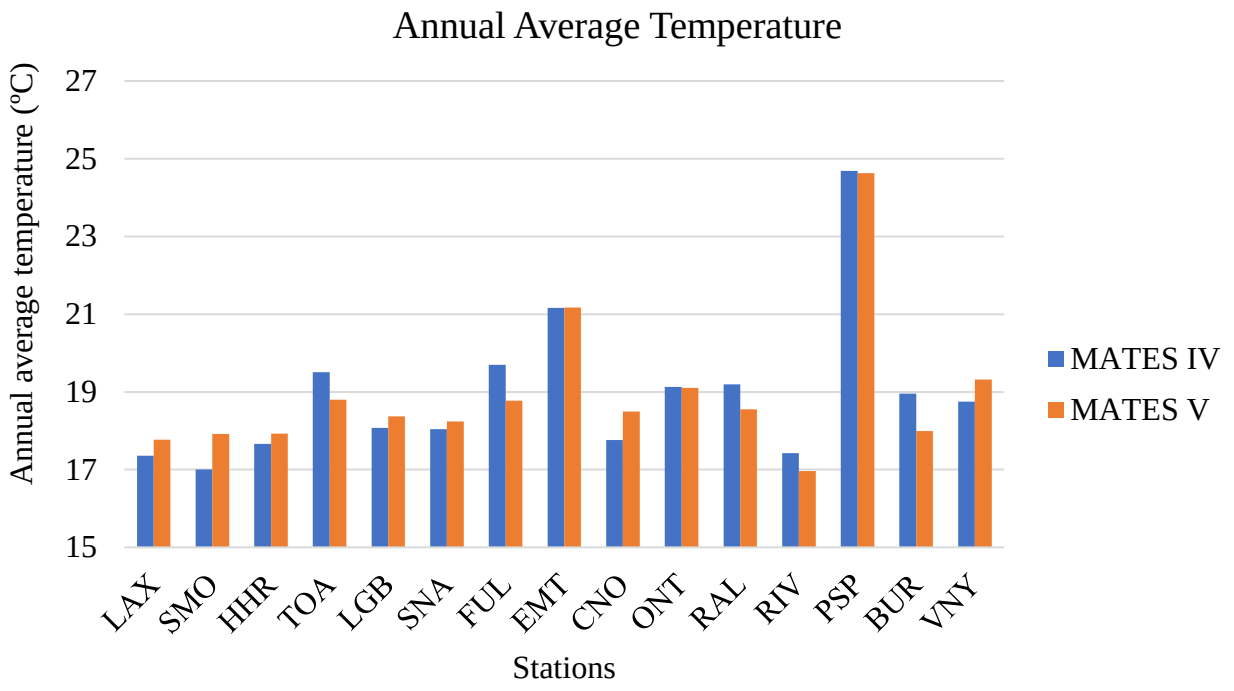

Figure IX-3-5
Annual average temperatures at each station during MATES IV and MATES V

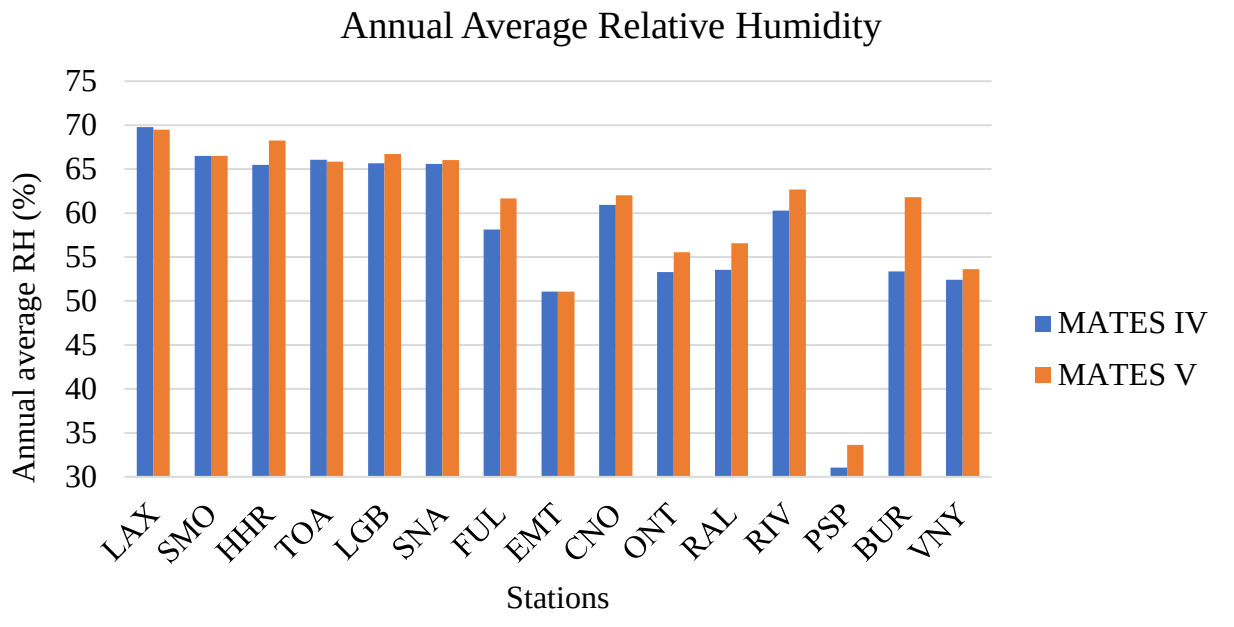

Figure IX-3-6
Annual average relative humidity at each station during MATES IV and MATES V

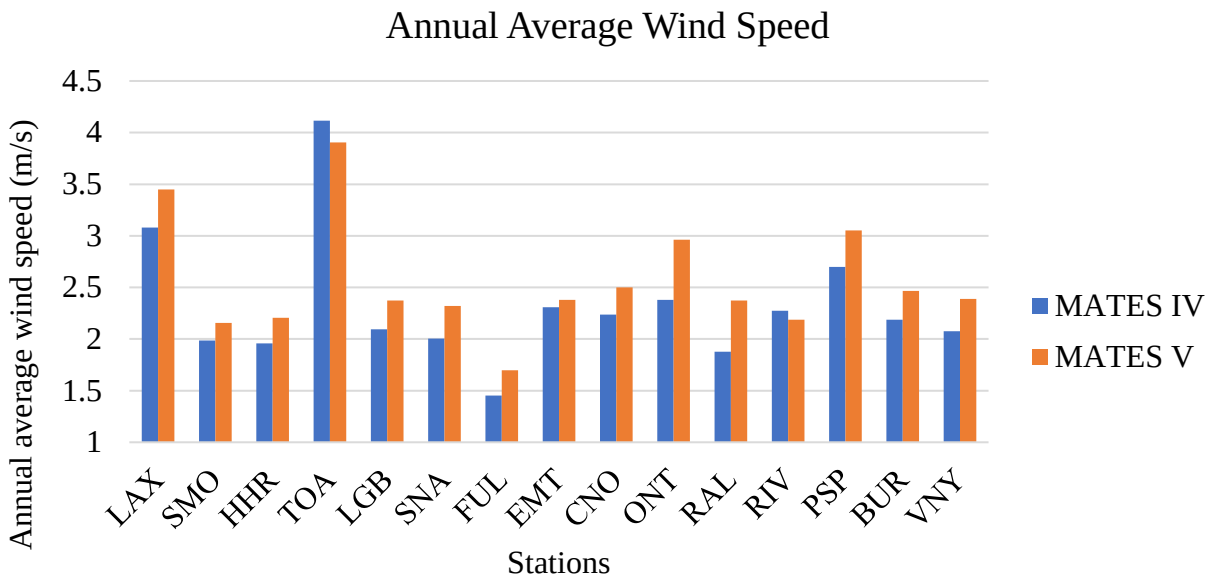

Figure IX-3-7
Annual average wind speed at each station during MATES IV and MATES V

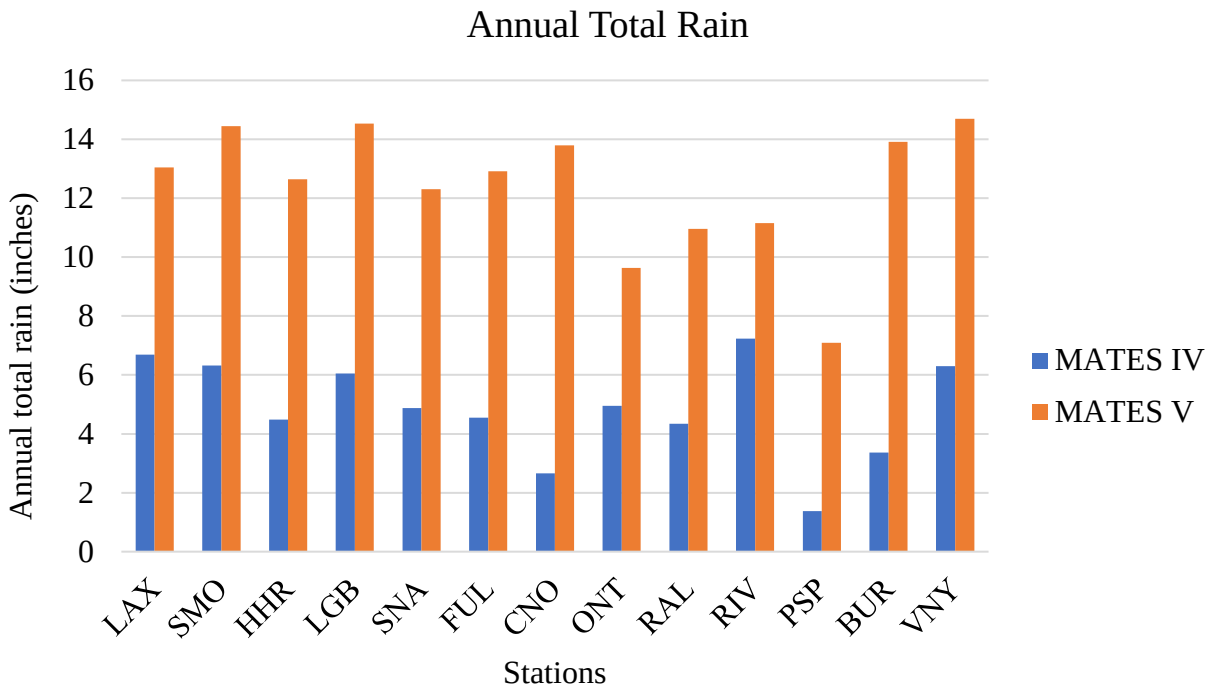

Figure IX-3-8
Annual total rain at each station during MATES IV and MATES V

IX.3.3 Weather Research and Forecasting (WRF) Numerical Model Configuration

The WRF model is one of the most widely used meteorological models that serves a wide range of meteorological applications across scales from tens of meters to thousands of kilometers. WRF has been applied to a wide range of phenomena, such as regional climate, monsoons, baroclinic waves, cyclones, mesoscale fronts, hurricane, deep convection, land-sea breezes, mountain-valley circulations, large eddy simulations, fire event, etc. The model has been in active development and it is a collaborative partnership of the National Center for Atmospheric Research (NCAR), the National Oceanic and Atmospheric Administration (represented by the National Centers for Environmental Prediction (NCEP) and the Earth System Research Laboratory), the U.S. Air Force, the Naval Research Laboratory, the University of Oklahoma, and the Federal Aviation Administration (FAA). The WRF system contains two dynamical solvers, referred to as the ARW (Advanced Research WRF) core and the NMM (Nonhydrostatic Mesoscale Model) core. The ARW configuration was chosen for the current modeling analyses. The ARW is primarily developed and maintained by the National Center for Atmospheric Research (NCAR) mesoscale and microscale meteorology laboratory.

The WRF model is a fully compressible and nonhydrostatic model (with a run-time hydrostatic option). Its vertical coordinate is selectable as either a terrain-following or hybrid vertical coordinate hydrostatic pressure coordinate. The grid staggering is the Arakawa C-grid. It uses a time-split small step for acoustic and gravity-wave mode. The dynamics conserves scaler variables. The WRF is designed to be a flexible, state-of-the-art atmospheric simulation system that is portable and efficient on parallel computing platforms.

The WRF simulation domain designed for the MATES V study encompasses the greater Los Angeles and suburban areas, its surrounding mountains, and the sea off the coast of the Basin, as shown in Figure IX-3-9. WRF simulations were conducted with four nested domains at grid resolutions of 36 km, 12 km, 4 km and 2 km. The innermost domain has 187 by 107 grid points in abscissa and ordinate, respectively, which spans 374km by 214 km in east-west and north-south directions, respectively. The figure also shows the relative locations and sizes of the four nested grids. The innermost domain presented in Figure IX-3-10, excluding three boundary columns and rows, served as the CAMx chemical transport modeling domain.

The WRF simulation employed 30 layers vertically with the lowest computational layer being approximately 20 m above ground level (agl) and the top layer at 50 hPa. Four Dimensional Data Assimilation (FDDA) was conducted using grid analysis data that was enhanced with available surface and vertical sounding data. The Sea Surface Temperature (SST) is a critical factor that drives the land-sea breeze and up-slope/down-slope flow. The SST data from the Global Data Assimilation Experiment (GODAE) are used to update the WRF modeling every 6 hours to better represent the sea surface temperature. The Yon-Sei University (YSU) scheme (Hong and Pan, 1996) was used to model the planetary boundary layer (PBL). The WRF simulation with this

configuration is referred as “control” simulation. The flowchart (Figure IX-3-11) of WRF simulation shows the meteorology input data, the processing steps, the observation nudging and the one-way nesting for high resolution inner domain.

After careful testing of different WRF physics options, the longwave radiation scheme of Rapid Radiative Transfer Model (RRTM), the shortwave radiation scheme of Dudhia and WRF Single-Moment 3-class scheme of micro physics were chosen for simulations. Kain-Fritsch cumulus schemes were employed to the outer three domains, while no cumulus parameterization was used for the innermost domain. The selections of the land surface model (LSM) scheme, the impacts of vertical and spatial resolution (1km) are discussed further in the next section.

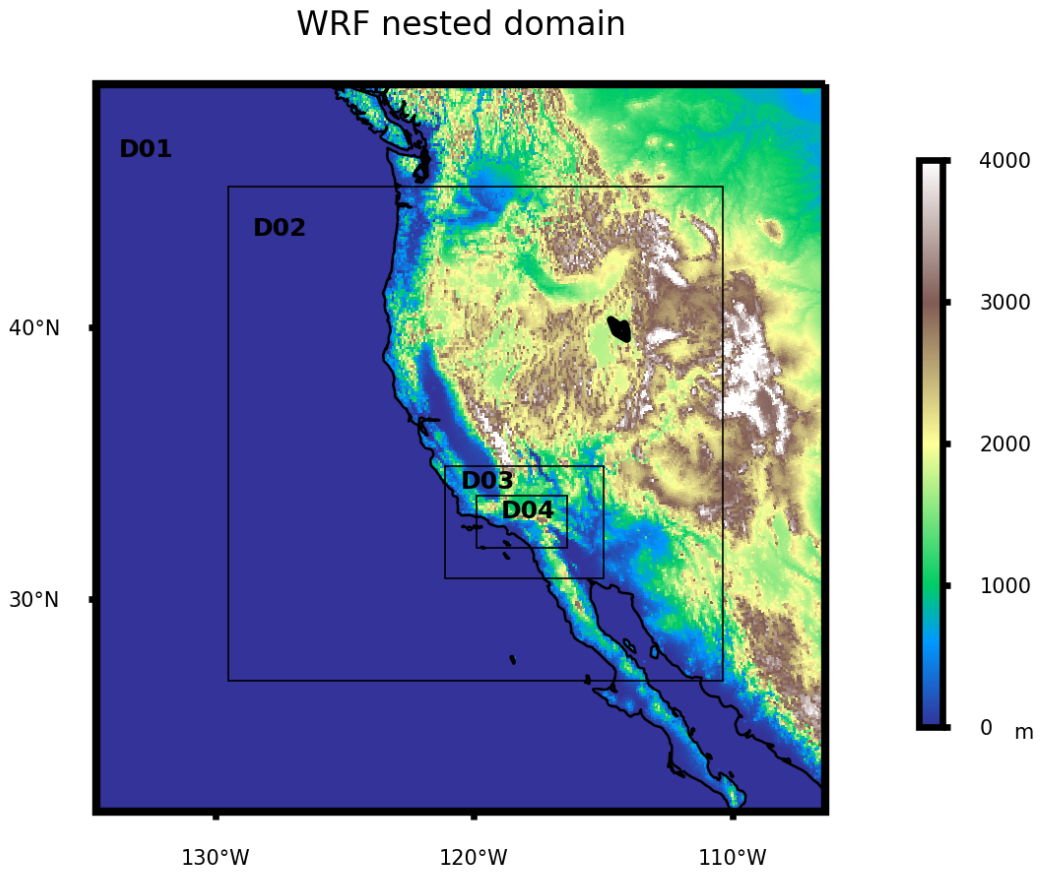

Figure IX-3-9
Four nested WRF modeling domains (36km, 12km, 4km, 2km horizontal resolution). Color scale represents topography

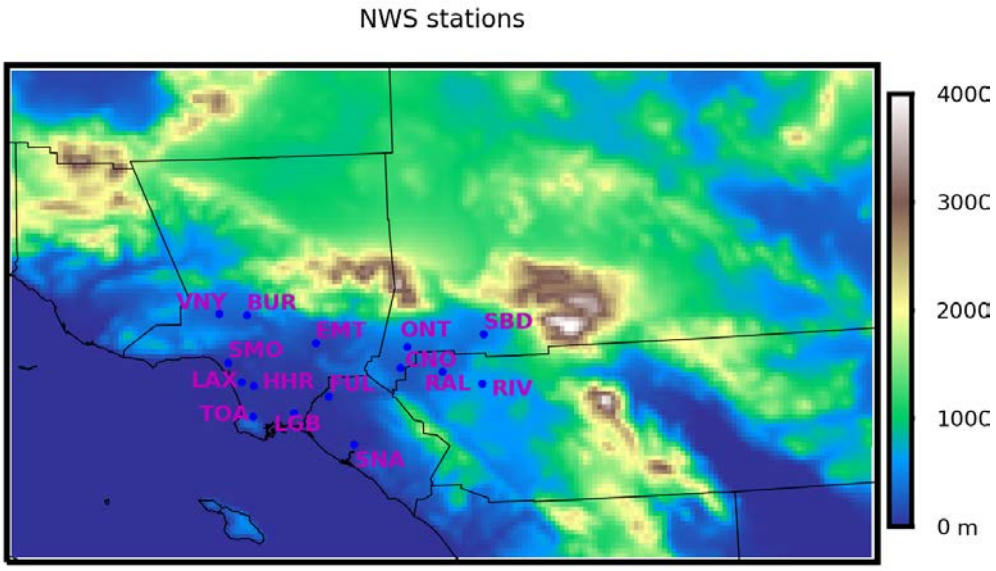

Figure IX-3-10
The inner most WRF simulation domain on the topographic map, and the 15 National Weather Service (NWS) stations used in the model performance evaluation

Table IX-3-1 below provides a summary of the WRF configuration used in MATES V in comparison with MATES IV. Major parameters finalized for MATES V are similar to those used in MATES IV. Sensitivity simulations were performed to evaluate land surface schemes and spatial and vertical resolutions of modeling configuration (Table IX-3-2). Those options identified as critical to describe air pollution episodes are presented.

Table IX-3-1

Overview of WRF configuration for MATES V in comparison with MATES IV

Component	MATES IV (July 2012-June 2013)	MATES V (May 2018-April 2019)
Numerical Platform	WRF version 3.4.1	WRF Version 4.0.3
Number of domains	4 nested domains	
Nested Domain setting	D01: 36 km (71 X 71)	D01: 36 km (83 X 83)
	D02: 12 km (133 X 133)	D02: 12 km (169 X 169)
	D03: 4 km (163 X 115)	
	D04: 2km (167 X 87)	D04: 2km (187 X 107)
Number of vertical layers	30 layers, the lowest layer is at ~ 20 m agl.	
Simulation Length	4 day with 24-hour spin-up	
Initial and boundary values	NCEP NAM* analysis (40 km X 40 km)	NCEP NARR# Re-analysis (32 km X 32 km)
Sea Surface Temperature	GHRSST+	
Boundary layer scheme	YSU (Yon-Sei University) scheme	
Land Surface model	Five-layer soil model	Unified Noah
Cumulus parameterization	Kain-Fritsch for the outer two domains Explicit for inner two domains	Kain-Fritschfor the outer three domains Explicit for the innermost domain
Micro physics	Simple ice	WRF Single-Moment 3-class
Radiation	Cloud radiation	RRTM scheme for longwave, Dudhia scheme for shortwave
Four-dimensional data analysis	Analysis nudging with NWS surface and upper air Measurements	

*NAM - The North American Mesoscale Forecast System
+GHRSST - The Group for High Resolution Sea Surface Temperature (https://www.ghrsst.org/)
#NARR - North American Regional Reanalysis

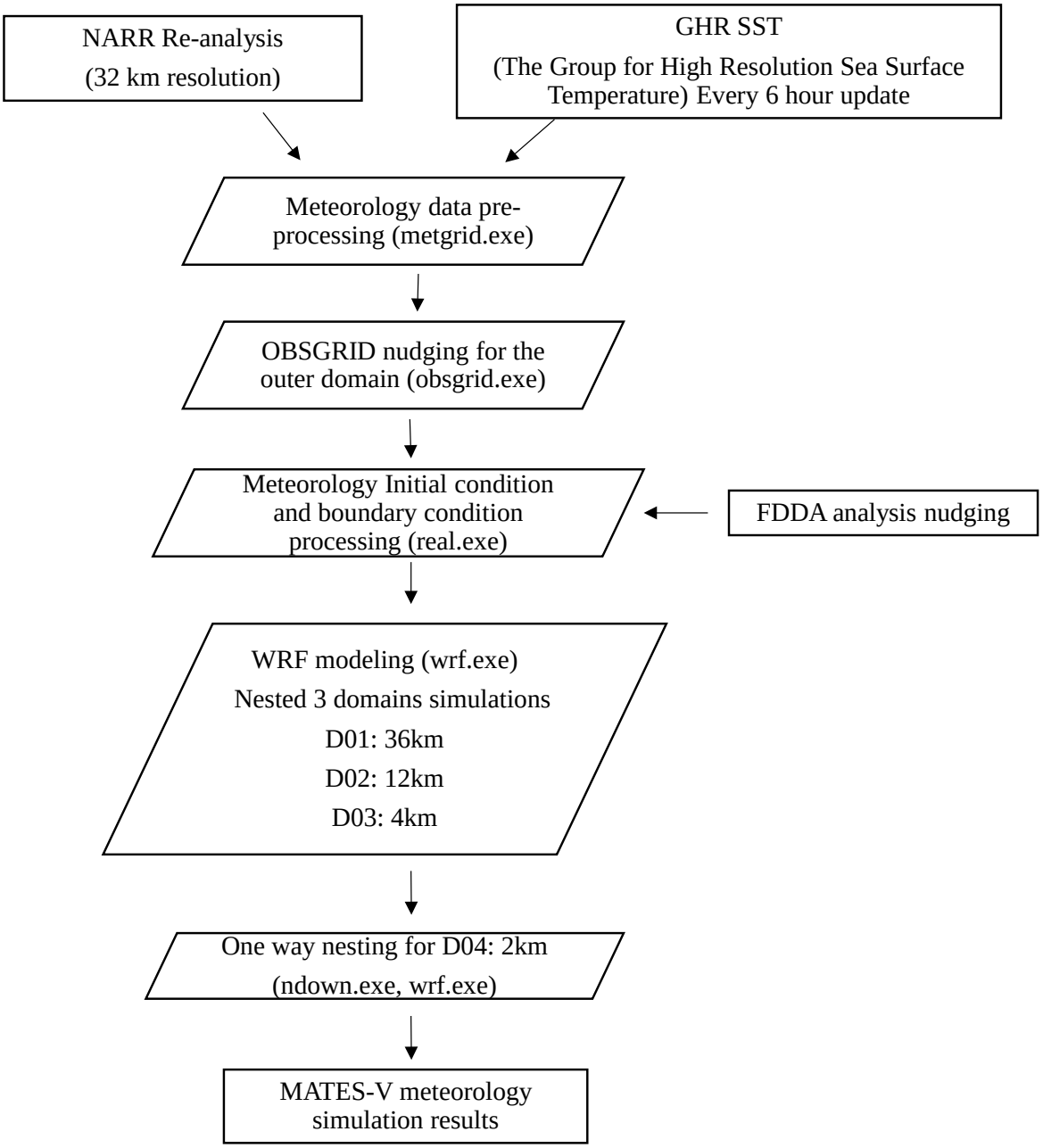

Figure IX-3-11
Flowchart of WRF simulation for MATES V

TABLE IX-3-1

The list of WRF sensitivity simulations

#	Testing Categories	Database
1	Land Surface Scheme	Pleim-Xiu land surface scheme
2	High Spatial Resolution	1km ×1km simulation*
3	High Vertical Resolution	35 layers in total, added 5 more layers between 0.8km – 3 km

*Considering the computational cost, only 4 month simulations (April 2018, July 2018, October 2018 and January 2019) were counducted

IX.3.4 Model Performance Evaluation of Metrological fields– Surface Level

The performance of the control simulations along with other sensitivity testing simulations are summarized in Table IX-3-3 and Table IX-3-4 for the summer season (June, July, and August of 2018) and winter season (December 2018, January and February 2019), respectively. All the results shown in Table IX-3-3 and IX-3-4 are averaged values for the 15 NWS stations. The locations of the NWS stations are shown in Figure IX-3-10. Overall, the WRF simulation for 2018 summer and winter provided representative meteorological fields that well characterized the observed conditions. These fields were used directly in the CAMx joint particulate and ozone simulations.

The performance of WRF control simulations used as transport fields for the CAMx modeling is provided in Figure IX-3-12 through Figure IX-3-20. The model performance was evaluated for each month at the airport stations in the model domain for May 2018 through April 2019. However, only one summer month (July) and one winter month (January) are shown here.

Three NWS stations are selected for surface level model performance evaluation: Hawthorne Municipal Airport (HHR, a coastal site), Fullerton Municipal Airport (FUL, an inland Orange County station), and Chino Airport (CNO, located in mid-Basin). The diurnal variation of temperature, humidity and surface wind are well represented by the WRF control simulations. Temperature and wind speed predictions are more accurate in the summer season than the winter months (Figure IX-12 – Figure IX-17). The observed temperature gradient from the coastal station of HHR to the inland station of CNO is well captured by the WRF model. During summer, the median temperature is 295, 300, and 305 K at HHR, FUL and CNO, respectively, from both WRF simulations and observations. For the inland stations of CNO and FUL, the WRF control simulations show slight underestimation of daily highest temperature during the days in July of 2018. At the near coast station of HHR, the WRF control simulation shows better performance in predicting daily highest values in summer.

During the winter month of January 2019, the WRF-simulated temperature values has better performance at the HHR station compare to the two other stations; the model performance at this

station during January 2019 (R = 0.89) is slightly better than in July 2019 (R = 0.87) as well. The model predictions of temperature at CNO and FUL stations during July 2019 are also better than the predictions during January 2019. The daily peak values are in better agreement with observations towards the end of the month of January 2019 at all stations; the model tends to overpredict the minimum values during this month.

The wind speed in summer shows distinct diurnal variation from both the WRF simulation and observation at all three stations with a strong sea breeze in the early afternoon. Daily maximum wind speed values show slight variations during the summer month of July 2019, unlike the winter month of January 2019 (e.g. from 2.5 to 12.5 m s^{-1} during January at CNO station). The model performance in predicting the wind speed is significantly better during summer month of July 2019 compared to the winter month of January 2019 at all stations; R values change from 0.82, 0.73, and 0.78 in July 2019, at CNO, FUL, and HHR stations, respectively, to 0.46,0.41,0.37 in January 2019. The model underestimates the daily peak wind speed values at the HHR station during the entire month of July 2019.

The WRF model has predicted the water vapor mixing ratio trends fairly well at all stations. The observations and predictions are in good agreement during winter with correlation coefficients of 0.83, 0.86, and 0.87 in January 2019 at CNO, FUL, and HHR stations, respectively; the corresponding values for the month of July are 0.61, 0.63, and 0.54. The WRF control run yields comparable magnitude of water vapor mixing ratio in summer without the general underestimation issue that occur in winter months. For both summer and winter months, the WRF control simulation did not capture a few episodes of sudden shift between dryness and wetness.

Table IX-3-3

WRF performance statistics for the seasonal average of June, July and August 2018 at 15 NWS stations

	Control	Pleim-Xiu Land Surface Scheme	High Spatial Resolution	High Vertical Resolution
2m Temperature Mean OBS (K)	299.1	299.1	299.1	299.1
2m Temperature Mean SIM (K)	297.6	297.7	298.9	297.5
2m Temperature Bias (K)	0.3	0.5	-0.1	0.3
2m Temperature Gross Error (K)	1.6	1.5	1.7	1.6
2m Temperature RMSE (K)	2.2	1.9	2.2	2.2
Water vapor mixing ratio Mean OBS (kg/kg)	11.2	11.2	11.2	11.2
Water vapor mixing ratio Mean SIM (kg/kg)	10.9	11.2	11.6	10.9
Water vapor mixing ratio Bias (kg/kg)	0.2	0.5	0.4	0.2
Water vapor mixing ratio Gross Error (kg/kg)	1.4	1.4	1.5	1.4

Water vapor mixing ratio RMSE (kg/kg)	2.4	2.4	2.6	2.4
Wind Speed Mean OBS (m/s)	2.8	2.8	2.8	2.8
Wind Speed Mean PRD (m/s)	2.4	2.4	2.5	2.4
Wind Speed Bias (m/s)	-0.3	-0.4	-0.3	-0.3
Wind Speed Gross Error (m/s)	1.1	1.1	1.2	1.1
Wind Speed RMSE (m/s)	1.5	1.4	1.5	1.5

Table IX-3-4

WRF performance statistics for the seasonal average of December 2018, and January and February 2019 at 15 NWS stations

	Control	Pleim Xiu	High Spatial resolution	High Vertical resolution
2m Temperature Mean OBS (K)	286.7	286.7	286.7	286.7
2m Temperature Mean SIM (K)	286	285	286.5	286
2m Temperature Bias (K)	0	-1	-0.2	0
2m Temperature Gross Error (K)	1.7	1.9	1.9	1.7
2m Temperature RMSE (K)	2.2	2.4	2.5	2.2
Water vapor mixing ratio Mean OBS (kg/kg)	5.9	5.9	5.9	5.9
Water vapor mixing ratio Mean SIM (kg/kg)	4.8	5.2	5	4.9
Water vapor mixing ratio Bias (kg/kg)	-0.8	-0.4	-0.9	-0.7
Water vapor mixing ratio Gross Error (kg/kg)	1.2	1.2	1.2	1.2
Water vapor mixing ratio RMSE (kg/kg)	1.7	1.7	1.6	1.7
Wind Speed Mean OBS (m/s)	2.1	2.1	2.1	2.1
Wind Speed Mean PRD (m/s)	2.1	1.9	2	2.1
Wind Speed Bias (m/s)	0	-0.1	0	0
Wind Speed Gross Error (m/s)	1.4	1.4	1.5	1.5
Wind Speed RMSE (m/s)	1.9	1.9	2	1.9

[*]To save computing time, only 4 month simulations – April 2018, July 2018, October 2018 and January 2019 are counducted for the WRF simulation with 1 X 1 km.

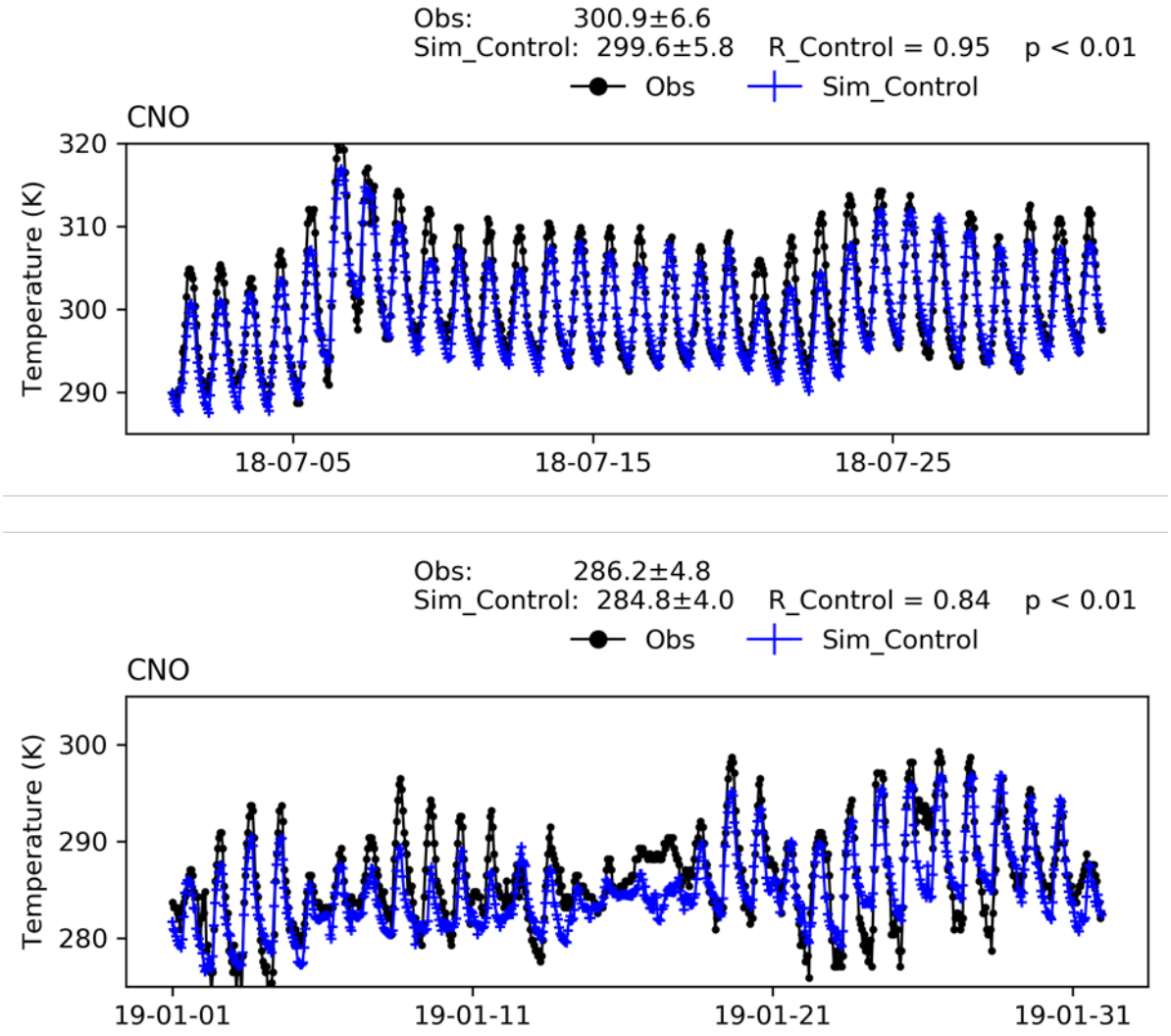

Figure IX-3-12

Time series of hourly temperature from measurement and WRF control simulations at Chino (CNO) station for July 2018 and January 2019

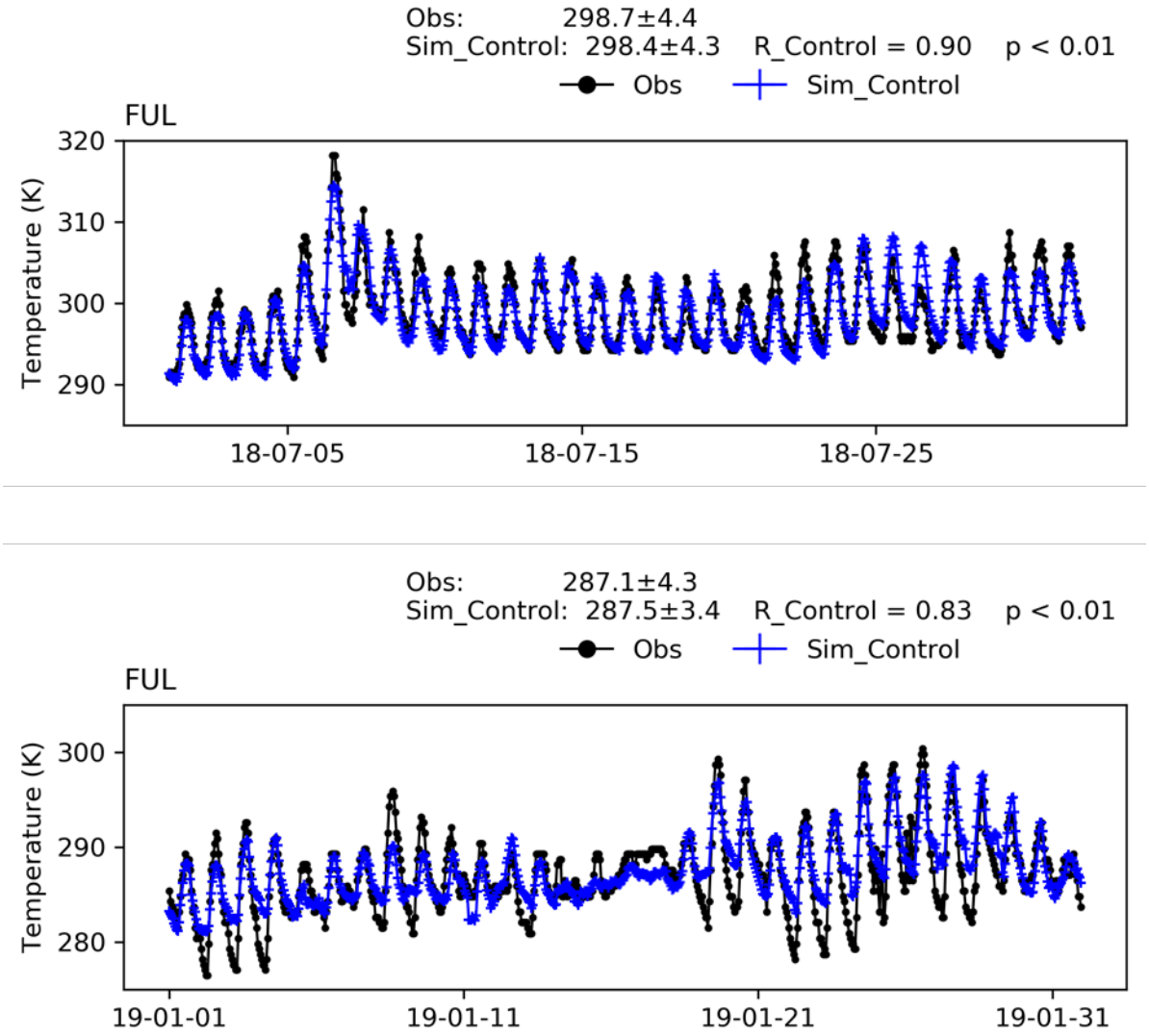

Figure IX-3-13

Time series of hourly temperature from measurements and WRF control simulations at Fullerton (FUL) station for July 2018 and January 2019

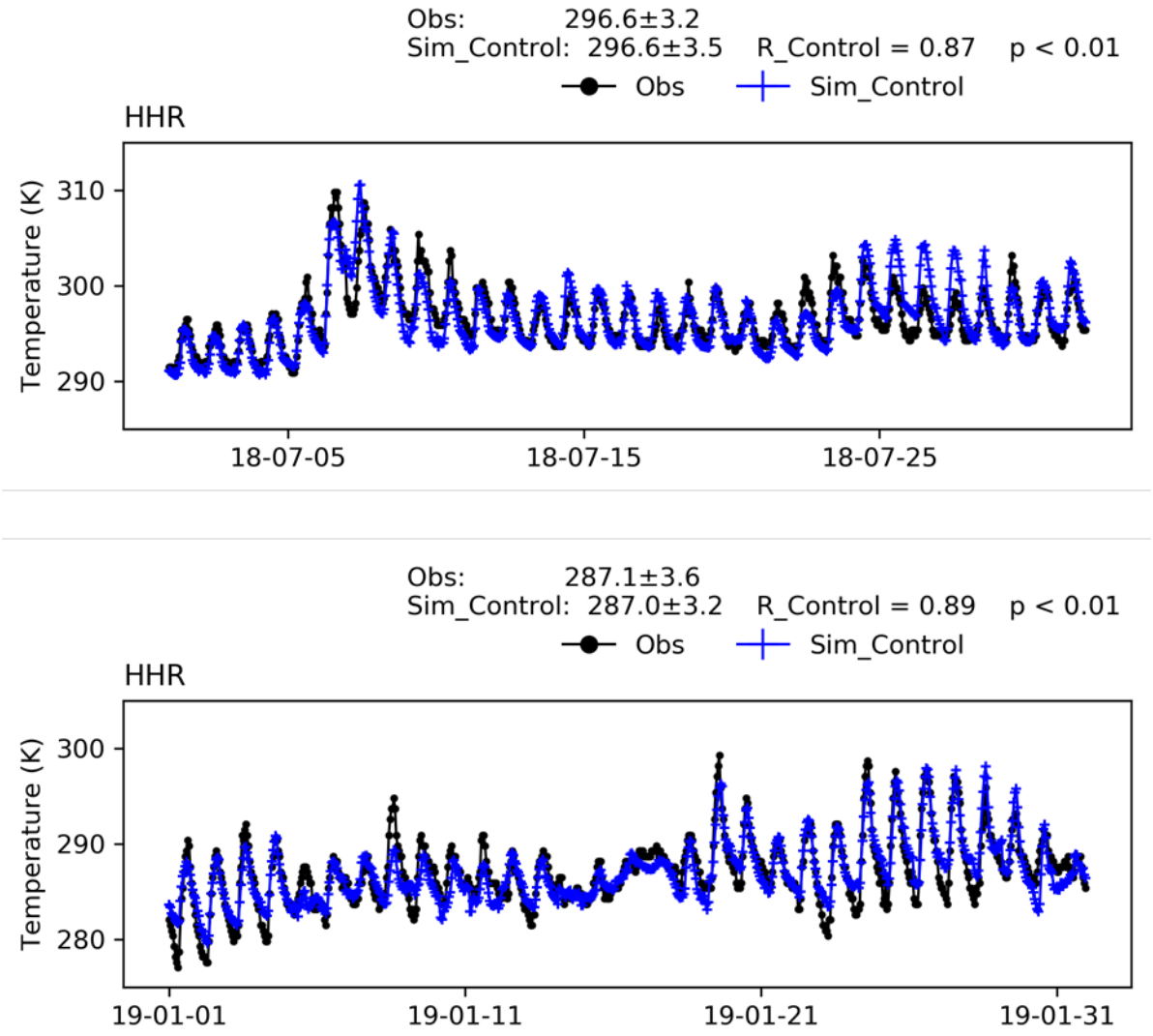

Figure IX-3-14

Time series of hourly temperature from measurements and WRF control simulations at Hawthorne (HHR) station for July 2018 and January 2019

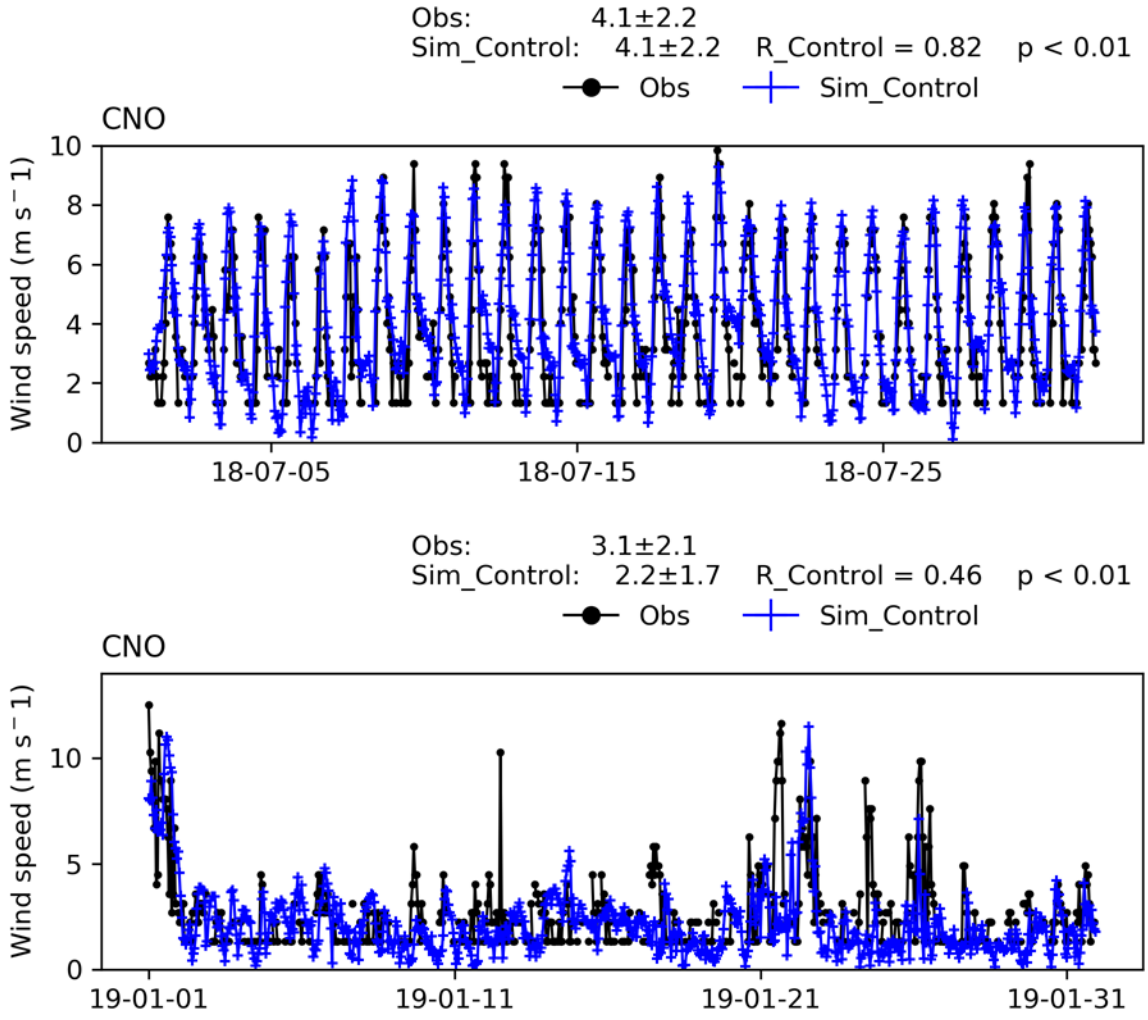

Figure IX-3-15

Time series of hourly wind speed from measurements and WRF control simulations at Chino (CNO) station for July 2018 and January 2019

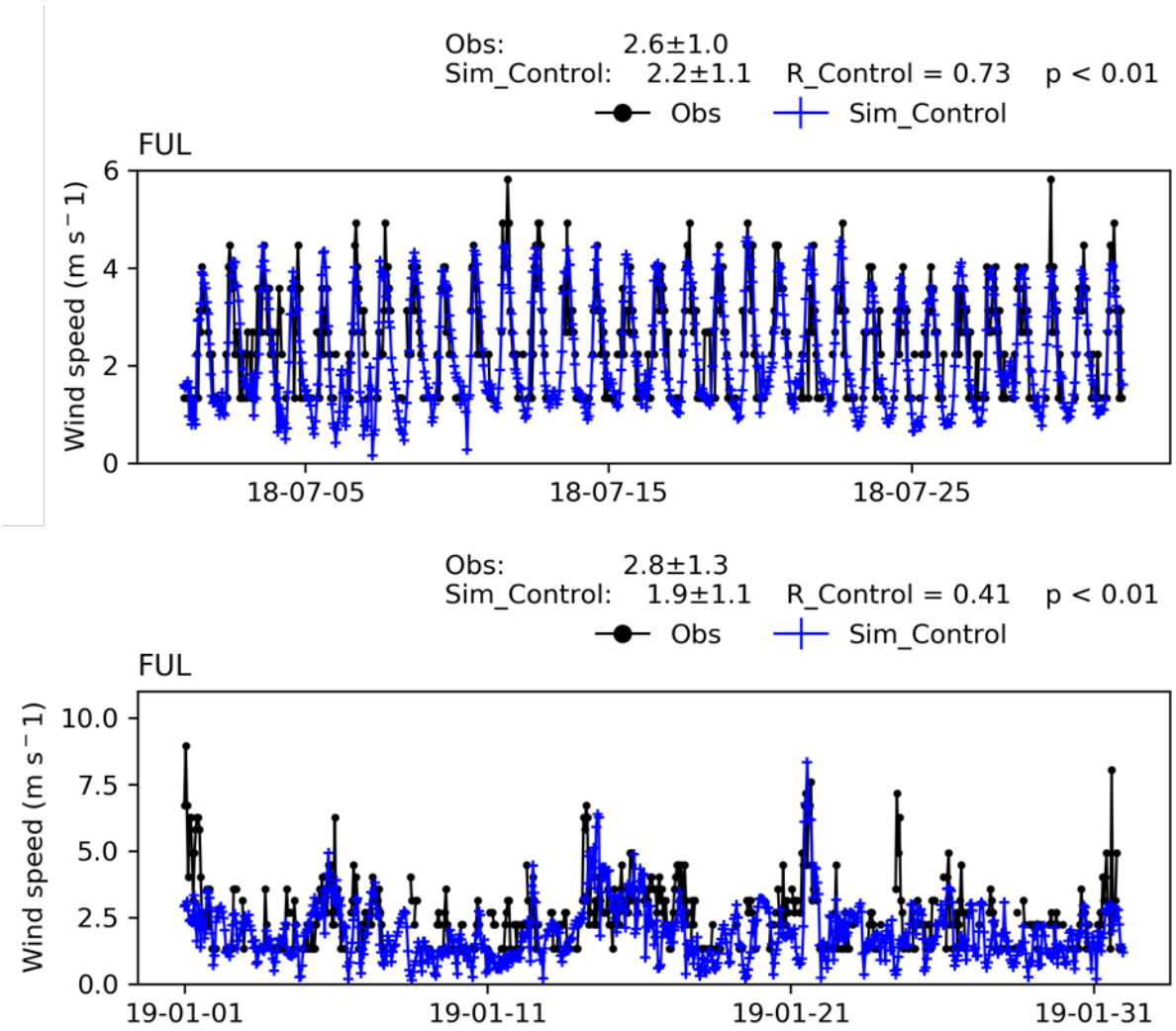

Figure IX-3-16

Time series of hourly wind speed from measurements and WRF control simulations at Fullerton (FUL) station for July 2018 and January 2019

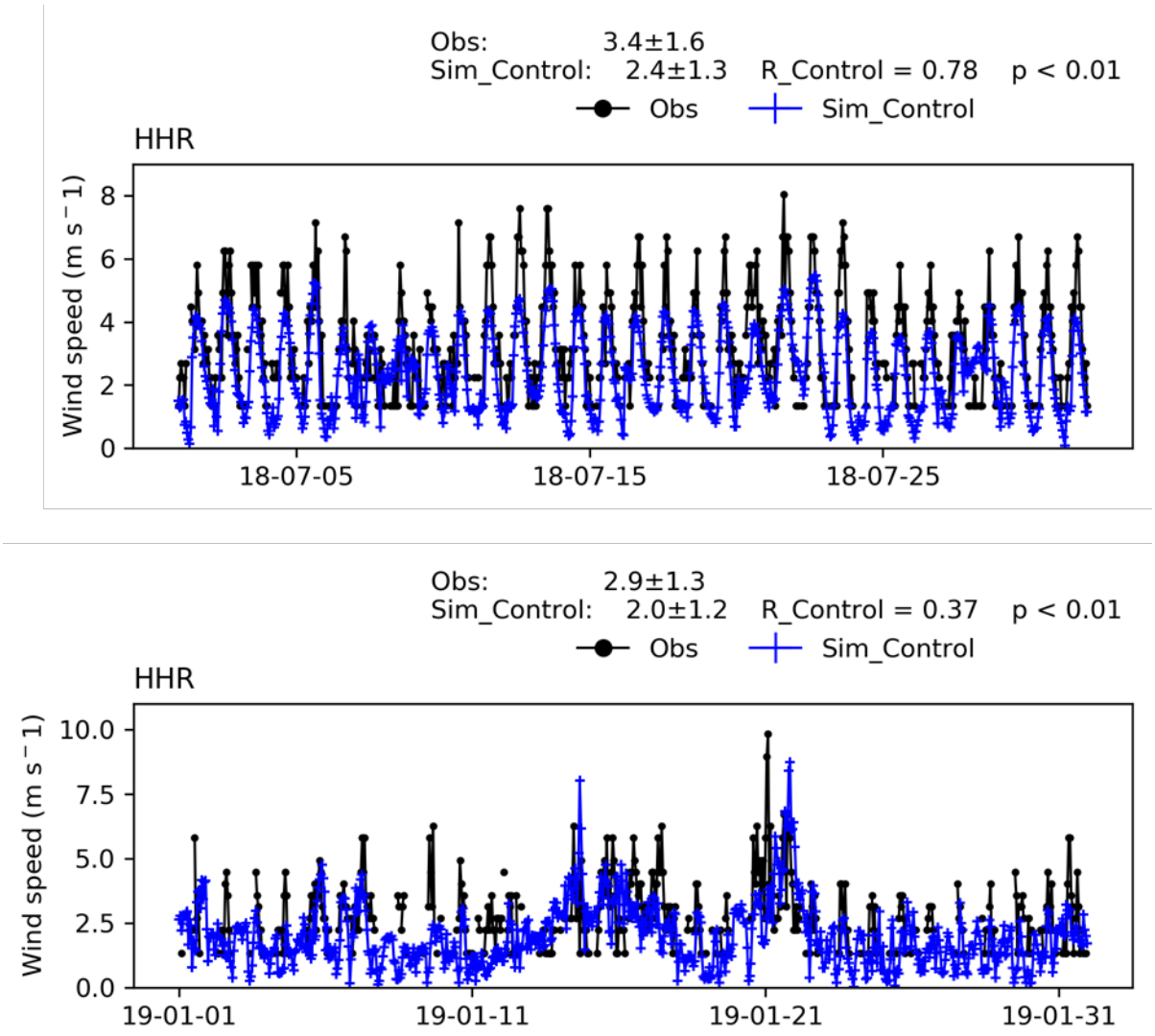

Figure IX-3-17

Time series of hourly wind speed from measurements and WRF control simulations at Hawthorne (HHR) station for July 2018 and January 2019

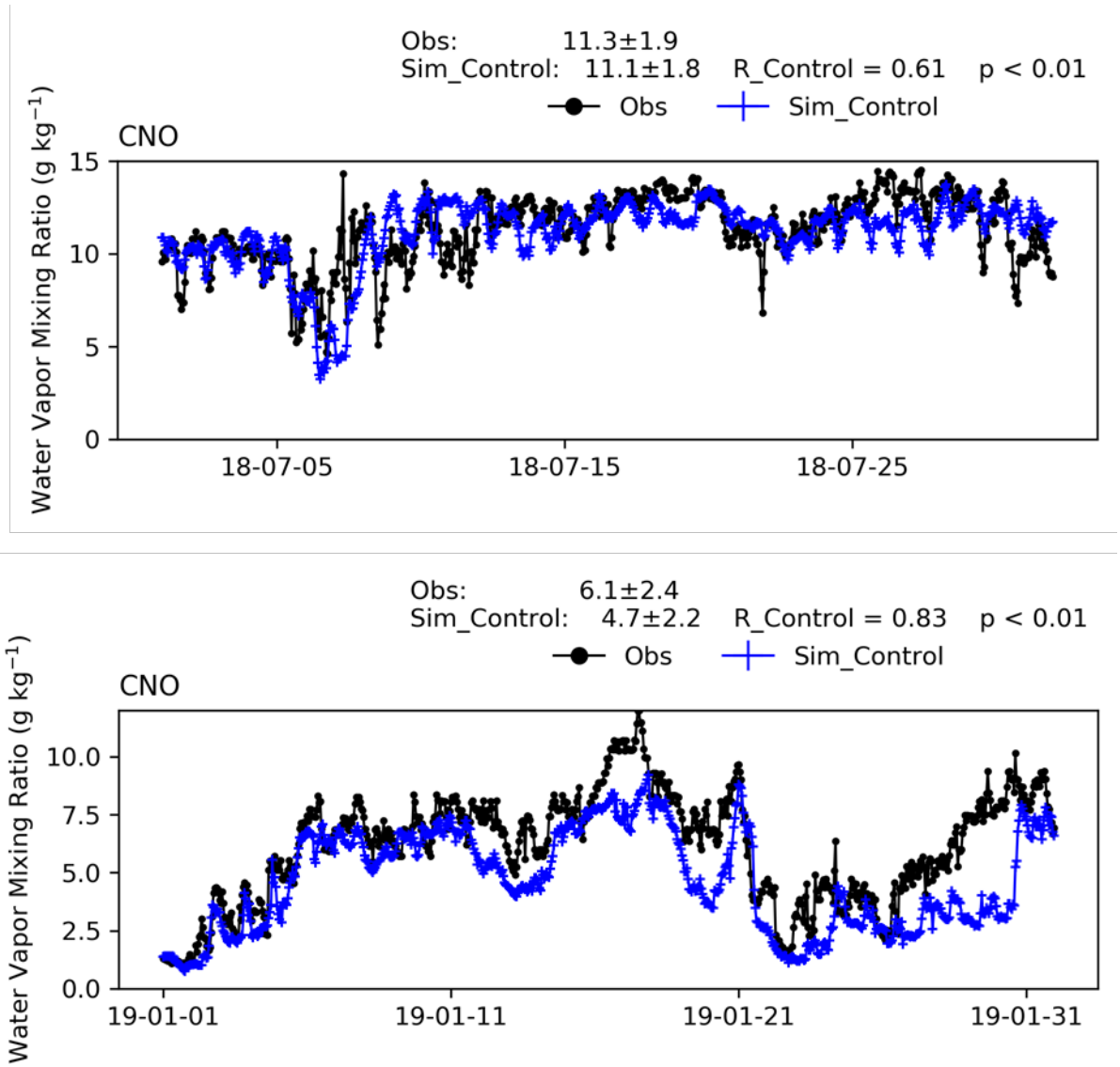

Figure IX-3-18

Time series of hourly water vapor mixing ratio from measurements and WRF control simulations at Chino (CNO) station for July 2018 and January 2019

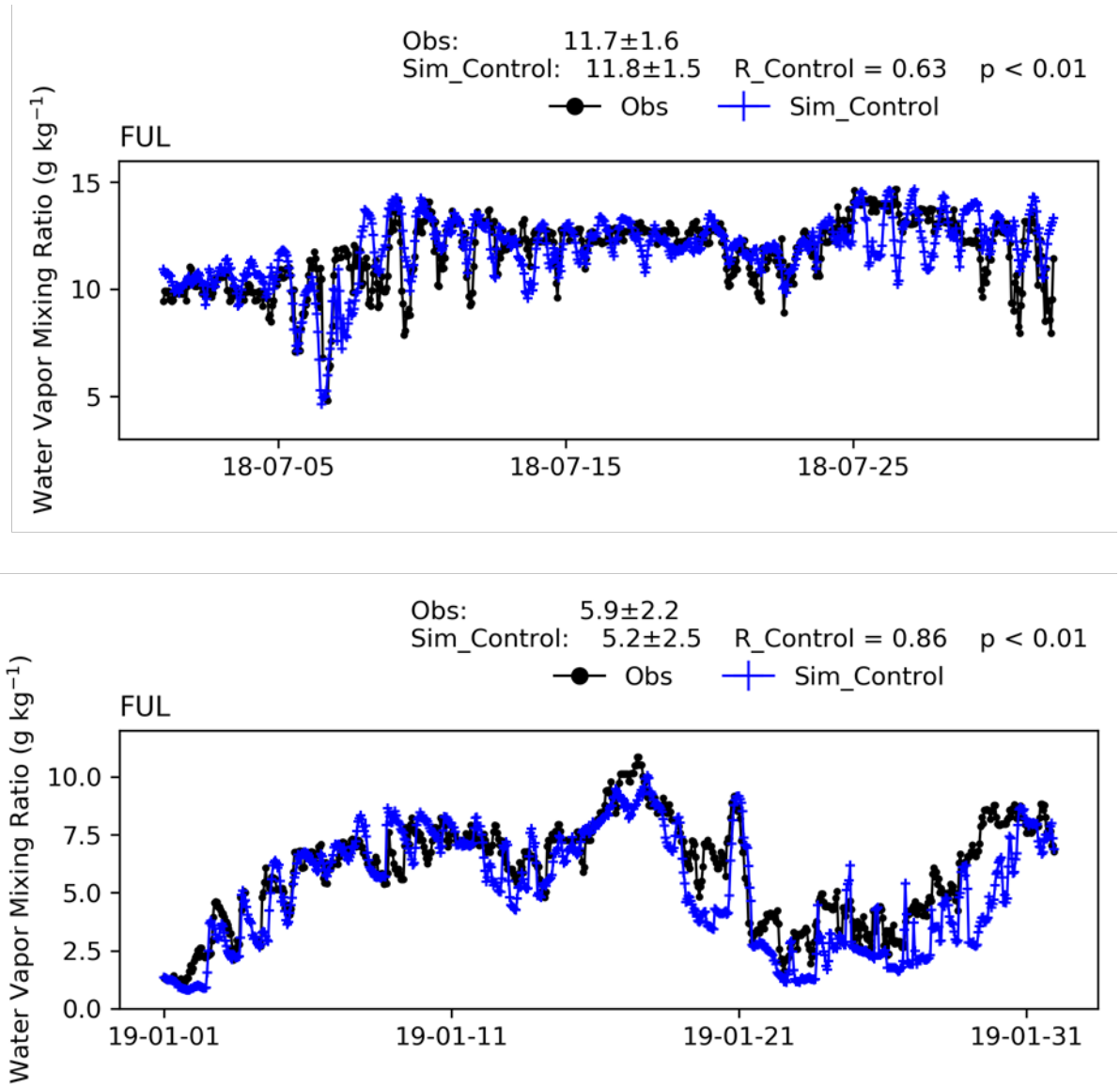

Figure IX-3-19

Time series of hourly water vapor mixing ratio from measurements and WRF control simulations at Fullerton (FUL) station for July 2018 and January 2019

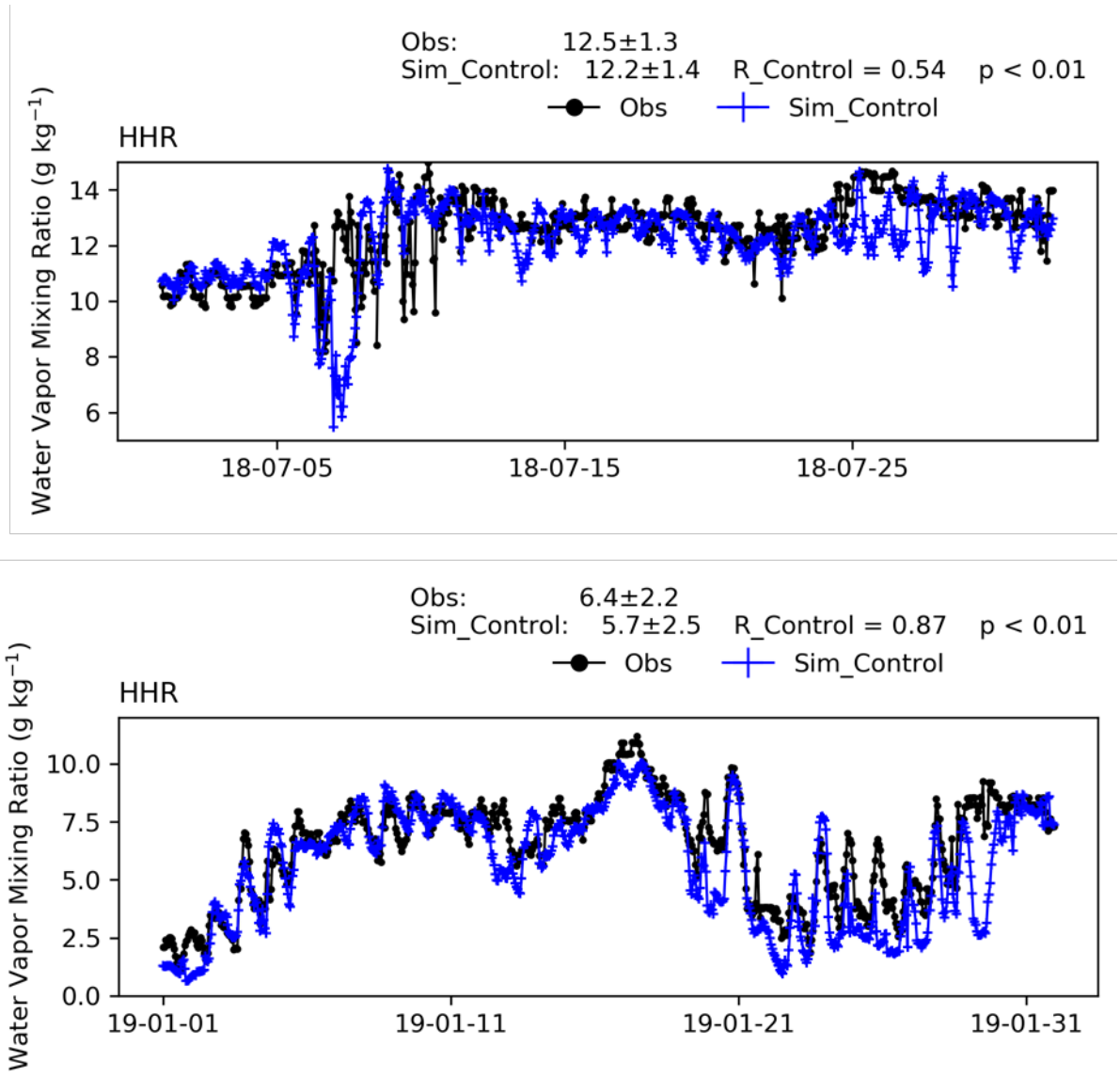

Figure IX-3-20

Time series of hourly water vapor mixing ratio from measurements and WRF control simulations at Hawthorne (HHR) station for July 2018 and January 2019

IX.3.5 Model Performance Evaluation of Meteorological fields – Diurnal variations

Monthly average diurnal variations of simulated temperature and water vapor mixing ratio were compared against measurements at three locations as provided in Figures IX-3-21 - IX-3-22. The seasonal differences between summer and winter, as represented by July and January, respectively, and the diurnal variations were well reproduced in the WRF control simulation. For example, the daily highest temperature occurs at around 14:00 local time for both summer (~305 K) and winter (~292 K). The water vapor mixing ratio does not exhibit distinct

diurnal variation as does the temperature, but it does show a slight dryness in the early afternoon such as between 13:00 – 15:00 local time during summer.

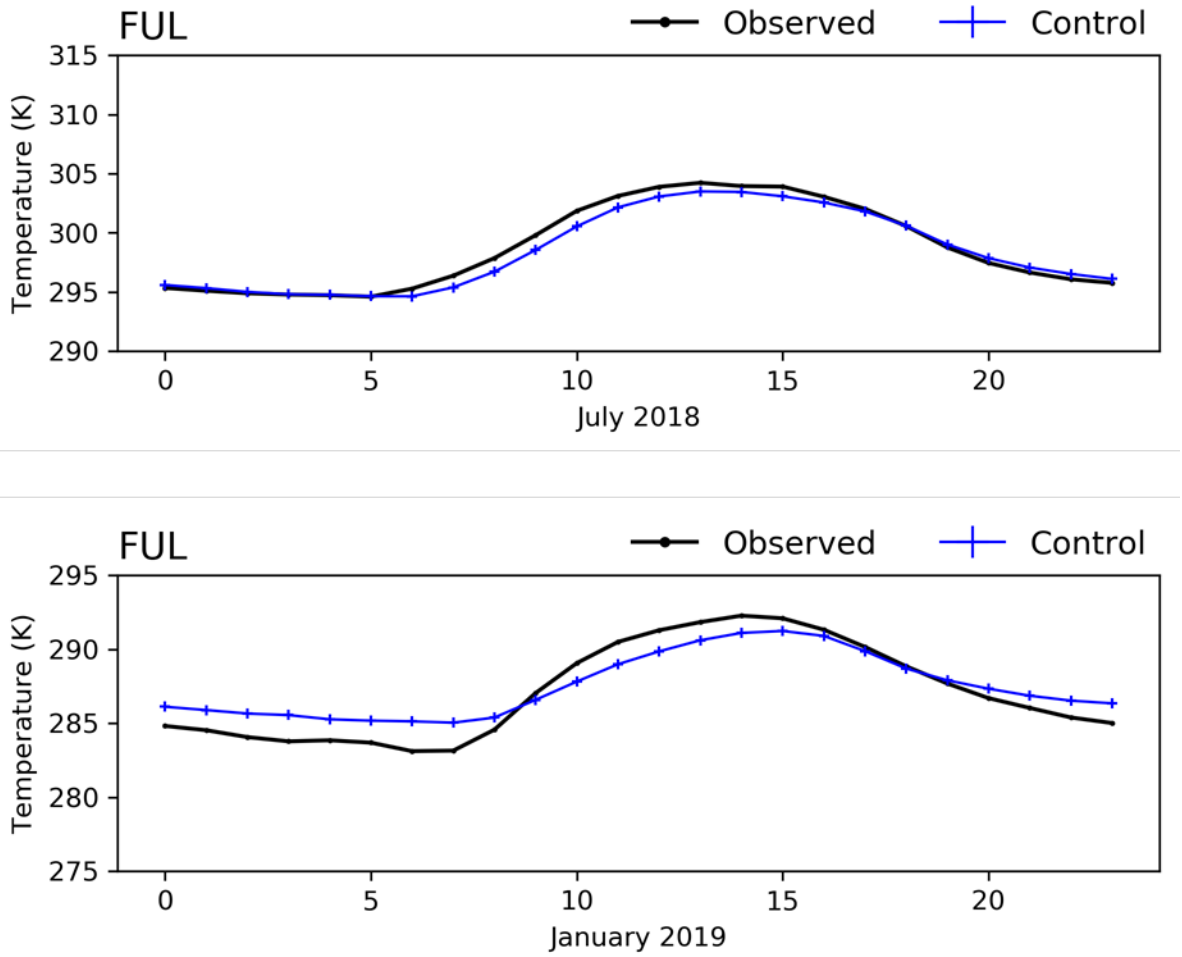

Figure IX-3-21

Measured vs simulated composite diurnal temperature variation at Fullerton (FUL) station for July 2018 and January 2019

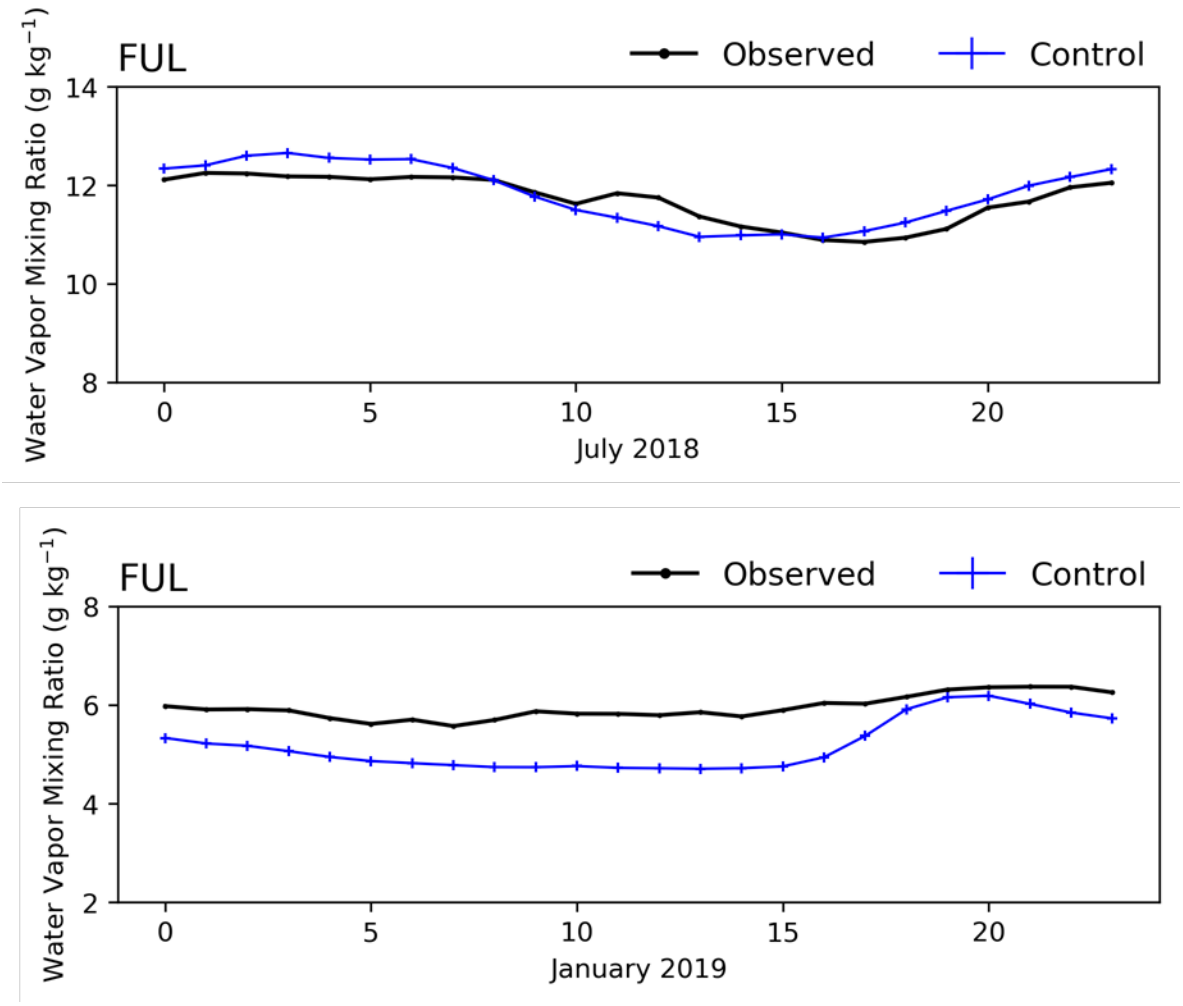

Figure IX-3-22

Water vapor mixing ratio at Fullerton (FUL) station from measurement and WRF control simulation for July 2018 and January 2019

IX.3.6 Meteorological Model Performance – Wind Rose

The measured and WRF control simulated wind rose at each station for 1-year period of May 2018– April 2019 are shown in Figure IX-3-23 – Figure IX-3-27. The wind rose plots for 5 stations are presented. In general, the control simulations reproduce the dominant wind direction as the measurement at each station. For example, the station of CNO, FUL, HHR and ONT all have southwest wind as prevailing wind direction showed from both observations and simulations. The wind direction is mostly from the southeast at the BUR station, as presented in both observations and simulations. For the wind speed, among the five stations, the FUL and BUR stations have calm winds, mostly under 6 m/s, while other stations showed stronger wind between 6 - 8 m/s. In general, the WRF control simulation underestimates the observed wind speed at HHR and ONT stations.

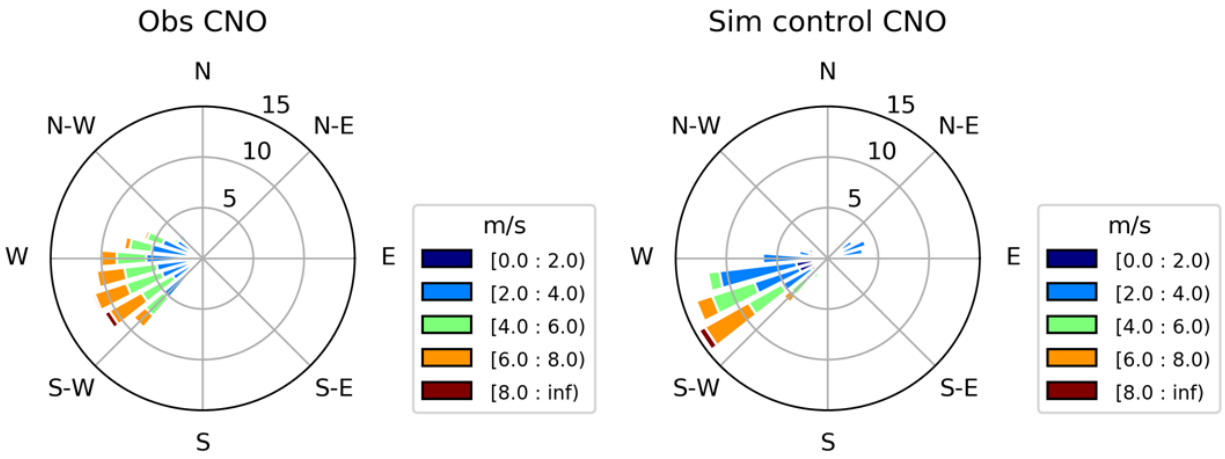

Figure IX-3-23

Wind rose from measurement and WRF control simulation at Chino (CNO) station during MATES V

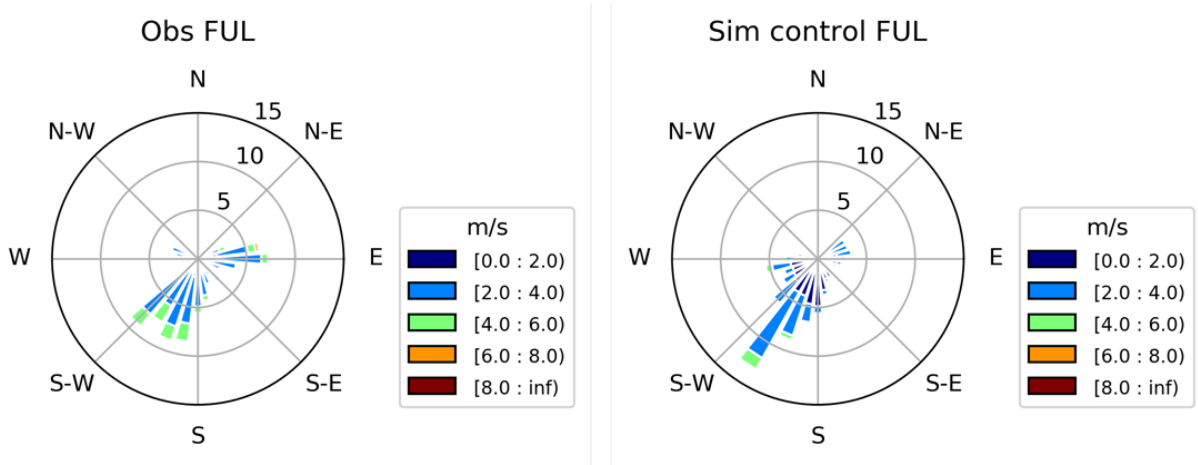

Figure IX-3-24

Wind rose from measurement and WRF control simulation at Fullerton (FUL) station during MATES V

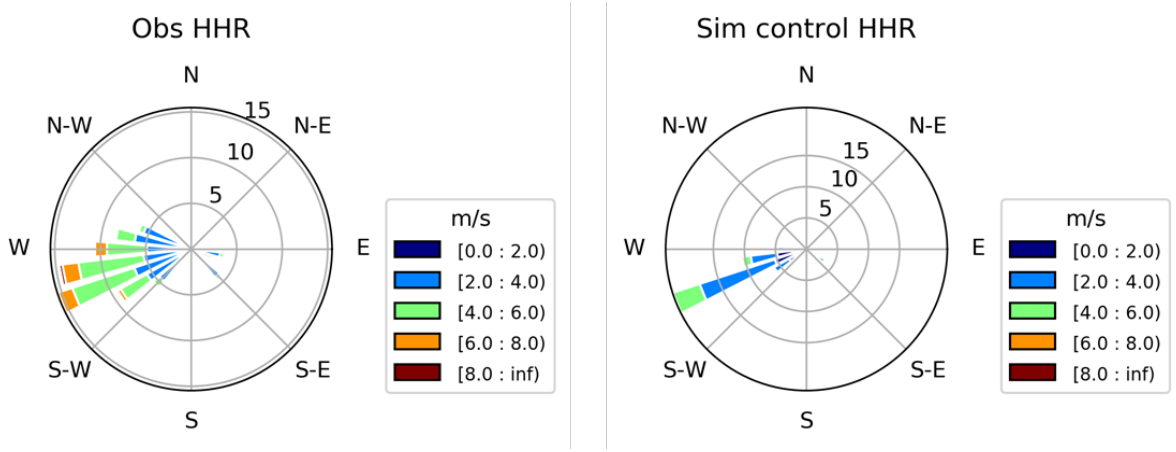

Figure IX-3-25

Wind rose from measurement and WRF control simulation at Hawthorne (HHR) station during MATES V

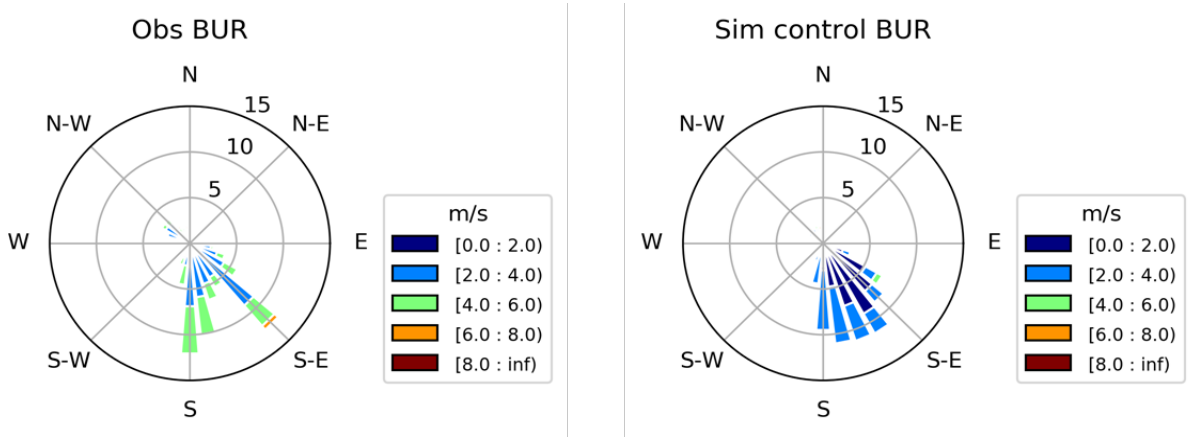

Figure IX-3-26

Wind rose from measurement and WRF control simulation at Burbank (BUR) station during MATES V

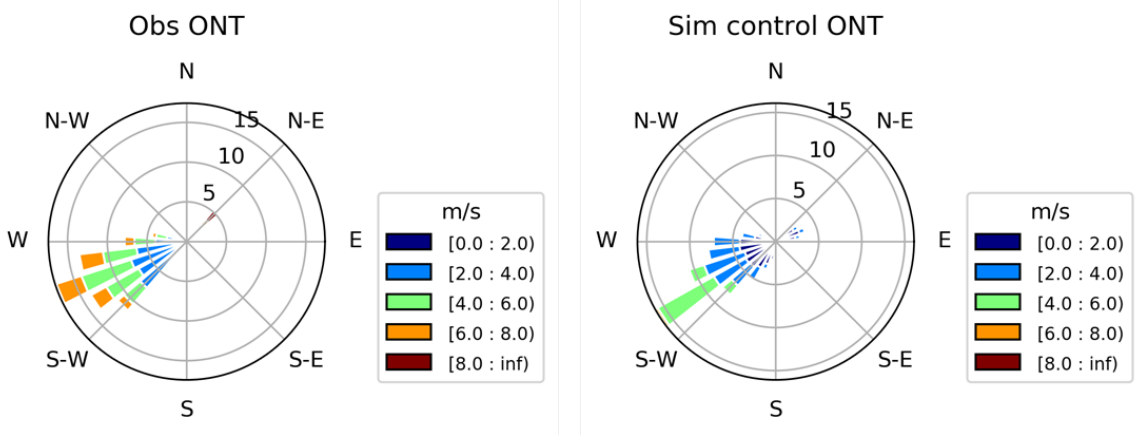

Figure IX-3-27

Wind rose from measurement and WRF control simulation at Ontario (ONT) station during MATES V

IX.3.7 Meteorological Model Performance – Planetary Boundary Layer Height (PBLH)

Time series of hourly PBLH from Ceilometer measurements and WRF control simulations for July 2018 at ONT and IRV are shown in Figure IX-3-28. The simulations match very well with the Ceilometer PBL height in general except the Ceilometer reported several very high values such as values higher than 2 km. The very high PBL values from the Ceilometer might be caused by some contamination from clouds. Time series of seasonal composed PBLH diurnal variation from measurement and the WRF control simulations for summer season (June, July and August of 2018) at ONT and IRV shown in Figure IX-3-29. The PBL height development processes from midnight through daytime toward late night are well captured by the simulations. For example, at ONT, the PBL height is lowest (~200 m) during early morning and develops to

higher values of ~800 m around noon time because convection and vertical mixing are stronger, then slowly decays to the lower heights during the late afternoon and early night.

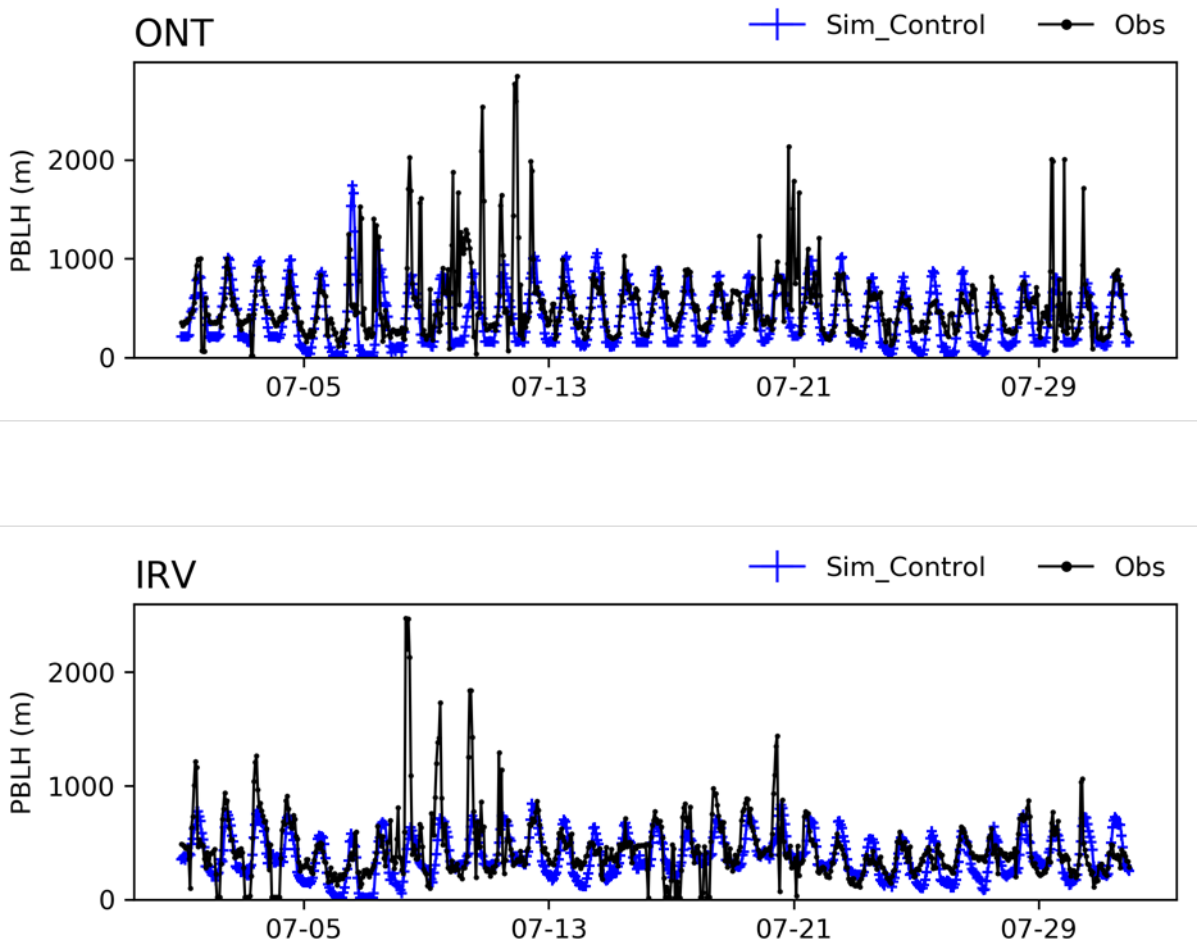

Figure IX-3-28

Time series of hourly PBLH from ceilometer measurement and WRF control simulations for July of 2018 at Ontario (ONT) station and at Irvine (IRV) station

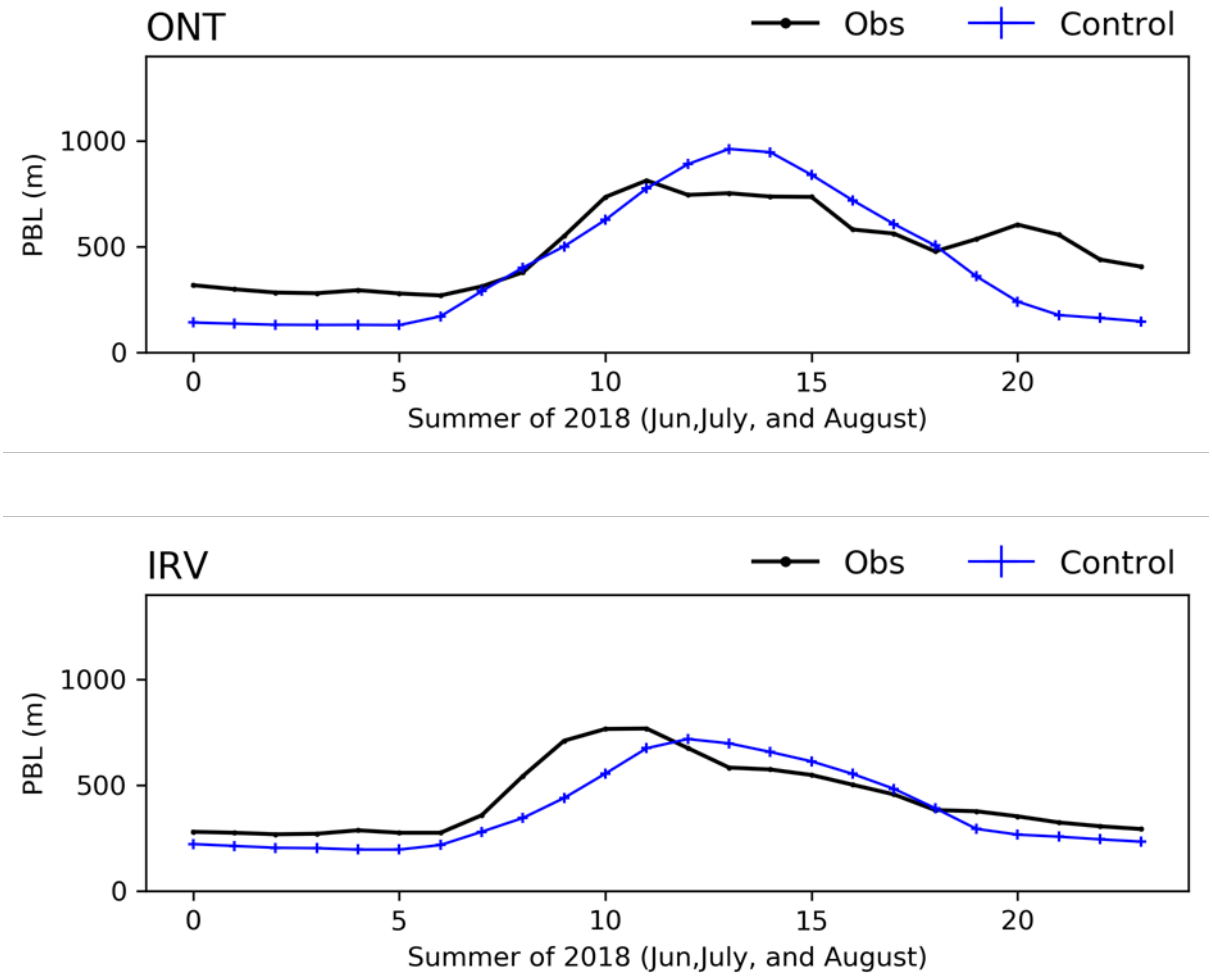

Figure IX-3-29

Time series of seasonal composed PBLH diurnal variation from ceilometer measurement and WRF control simulations for summer season (Jun, July and August of 2018) at Ontario (ONT) station and Irvine (IRV) station

IX.3.8 Vertical Dispersion

The WRF output was converted to the CAMx reactive tracer (RTRAC) format using 'wrfcamx_v.7' software. Vertical diffusivity (*Kv*), which is critical in vertical dispersion, was computed using CMAQ vertical diffusivity scheme with a minimum value of 1.0 m^2/sec. The number of vertical layers was reduced to 18 layers from the 30-layer configuration used in the WRF. The layers whose height was below 2 km from the ground level were remained unchanged. The layers above 2 km were collapsed to four layers in order to reduce computation cost. The vertical structure was chosen carefully to optimize computational efficiency and numerical accuracy based on an extensive sensitivity study evaluating the impact of vertical layer structure using various numbers of computational layers.

There are three *Kv*-patch options: 1) Land use-based patch to enhance mixing over urban areas; 2) the OB70 patch applies the O'Brien 70 [OB70] (O'Brien, 1970) profile through a user specified surface layer depth. Its purpose is to maintain higher vertical diffusivity during nighttime hours to help reduce over predictions in the buildup of NOx; 3) the cloud patch extends the daytime PBL vertical diffusivity profile through capping cloud tops as a means to prohibit artificial collapse of the boundary layer when convection develops and to include convective venting to the free troposphere. Since the SoCAB is mostly under stable atmosphere especially during pollution episodes, it is recommended to avoid using the cloud patch. In all, after careful evaluation of various sensitivity analyses, the vertical dispersion profile used in the final MATES V CAMx RTRAC simulations relied on a 16-layer structure using the CMAQ diffusivity scheme overlaid with the *Kv*-patch option. The land use-based patch and OB79 patch are applied with the minimum vertical diffusivity of 1.0 m^2/sec. In the current study, the first and second computational layers, which are centered approximately 20 m and 40 m above ground level, respectively, were subject to the direct modification of the *Kv* through the *Kv* patch.

IX.4 MATES V CAMx Modeling Emissions

An updated version of the 2016 AQMP emissions inventory for the year 2018 provided mobile and stationary source input for the MATES V CAMx RTRAC simulations. On-Road mobile source emissions were updated based the most recent CARB model, EMFAC2017 (CARB, 2017) and adjusted for time-of-day and day-of-week travel patterns based on CalTrans Performance Monitoring System (PeMS) and weigh-in-motion data profiles. The updated inventory also included 2018 reported point source emissions and updated OGV emissions. Table IX-4-1 lists the annual average day emissions for 2018. (A comprehensive breakdown of the planning VOC, NOx, CO, SO2 and particulate emissions for 2018 used in the MATES V simulation is provided in Chapter 3 and Appendix VIII). Table IX-4-1 also includes the MATES IV total suspended particulate matter (TSP) and $PM_{2.5}$ diesel emissions for 2012 for comparison.

Table IX-4-1
Annual Average Diesel/EC Emissions in the SCAB (TPD)

Compound	MATES IV 2012		MATES V 2018	
	$PM_{2.5}$	TSP	$PM_{2.5}$	TSP
EC	11.58	14.74	5.05	7.85
Total Diesel Particulate Matter (DPM)	9.43	10.24	4.53	4.85
DPM per Major Source Category				
On-road	4.97	5.40	2.00	2.11
Off-road	2.94	3.20	1.81	1.98
Ships	0.74	0.78	0.29	0.31
Trains	0.56	0.61	0.30	0.32
Stationary	0.22	0.25	0.14	0.14
Total DPM	9.43	10.24	4.53	4.85

A comparison of the MATES V 2018 $PM_{2.5}$ diesel emissions shows a 52% reduction in emissions from the 2012 emissions used in MATES IV. The most significant area of diesel particulate matter emissions reduction occurs in the on-road categories due to significant DPM reductions from CARB's Truck and Bus Regulation.

Figures IX-4-1a through IX-4-1x provide the grid-based average modeling emissions for selected toxic pollutant and precursor emissions categories.

The MATES V modeling used the latest available emissions data. For major point sources, reported annual emissions were used. For area and off-road mobile sources, although annual emissions were based on projection in 2016 AQMP, the latest updated spatial surrogates were used to allocate county total emissions to a specific grid in the modeling domain. The EMFAC2017 emission factors along with SCAG's transportation modeling for 2018 developed for the 2016 RTP/SCS, CalTrans Performance Measurement System (PeMS) and Weigh-in-Motion (WIM) data, and ambient conditions from WRF modeling were used to generate spatially and temporally resolved on-road modeling emissions. The projected annual emissions from ocean-going vessels (OGV) for 2018 from the CARB 2018 SIP update (CARB, 2018) were also used. Emissions from OGV and commercial harbor craft (CHC) were spatially and temporally resolved using Automatic Identification System (AIS) data. OGV emissions are released through stacks, which result in the emissions penetrated to the computational layer 2 and higher, while CHC emissions were assumed to be released at the sea level due to the lower profile of a typical harbor craft. The latest biogenic emission model, Model of Emissions of Gases and Aerosols from Nature 3 (MEGAN3), together with WRF outputs were used to generate day-specific biogenic emissions.

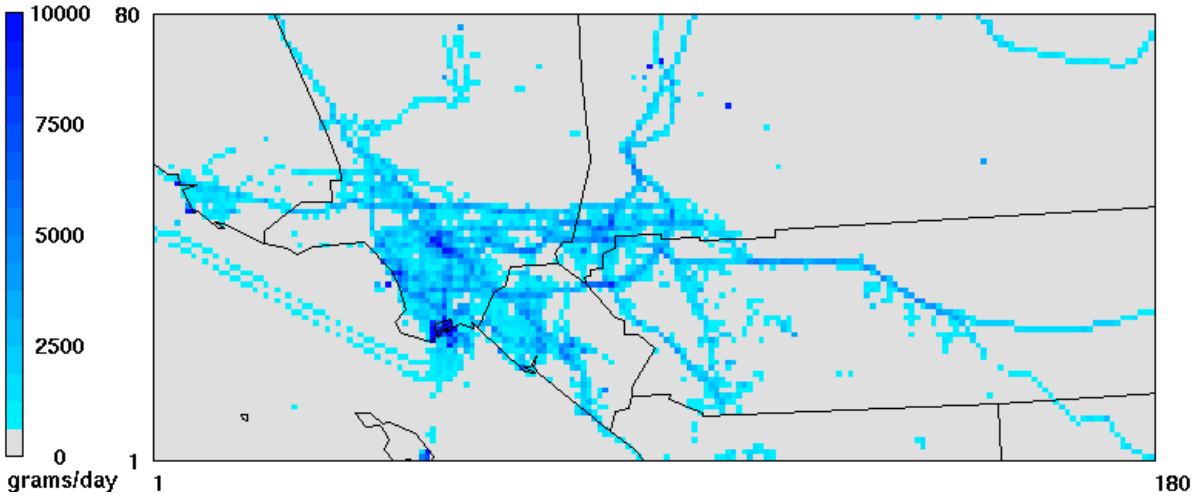

Figure IX-4-1a
Average emissions pattern for diesel PM from all source categories

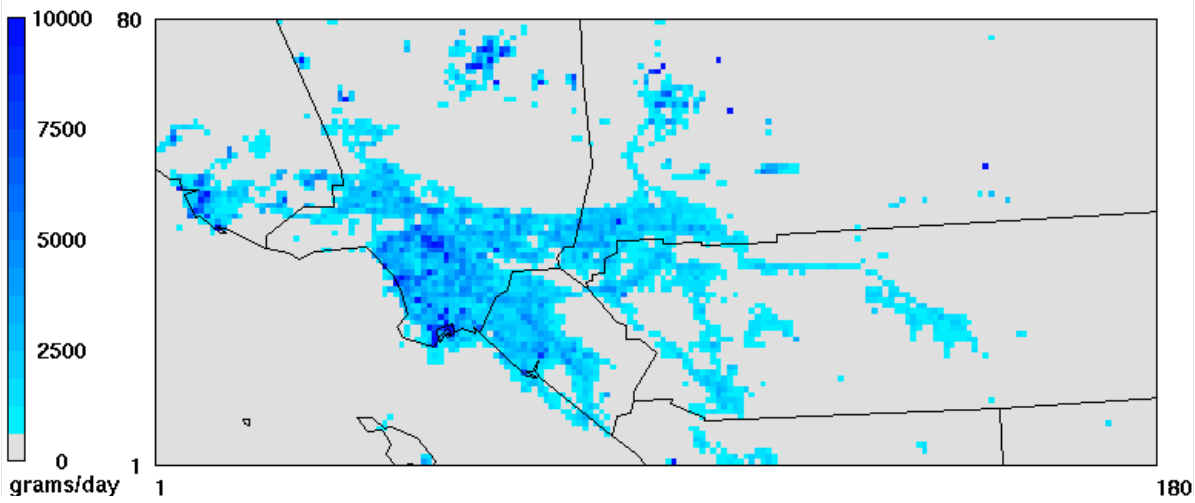

Figure IX-4-1b
Average emissions pattern for elemental carbon

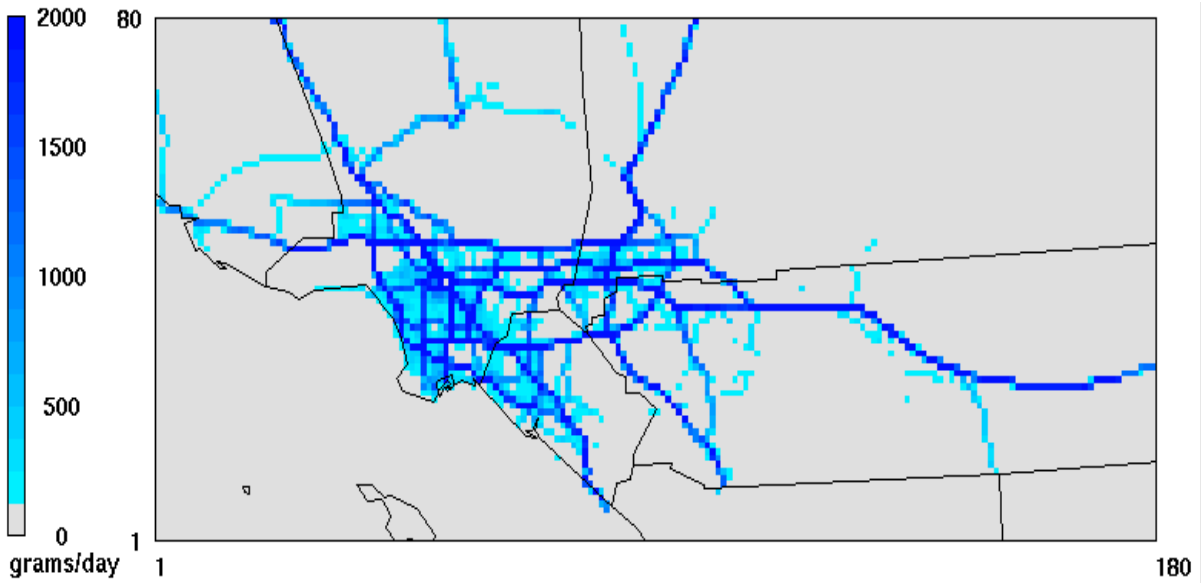

Figure IX-4-1c
Average emissions pattern of on-road diesel PM

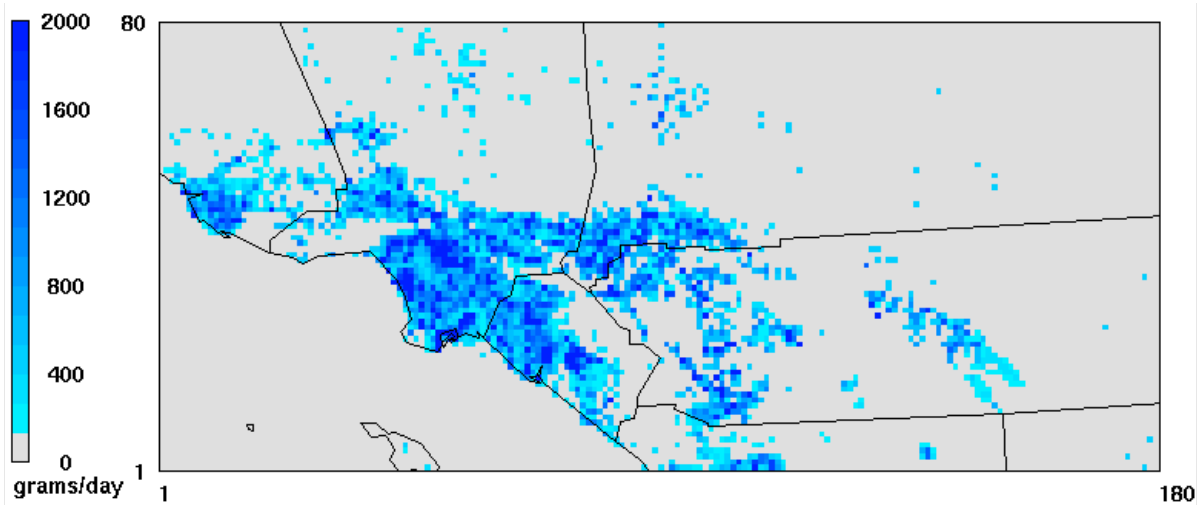

Figure IX-4-1d
Average emissions pattern of off-road diesel PM

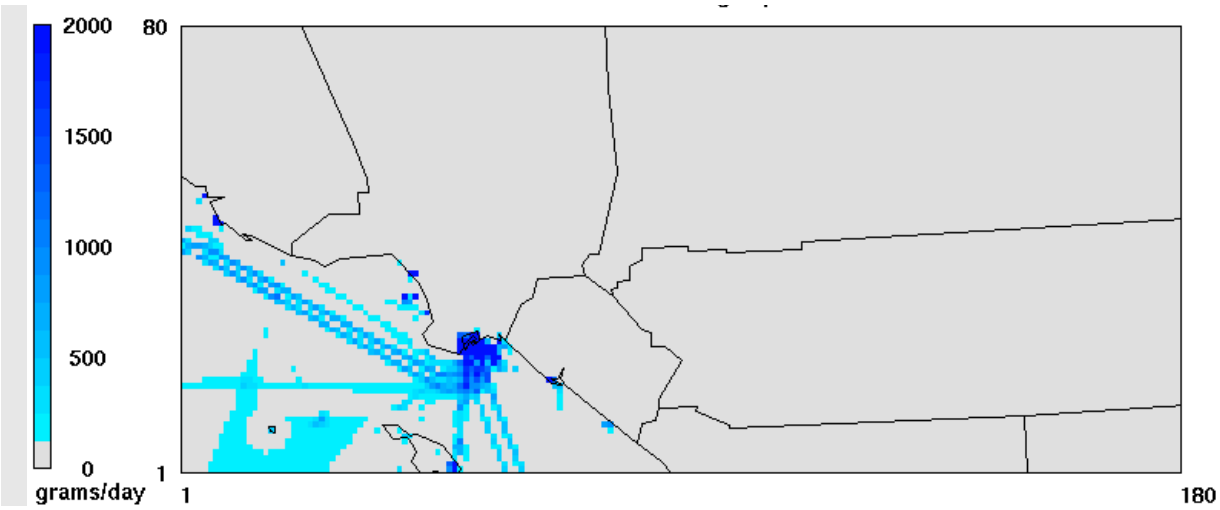

Figure IX-4-1e
Average emissions pattern of diesel PM from OGV and CHC.

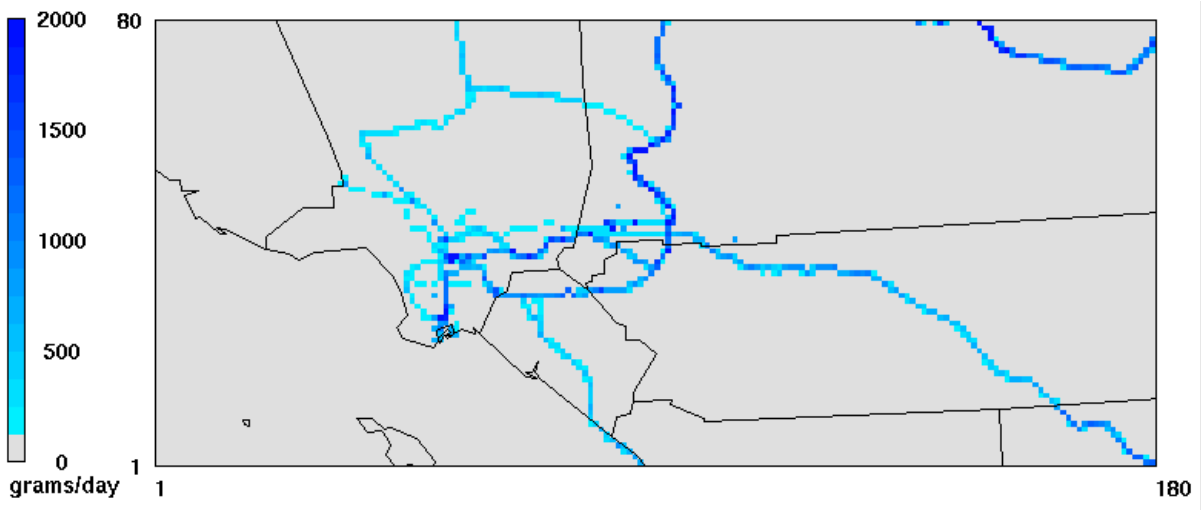

Figure IX-4-1f
Average emissions pattern of diesel PM from trains

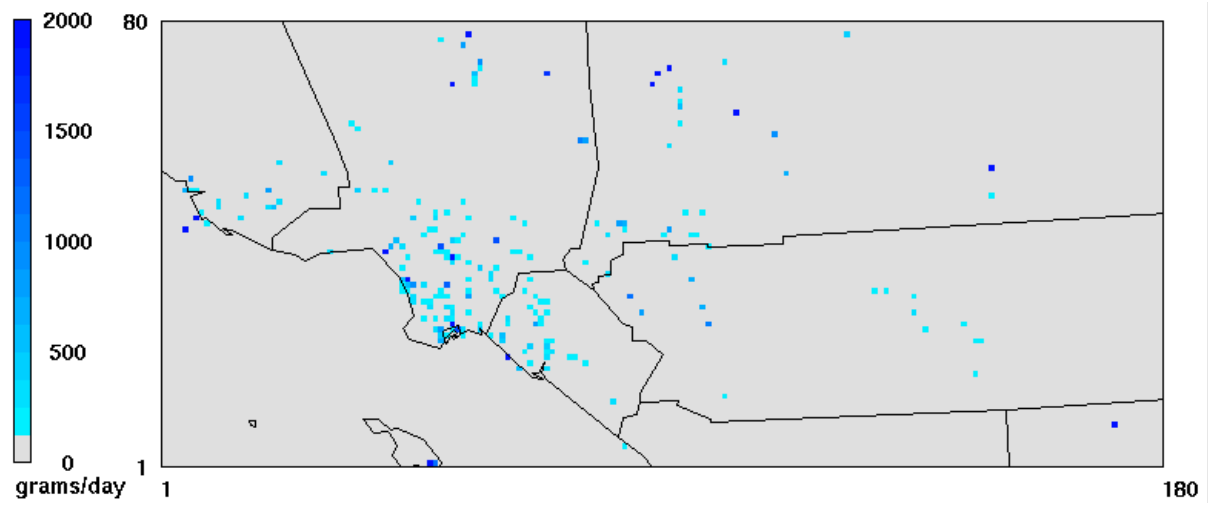

Figure IX-4-1g
Average emissions pattern Diesel PM from stationary sources

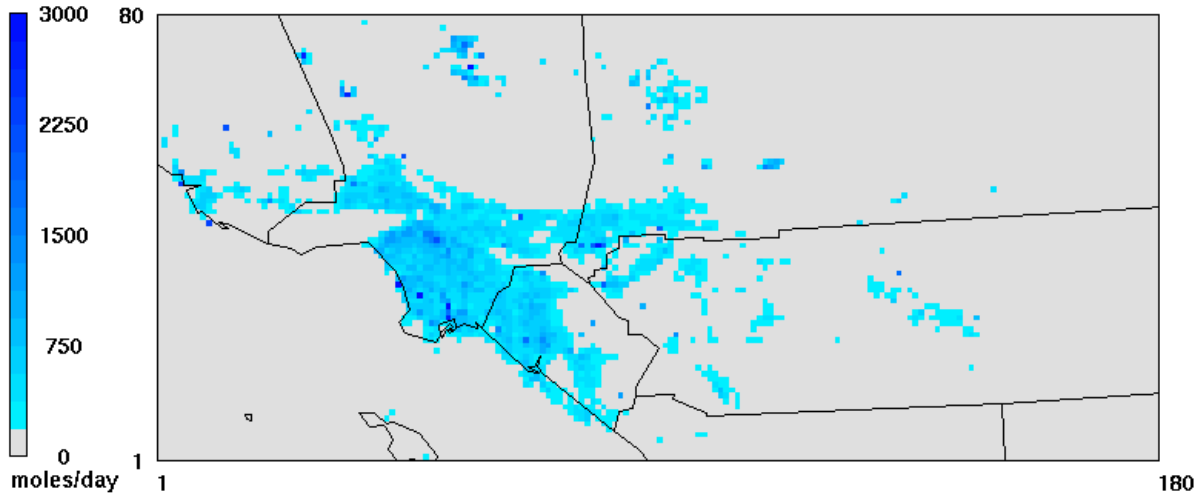

Figure IX-4-1h
Average VOC emissions pattern from all source categories

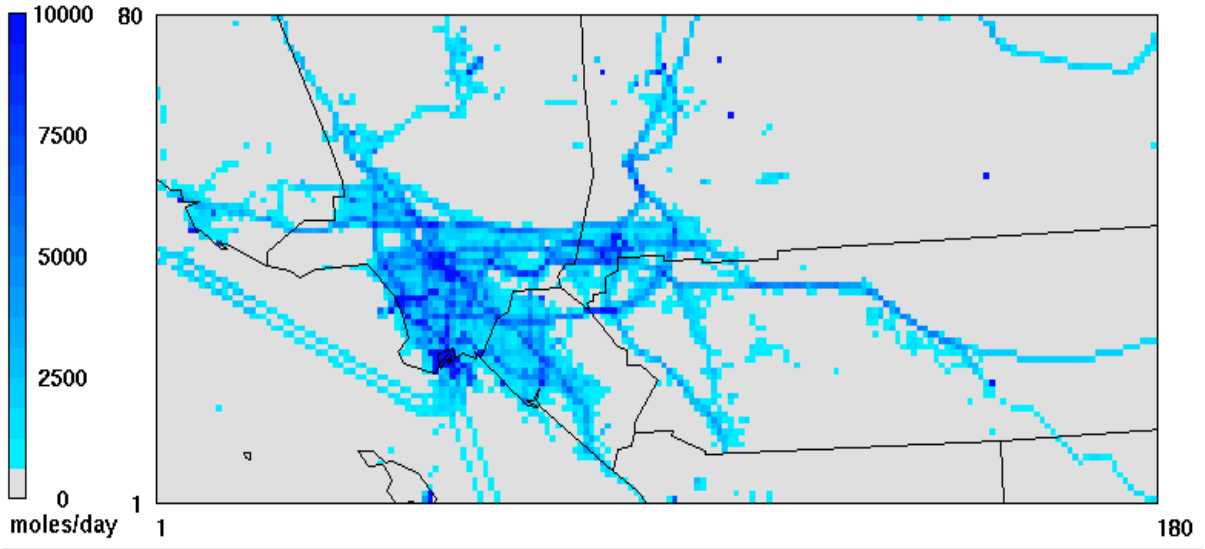

Figure IX-4-1i
Average NOx emissions pattern from all source categories

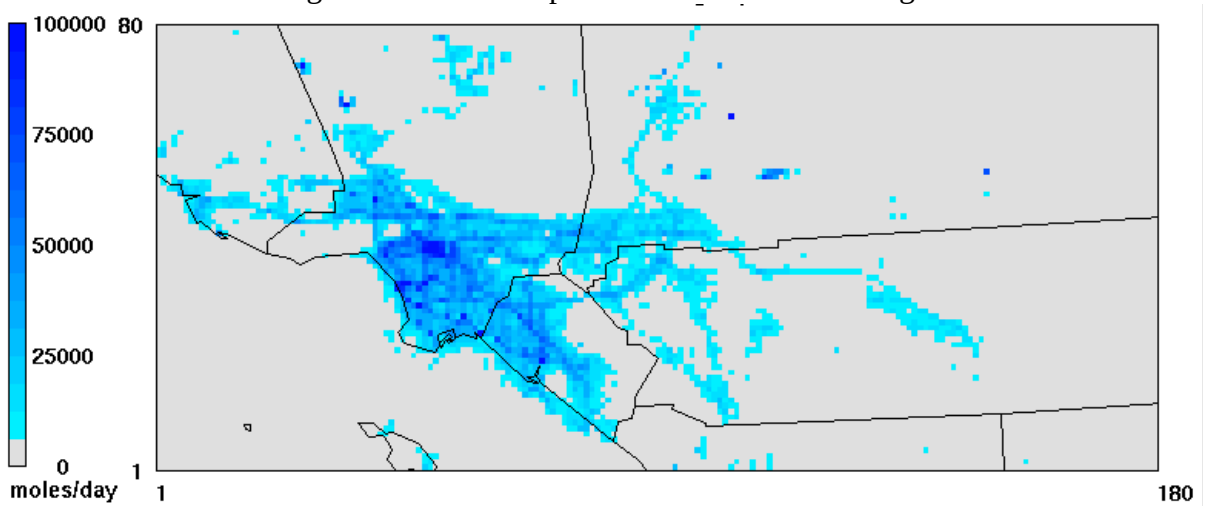

Figure IX-4-1j
Average CO emissions pattern from all source categories

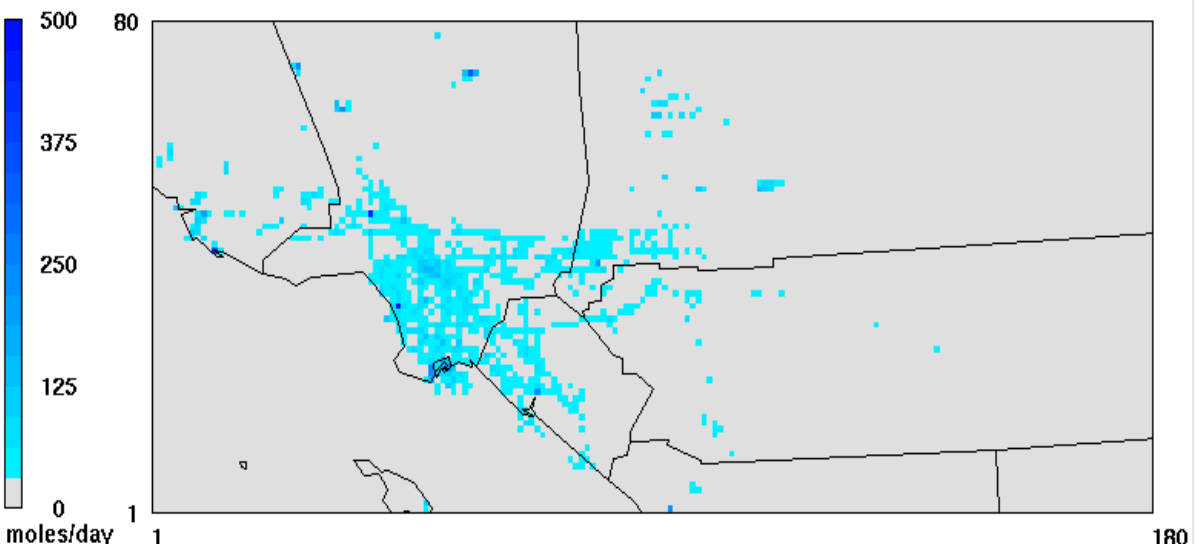

Figure IX-4-1k
Average emissions pattern for Acetaldehyde from all source categories

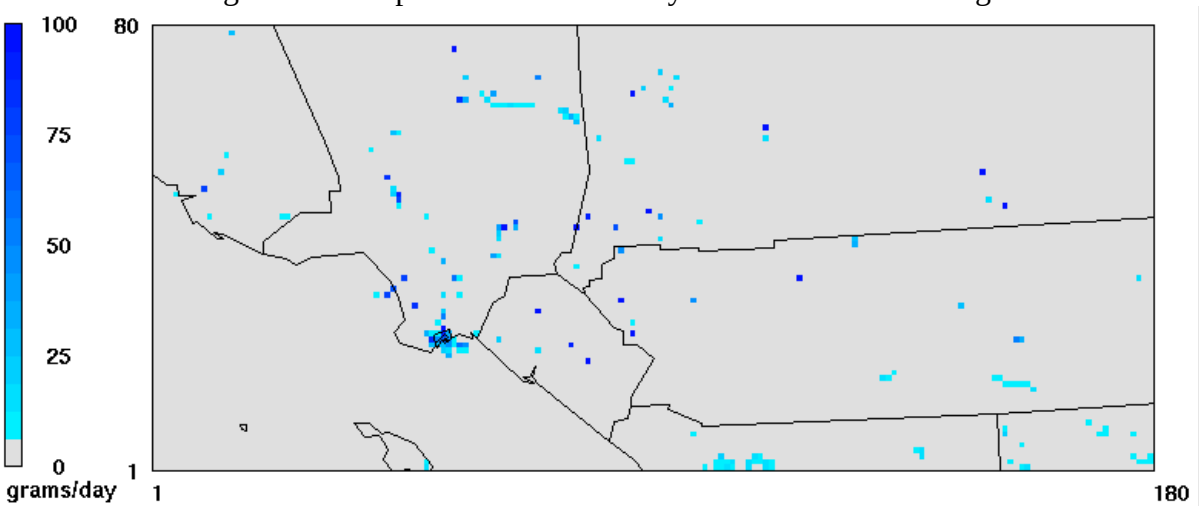

Figure IX-4-1l
Average Arsenic emissions pattern from all source categories

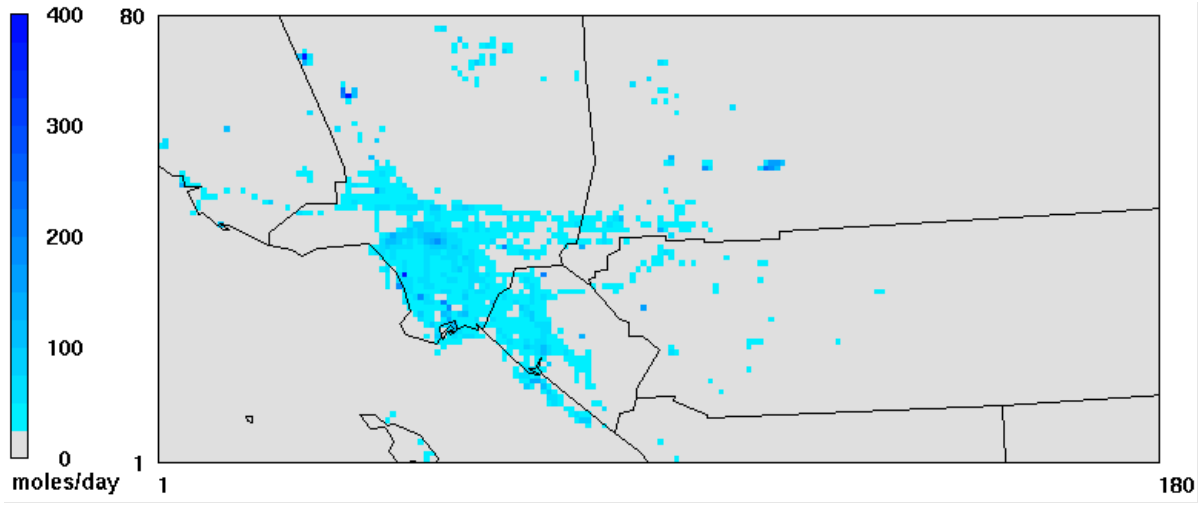

Figure IX-4-1m
Average Benzene emissions pattern from all source categories

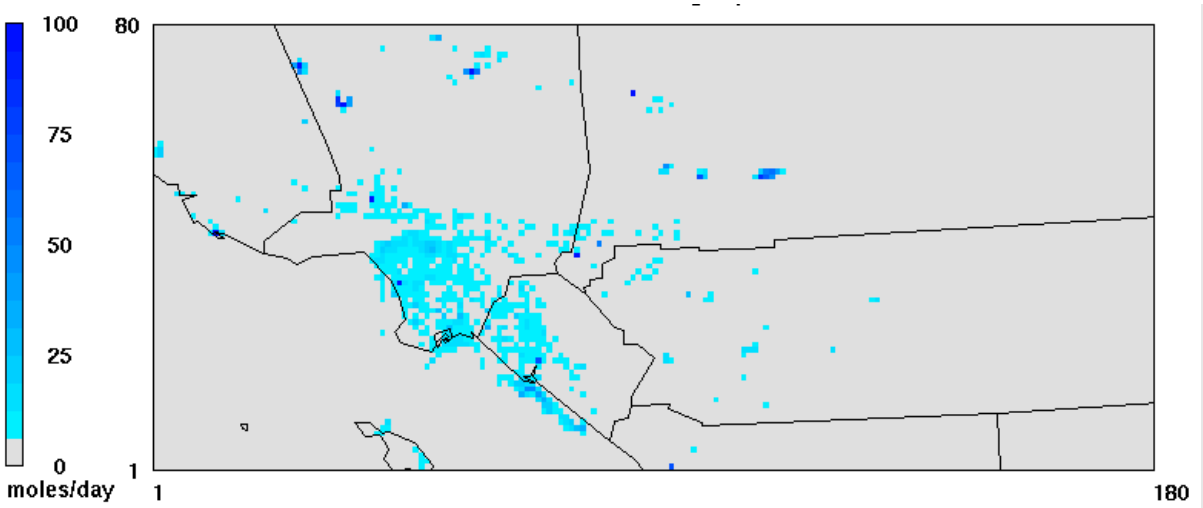

Figure IX-4-1n
Average 1,3-Butadiene emissions pattern from all source categories

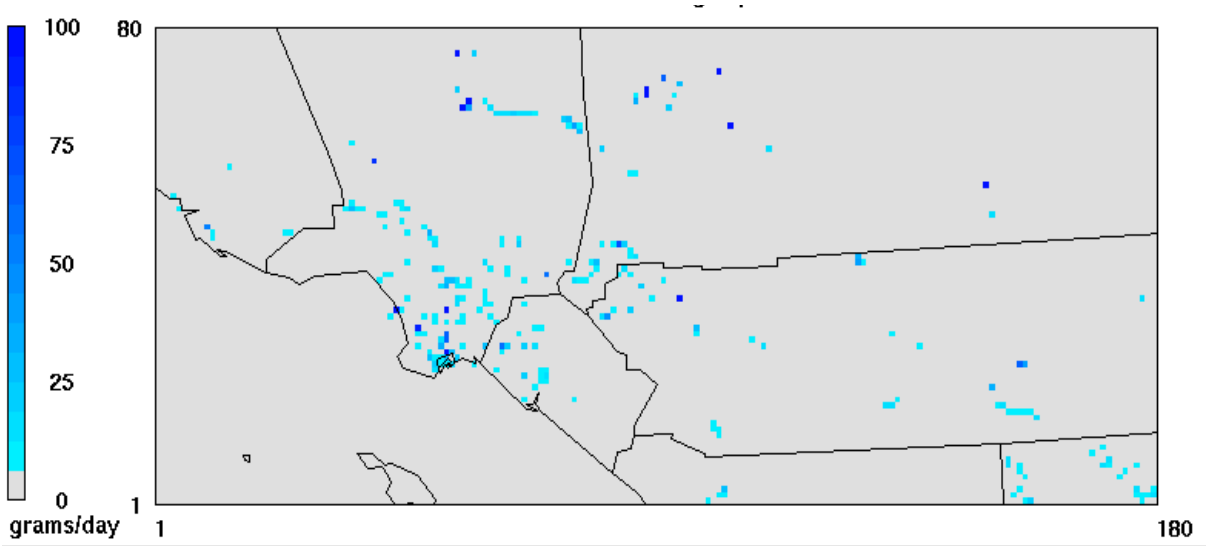

Figure IX-4-1o
Average Cadmium emissions pattern from all source categories

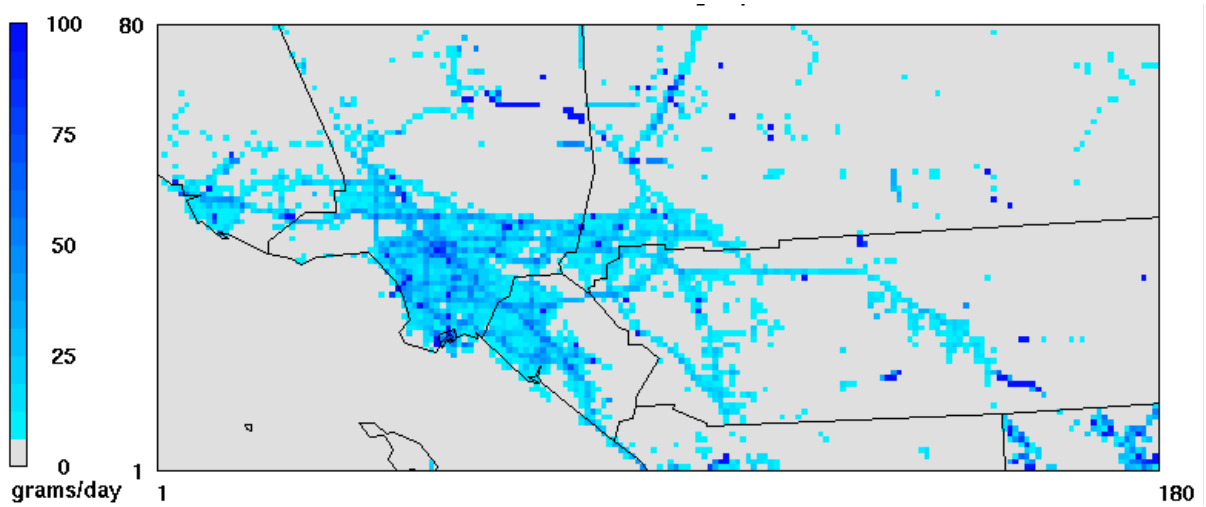

Figure IX-4-1p
Average Total Chromium emissions pattern from all source categories

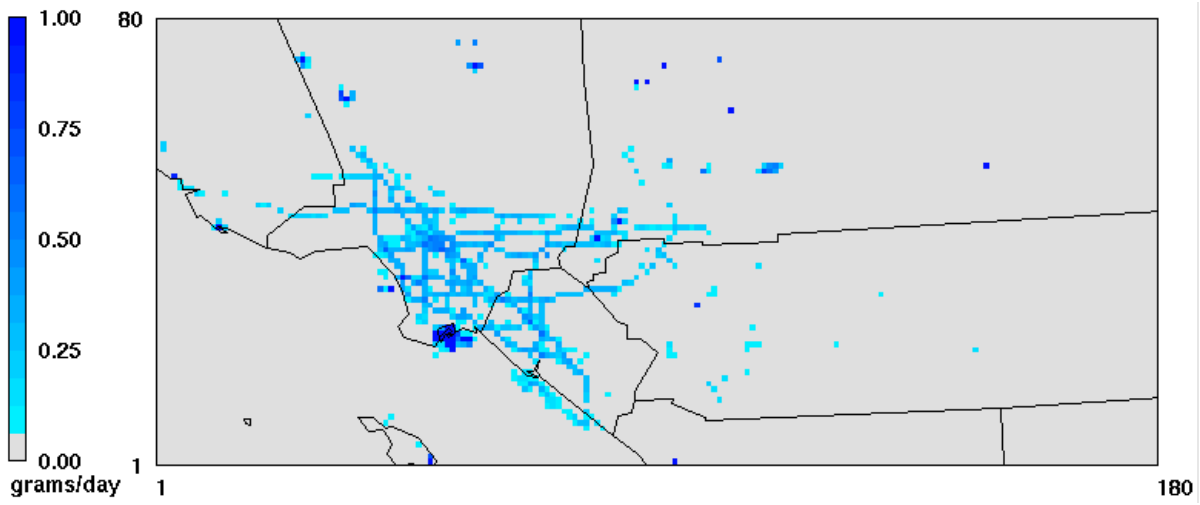

Figure IX-4-1q
Average Hexavalent Chromium emissions pattern from all source categories

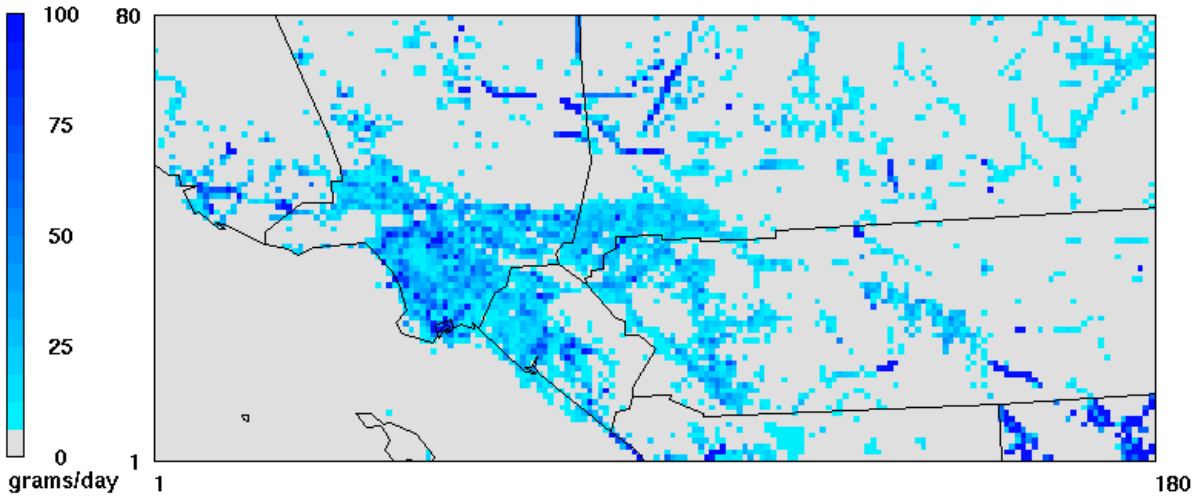

Figure IX-4-1r
Average Lead emissions pattern from all source categories

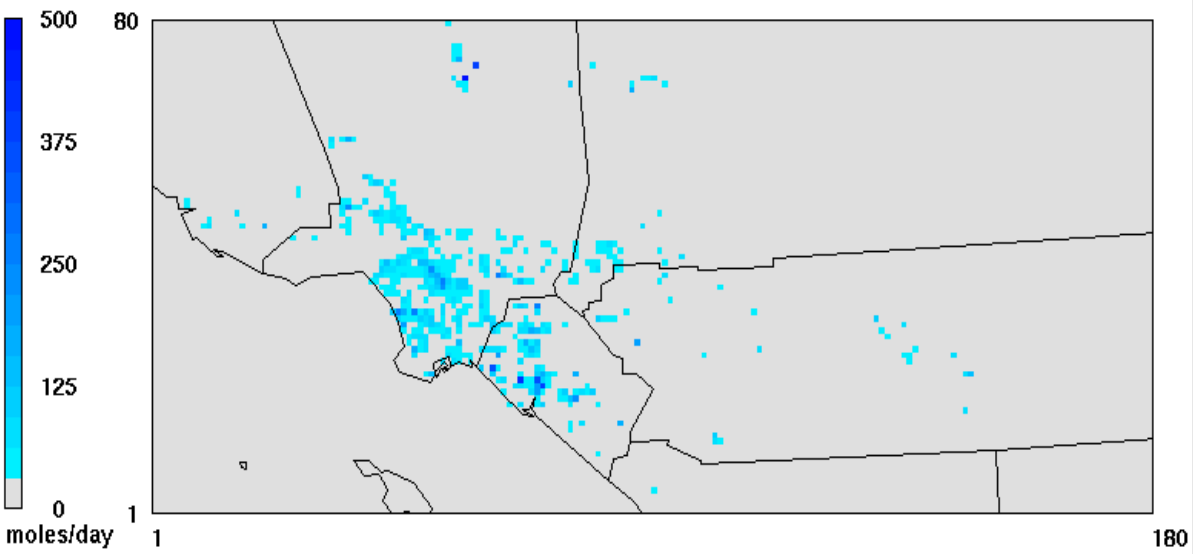

Figure IX-4-1s
Average Methylene Chloride emissions pattern from all source categories

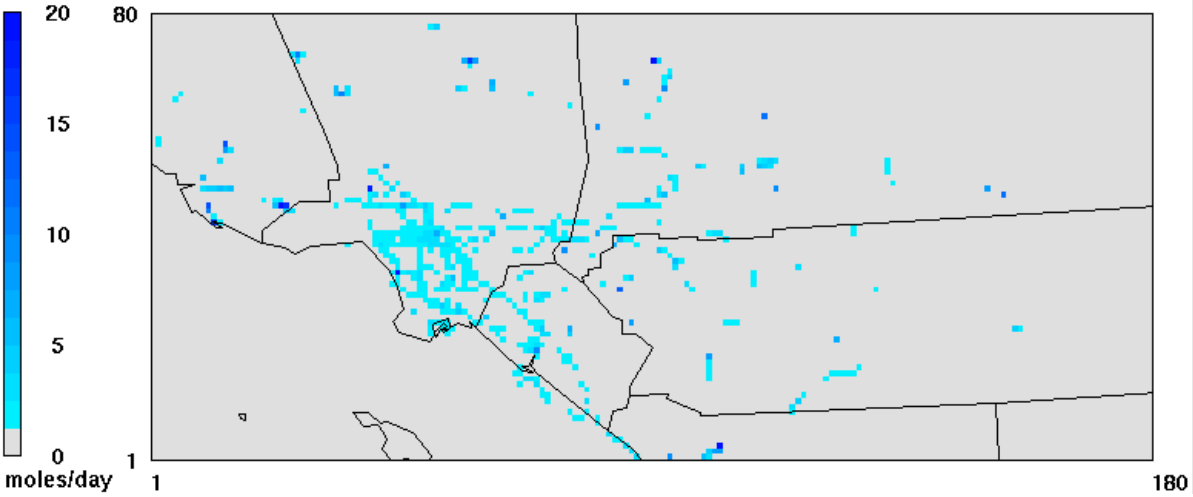

Figure IX-4-1t
Average Naphthalene emissions pattern from all source categories

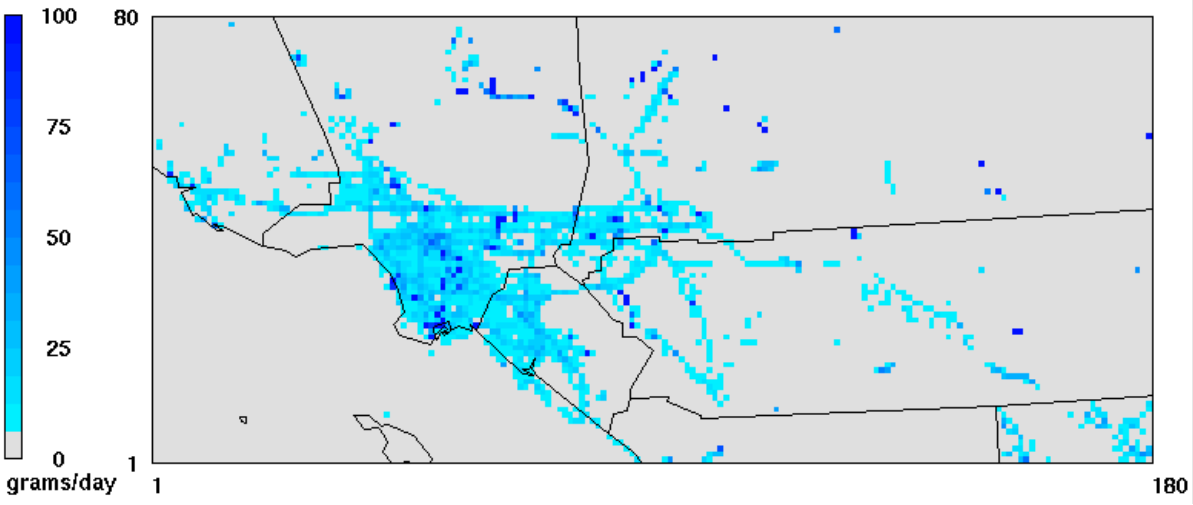

Figure IX-4-1u
Average Nickel emissions pattern from all source categories

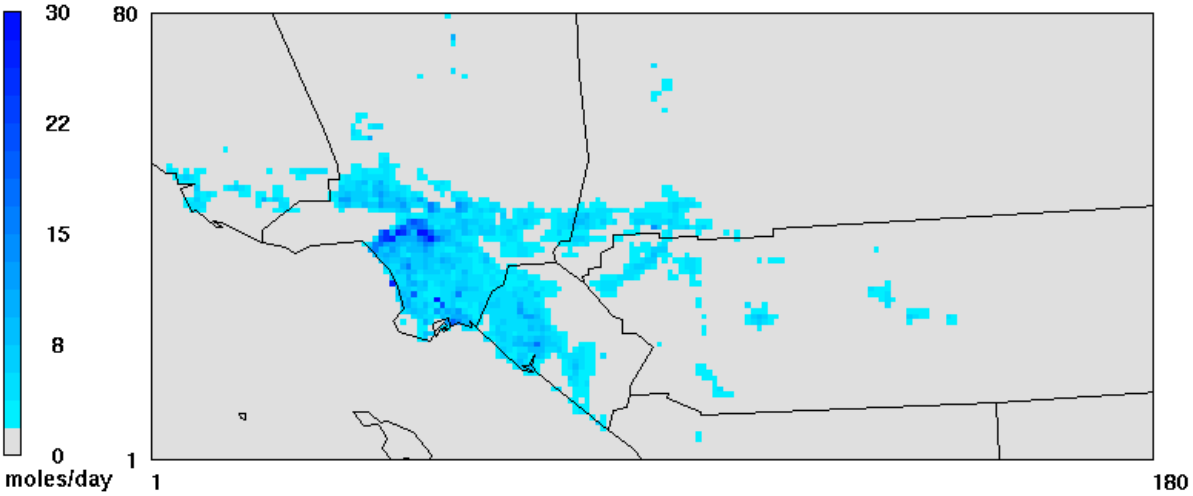

Figure IX-4-1v
Average p-Dichlorobenzene emissions pattern from all source categories

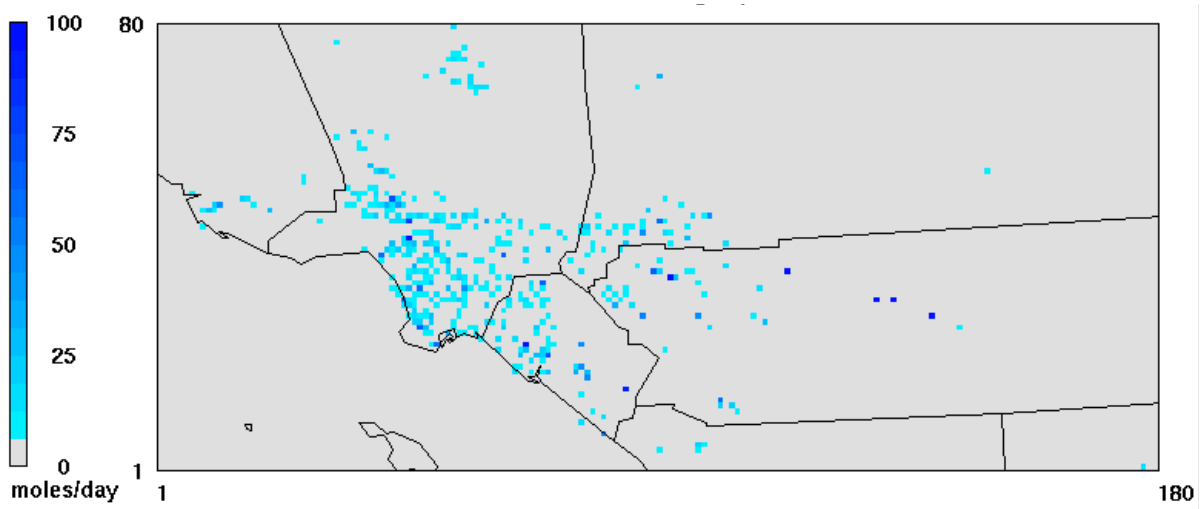

Figure IX-4-1w
Average Perchloroethylene emissions pattern from all source categories

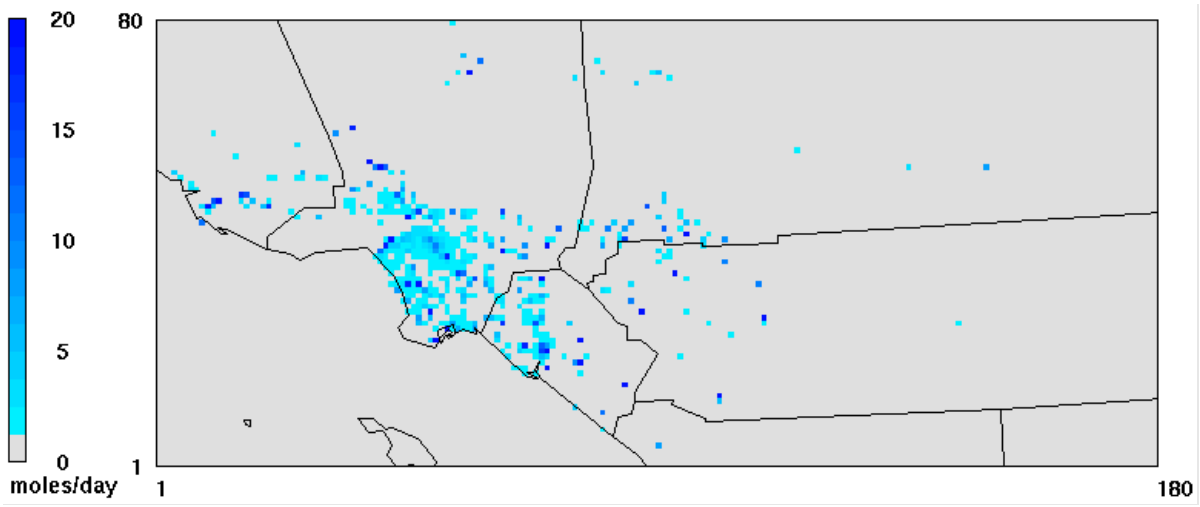

Figure IX-4-1x
Average Trichloroethylene emissions pattern from all source categories

IX.5 Modeling Setup

The MATES V regional modeling analyses relies on the CAMx RTRAC model to simulate annual impacts of both gaseous and aerosol toxic compounds. The accuracy of the modeling analyses depends on the accuracy of region-wide emissions of air toxic compounds, temporal and spatial resolutions of these emissions, accurate representation of meteorological conditions and quality of modeling tools used. The South Coast AQMD staff strives to use the best information and modeling tools available at the time for its MATES modeling analyses. Table IX-5-1 summarizes the major components in the air toxics modeling and provides a comparison between the MATES V and MATES IV analyses.

Table IX-5-1
Summary and Comparison of Key Modeling Considerations Between
MATES IV and MATES V

Parameter	MATES IV	MATES V
Meteorological Modeling Year	July 2012 - June 2013	May 2018 - April 2019
Model Platform / Chemistry	CAMx RTRAC (5.30)	CAMx RTRAC (6.50)
Meteorology Model /Vertical Layers	WRF with 30 layers/ CAMx: 16 layers	WRF with 30 layers/ CAMx: 16 layers
On-Road mobile Emissions	EMFAC2011/2012 RTP Caltrans/SCAG Model Uniform day of week and hourly distributions by Caltrans District	EMFAC2017/2016 RTP Caltrans PeMS/WIM data and SCAG model Day-specific spatial and temporal distributions
OGV and CHC Emissions	2012 AQMP for 2012 OGV; Emissions spread through mostly layers 1 and 2; uniform spatial and temporal distributions	2018 SIP Update for OGV; Emissions spread through mostly layers 1 and 2; day-specific temporal and spatial distributions
Point Source Emissions	2012 Projection from 2008 (2012 AQMP)	2018 Annual Emissions Reports
Area Source Emissions	2012 Projection from 2008 (2012 AQMP)	2018 Projection from 2012 (2016 AQMP)
Off-Road Emissions except OGV	2012 Projection from 2008 (2012 AQMP)	2018 Projection from 2012 (2016 AQMP)

IX.6 Boundary and Initial Conditions

The day-specific boundary condition files were prepared by extracting values at boundary grids from the 2016 AQMP modeling domain, which spans 90 by 40 grids in the east-west and the north-south direction, respectively, with 4 km grid space (2016 AQMP, Appendix V, Figure V-2-2).The CMAQ modeling domain covers the South Coast Air Basin as well as adjacent counties in Southern California. SAPRC07 were chosen as the gaseous species mechanism and AERO6 were chosen as aerosol module in the CMAQ modeling (South Coast AQMD, 2020). In total, 171 modeled gaseous and aerosol species were extracted from the CMAQ hourly simulation outputs using the BCON m3conc utility. For the unmodeled toxic gaseous and metal components required in the MATES V modeling, the boundary values were scaled based on the resolved CMAQ surrogate concentrations. The corresponding days in the 2018 CMAQ modeling values were used for the boundary conditions extraction during the January to April 2019 MATES modeling period. In order to minimize the impact of the unrealistic low CMAQ simulated

benzene concentrations to MATES V domain, a fixed value as 0.1 ppbV were replaced for the lateral boundary condition.

The initial condition files were prepared using the *icbcprep* utility included in the CAMx standard package. The utility prepares uniform boundary and initial conditions with prescribed values. The initial values turn out to be not significant in the annual modeling, since the footprint of the initial values typically disappear in approximately 7 to 10 days of time integration, depending on grid size and chemical mechanism. In the MATES V simulations, 7 days were used as initial spin-up.

IX.7 CAMx Modeling Results

CAMx modeling results, CAMx modeling performance evaluation, and cancer risk estimation based on model predicted air toxics concentrations, OEHHA's cancer potency factor and population were presented in this section. The estimated cancer risk based on CAMx modeling results were compared with measurement-based cancer risk and those from MATES IV to evaluate the progress in improving air quality for the South Coast Air Basin and Coachella Valley.

IX.7.1 Overall Model Performances

The performance of the CAMx regional modeling simulation is summarized through statistical and graphical analysis, including time series of key pollutant concentrations. Summarized in Table IX-7-1 are the measurements and model predictions of toxic components during the sampling period. Prediction Accuracy (PA), defined as the percentage difference between the mean observed and simulated concentrations, is given as an indicator for the model performance.

For the MATES V period, the model simulated concentrations of particulate matter species, such as $EC_{2.5,}$ and TSP metals, compared favorably with measurement results. Concentrations of some air toxic species, such as perchloroethylene, p-dichlorobenzene, trichloroethylene, and naphthalene have become low enough that model performances for those pollutants are immaterial. Concentrations of 1,3-butadiene was underpredicted by the modeling. Emissions of 1,3-butadiene are primarily from gasoline combustion. Recently, CARB updated emissions from small off-road engines (CARB, 2020). This update is expected to increase 1,3-butadiene emissions marginally and to help reduce some of the underprediction, and is not incorporated in this modeling. Benzene and methylene were relatively well-simulated. Compared to MATES IV, ambient concentrations of formaldehyde and acetaldehyde increased in MATES V. These increases were incongruent with the expected emission decreases between the two MATES periods. Consequently, the model underpredicted the formaldehyde and acetaldehyde concentrations.

Simulated annual average $EC_{2.5}$ was used to assess overall model performance for the MATES V period. Tables IX-7-2 summarizes the MATESV $EC_{2.5}$ performance.

EPA guidance (U.S. EPA, 2006) recommends evaluating gaseous and particulate modeling performance using measures of prediction bias and error. PA goals of ±20% for ozone and ±30%

for individual components of $PM_{2.5}$ or PM_{10} have been used to assess simulation performance in previous modeling attainment demonstrations.

As shown in the Tables IX-7-2, eight of the 10 MATES V sites meet the $PM_{2.5}$ PA goal. In general, the model underpredicts annual average concentrations at the Rubidoux, Inland Valley San Bernardino, Compton and Pico Rivera stations, consistent with what was observed in our past modeling effort. Concentrations in locations such as Burbank Area, Long Beach and Anaheim are overpredicted. Overall, modeled $EC_{2.5}$ concentrations were 5% lower than the measurements, which were likely driven by the CAMx not being able to predict extreme high events (See Figures IX-7-1).

Table IX-7-3 provides the CAMx RTRAC performance for benzene at the 7 MATES V monitoring sites. Benzene model performance is included in the evaluation because of the confidence in the benzene measurement data based on the long-term monitoring conducted in the Basin and throughout California. With the exception of the Burbank Area site (25% over), the annual average benzene concentrations are underpredicted with Compton showing the largest low bias (36%). Overall, the model underpredicted benzene concentrations by 13%. Therefore, the overall model performance for benzene is reasonable.

The time series fit of the simulated $EC_{2.5}$ concentrations to measurements for each station is depicted in Figures IX-7-1a through IX-7-1j. As evident in the plots, variations of modeled concentrations matched well with measurements. As expected, the model has difficulty in predicting extreme high and low concentrations.

Table IX-7-1
Station Observed and CAMx Simulated MATES V Average Concentrations

Compound	Units	Anaheim			Burbank Area			Compton			Inland Valley San Bernardino		
		Obs	Model	PA	Obs	Model	PA	Obs	Model	PA	Obs	Model	PA
1,3-Butadiene	ppb	N/A	-	N/A	0.036	0.018	-50	0.095	0.017	-82	0.051	0.014	-72
Acetaldehyde	ppb	N/A	-	N/A	1.77	0.70	-61	1.48	0.55	-63	2.15	0.65	-70
As (2.5)	ng/m^3	N/A	0.17	N/A	N/A	0.13	N/A	N/A	0.28	N/A	N/A	0.22	N/A
As (TSP)	ng/m^3	0.36	0.31	-14	0.46	0.33	-28	0.44	0.59	34	0.89	0.52	-42
Benzene	ppb	N/A	-	N/A	0.22	0.27	23	0.38	0.24	-36	0.23	0.22	-4
Cd (2.5)	ng/m^3	N/A	0.43	N/A	N/A	0.39	N/A	N/A	0.80	N/A	N/A	0.59	N/A
Cd (TSP)	ng/m^3	0.24	0.49	104	0.19	0.47	147	0.25	0.86	244	0.31	0.78	151
Cr6 (TSP)	ng/m^3	0.038	0.022	-42	0.032	0.028	-13	0.061	0.029	-52	0.038	0.081	125
$EC_{2.5}$	$\mu g/m^3$	0.47	0.55	17	0.50	0.67	34	0.80	0.66	-18	0.78	0.63	-19
Formaldehyde	ppb	N/A	-	N/A	3.73	1.72	-54	2.47	1.48	-40	4.47	1.67	-63
Methylene Chloride	ppb	N/A	-	N/A	0.16	0.22	36	0.19	0.17	-10	0.19	0.15	-21
Naphthalene	ppb												
Ni (2.5)	ng/m^3	N/A	1.77	N/A	N/A	1.96	N/A	N/A	3.55	N/A	N/A	3.55	N/A
Ni (TSP)	ng/m^3	2.17	2.62	20	2.01	3.26	62	2.93	5.02	71	6.31	5.14	-19
Pb (2.5)	ng/m^3	N/A	1.11	N/A	N/A	1.56	N/A	N/A	1.36	N/A	N/A	2.24	N/A
Pb (TSP)	ng/m^3	2.72	2.46	-10	6.98	3.93	-44	4.81	3.12	-53	7.66	4.93	-36
p-Dichlorobenzene	ppb	N/A	-	N/A	0.023	0.037	61	0.030	0.023	-23	0.020	0.018	-10
Perchloroethylene	ppb	N/A	-	N/A	0.021	0.032	52	0.049	0.023	-53	0.052	0.024	-54
Trichloroethylene	ppb	N/A	-	N/A	0.024	0.019	-21	0.020	0.012	-40	0.018	0.015	-17

Table IX-7-1 (Continued)
Station Observed and CAMx Simulated MATES V Annual Average Concentrations

Compound	Units	Huntington Park			North Long Beach			Central Los Angeles			Pico Rivera		
		Obs	Model	PA	Obs	Model	PA	Obs	Model	PA	Obs	Model	PA
1,3-Butadiene	ppb	0.074	0.022	-70	0.051	0.017	-67	N/A	-	N/A	0.055	0.012	-78
Acetaldehyde	ppb	1.63	0.62	-62	1.24	0.50	-60	N/A	-	N/A	1.39	0.64	-54
As (2.5)	ng/m^3	N/A	0.24	N/A	N/A	0.46	N/A	N/A	0.20	N/A	N/A	0.18	N/A
As (TSP)	ng/m^3	0.45	0.46	2	0.38	0.69	82	0.42	0.43	2	0.66	0.41	-39
Benzene	ppb	0.31	0.26	-16	0.32	0.24	-23	N/A	-	N/A	0.25	0.23	-6
Cd (2.5)	ng/m^3	N/A	0.82	N/A	N/A	0.58	N/A	N/A	0.43	N/A	N/A	0.41	N/A
Cd (TSP)	ng/m^3	0.46	0.90	96	0.09	0.66	633	0.15	0.52	246	0.14	0.49	250
Cr6 (TSP)	ng/m^3	0.057	0.024	-58	0.034	0.029	-15	0.044	0.036	-18	0.035	0.023	-34
$EC_{2.5}$	$\mu g/m^3$	0.68	0.66	-3	0.52	0.61	17	0.71	0.78	10	0.74	0.62	-16
Formaldehyde	ppb	2.56	1.61	-37	2.08	1.42	-32	N/A	-	N/A	3.00	1.56	-48
Methylene Chloride	ppb	0.17	0.27	59	0.16	0.14	-14	N/A	-	N/A	0.16	0.17	4
Naphthalene	ppb							0.013	0.007	-46			
Ni (2.5)	ng/m^3	N/A	3.01	N/A	N/A	2.91	N/A	N/A	2.94	N/A	N/A	2.47	N/A
Ni (TSP)	ng/m^3	2.64	4.25	61	3.64	4.23	16	2.00	4.50	125	3.00	3.81	27
Pb (2.5)	ng/m^3	N/A	1.41	N/A	N/A	1.56	N/A	N/A	1.64	N/A	N/A	1.36	N/A
Pb (TSP)	ng/m^3	4.42	3.56	-19	3.19	3.18	0	5.09	4.53	-11	4.73	3.35	-29
p-Dichlorobenzene	ppb	0.033	0.028	-15	0.029	0.025	-14	N/A	-	N/A	0.026	0.021	-19
Perchloroethylene	ppb	0.032	0.028	-13	0.023	0.017	-26	N/A	-	N/A	0.031	0.021	-32
Trichloroethylene	ppb	0.022	0.015	-32	0.020	0.011	-45	N/A	-	N/A	0.014	0.012	-14

Table IX-7-1 (Continued)
Station Observed and CAMx Simulated MATES V Average Concentrations

Compound	Units	Rubidoux			West Long Beach		
		Obs	Model	PA	Obs	Model	PA
1,3-Butadiene	ppb	N/A	-	N/A	0.062	0.022	-65
Acetaldehyde	ppb	N/A	-	N/A	1.16	0.51	-56
As (2.5)	ng/m^3	N/A	0.09	N/A	N/A	0.80	N/A
As (TSP)	ng/m^3	0.67	0.26	-61	0.47	1.11	136
Benzene	ppb	N/A	-	N/A	0.30	0.27	-10
Cd (2.5)	ng/m^3	N/A	0.22	N/A	N/A	0.88	N/A
Cd (TSP)	ng/m^3	0.59	0.30	-49	0.77	0.94	22
Cr6 (TSP)	ng/m^3	0.026	0.012	-54	0.035	0.037	6
$EC_{2.5}$	$\mu g/m^3$	0.69	0.42	-39	0.72	0.71	1
Formaldehyde	ppb	N/A	-	N/A	2.33	1.64	-30
Methylene Chloride	ppb	N/A	-	N/A	0.16	0.13	-19
Naphthalene	ppb	0.008	0.003	-100			
Ni (2.5))	ng/m^3	N/A	1.11	N/A	N/A	4.64	N/A
Ni (TSP)	ng/m^3	2.41	1.88	-22	4.32	6.84	58
Pb (2.5)	ng/m^3	N/A	0.88	N/A	N/A	1.87	N/A
Pb (TSP)	ng/m^3	4.47	2.63	-41	4.14	3.50	-15
p-Dichlorobenzene	ppb	N/A	-	N/A	0.026	0.024	8
Perchloroethylene	ppb	N/A	-	N/A	0.024	0.017	-29
Trichloroethylene	ppb	N/A	-	N/A	0.030	0.012	-60

Table IX-7-2
MATES V $EC_{2.5}$ Model Performance

Location	Observed ($\mu g/m^3$)	*Modeled ($\mu g/m^3$)	Prediction Accuracy	Mean Bias ($\mu g/m^3$)	Mean Error ($\mu g/m^3$)	Normalized Mean Bias	Normalized Mean Error
Anaheim	0.47	0.55	16	0.08	0.21	0.78	0.89
Burbank Area	0.50	0.67	33	0.17	0.33	1.06	1.22
Compton	0.80	0.66	-17	-0.14	0.42	0.59	0.86
Inland Valley San Bernardino	0.78	0.63	-20	-0.15	0.33	0.05	0.48
Huntington Park	0.68	0.66	-2	-0.02	0.32	0.74	0.97
Long Beach	0.52	0.62	19	0.10	0.28	1.53	1.67
Central L.A.	0.71	0.78	9	0.07	0.27	0.63	0.76
Pico Rivera	0.74	0.62	-16	-0.13	0.25	0.11	0.41
Rubidoux	0.69	0.42	-40	-0.27	0.35	0.06	0.60
West Long Beach	0.72	0.71	-2	-0.01	0.38	0.89	1.16
All Stations	0.66	0.63	-5	-0.03	0.31	0.64	0.90

Table IX-7-3
MATES V Simulation Performance Statistics for Benzene

Location	Observed (ppb)	Samples	Predicted (ppb)	PA	Mean Bias (ppb)	Mean Error (ppb)	Normalized Mean Bias	Normalized Mean Error
Anaheim								
Burbank Area	0.22	60	0.27	23	-0.06	0.08	0.33	0.41
Compton	0.38	61	0.24	-36	-0.14	0.20	0.09	0.52
Inland Valley San Bernardino	0.23	61	0.22	-4	-0.01	0.06	0.07	0.27
Huntington Park	0.31	60	0.26	-17	-0.05	0.11	0.08	0.35
North Long Beach	0.32	58	0.24	-24	-0.08	0.15	0.28	0.61
Central L.A.								
Pico Rivera	0.25	53	0.23	-8	-0.02	0.08	0.14	0.37
Rubidoux								
West Long Beach	0.30	58	0.27	-8	-0.03	0.13	0.35	0.61
All Stations	0.29	411	0.25	-13	-0.04	0.12	0.19	0.45

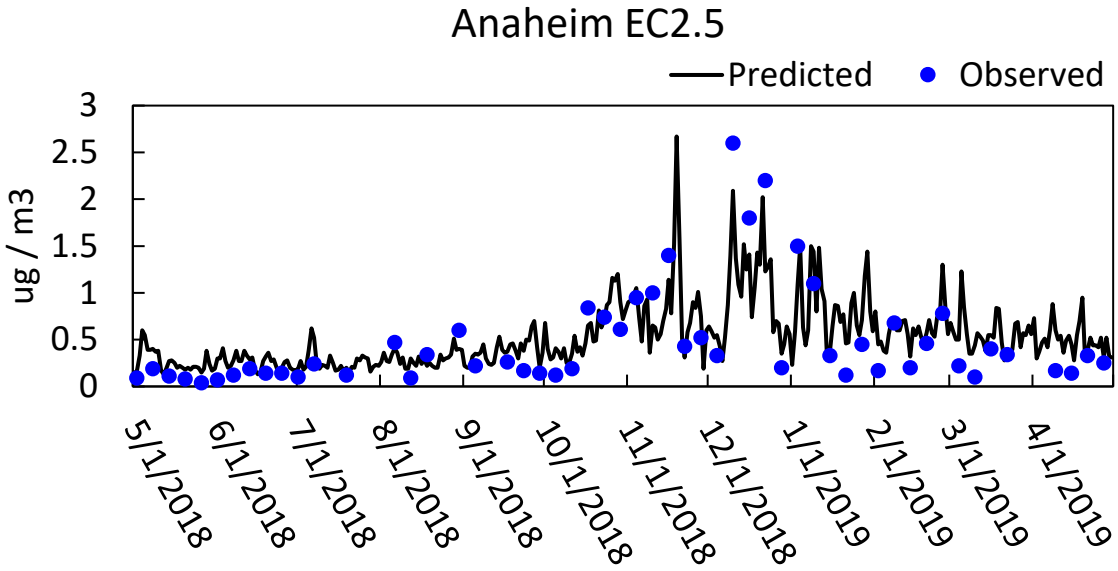

Figure IX-7-1a
$EC_{2.5}$ Time Series: Simulated vs. Measured at Anaheim

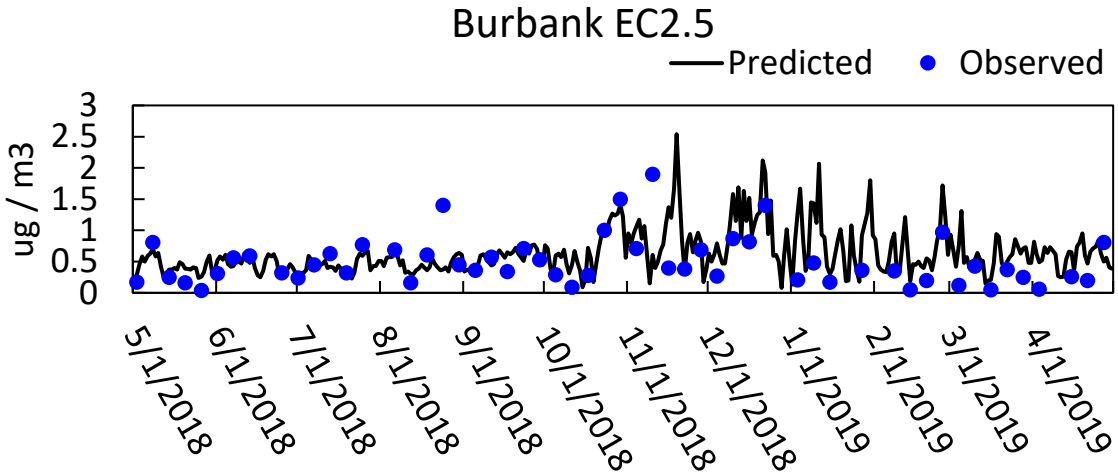

Figure IX-7-1b
$EC_{2.5}$ Time Series: Simulated vs. Measured at Burbank Area

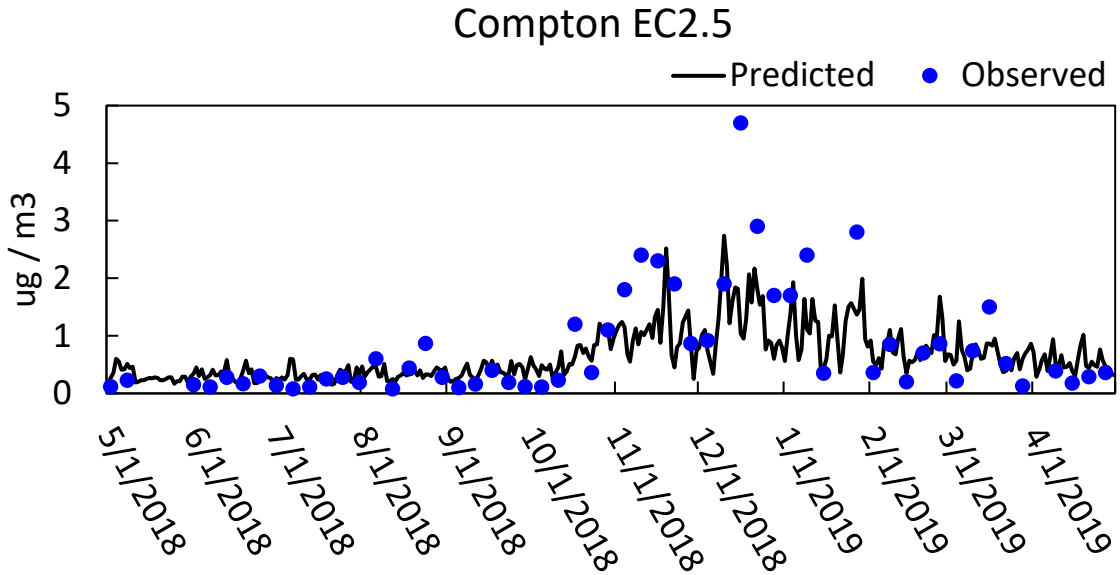

Figure IX-7-1c
$EC_{2.5}$ Time Series: Simulated vs. Measured at Compton

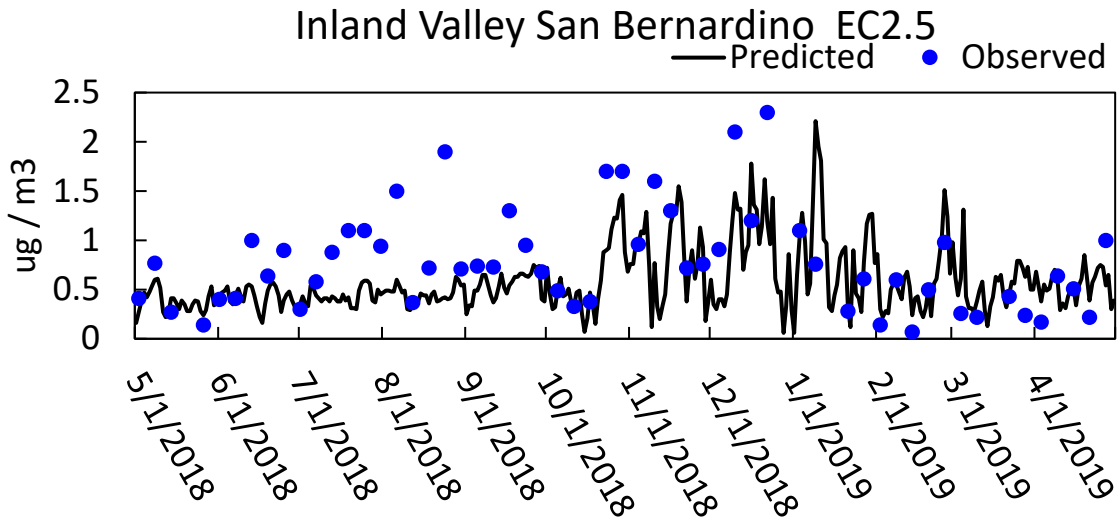

Figure IX-7-1d
$EC_{2.5}$ Time Series: Simulated vs. Measured at Inland Valley San Bernardino

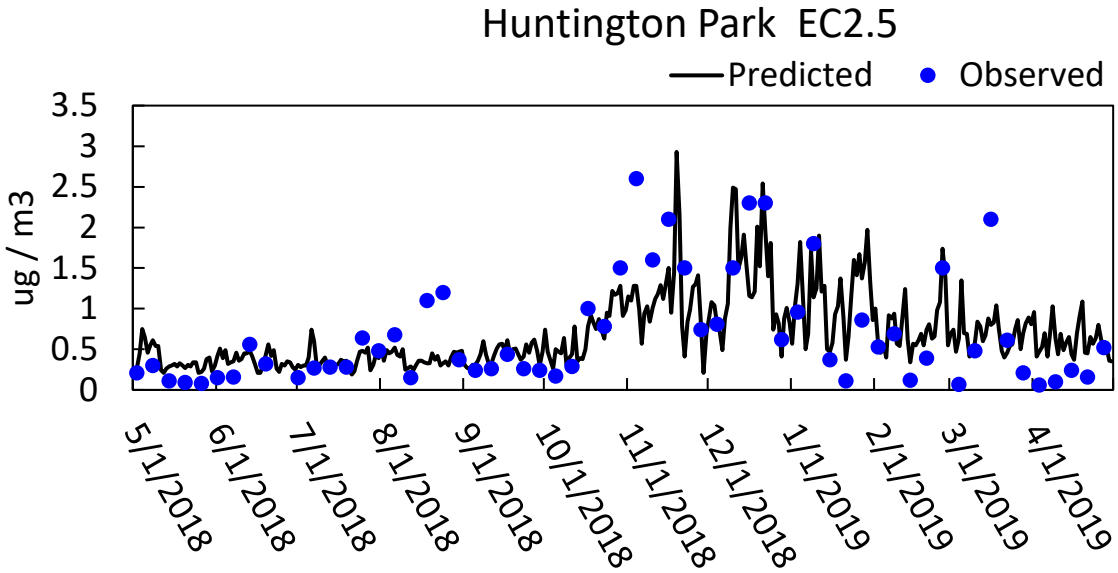

Figure IX-7-1e
$EC_{2.5}$ Time Series: Simulated vs. Measured at Huntington Park

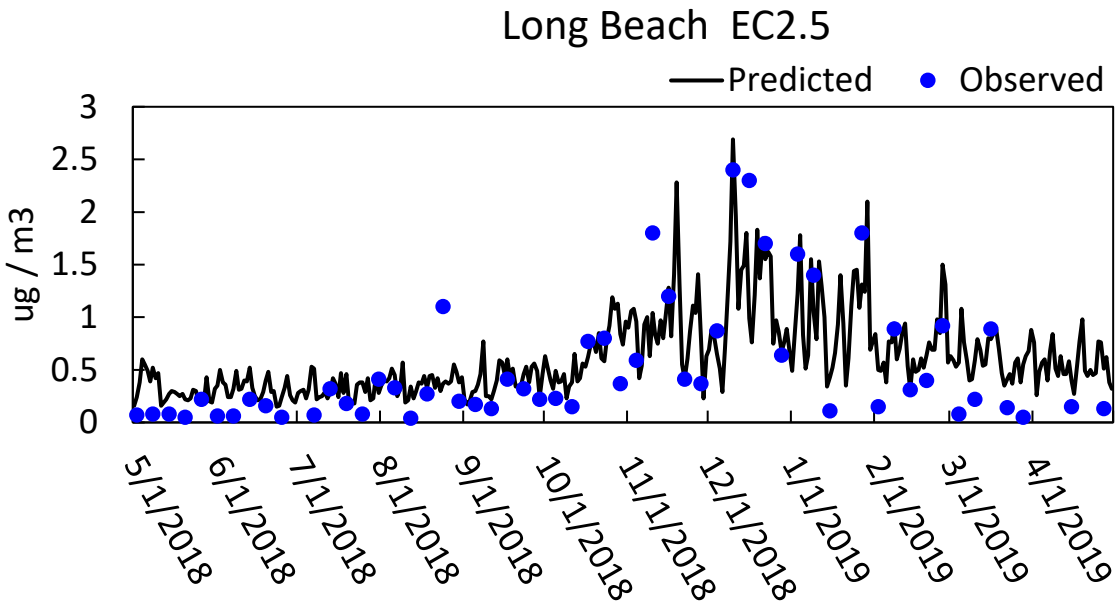

Figure IX-7-1f
$EC_{2.5}$ Time Series: Simulated vs. Measured at Long Beach

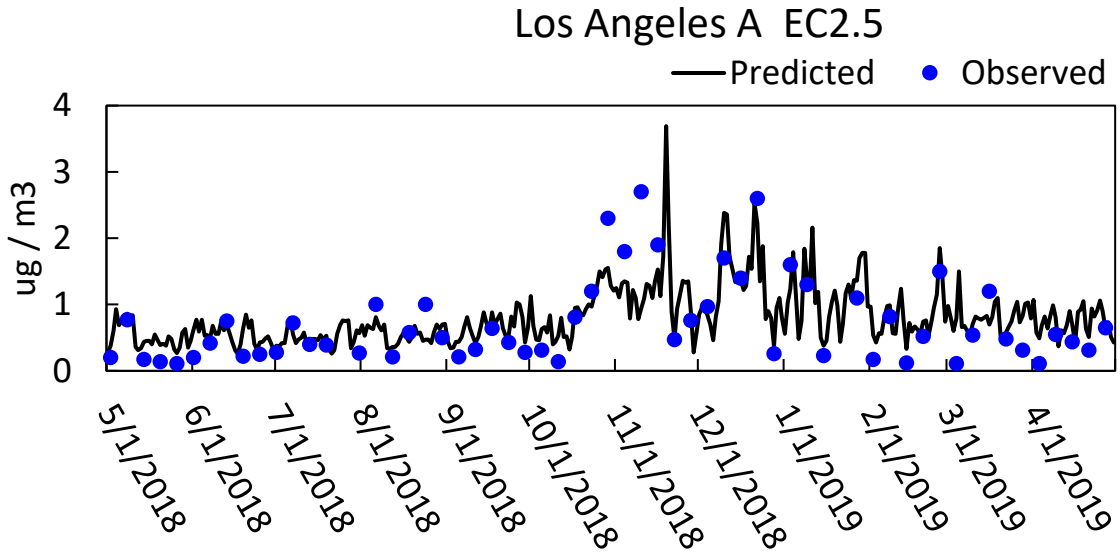

Figure IX-7-1g
$EC_{2.5}$ Time Series: Simulated vs. Measured at Central Los Angeles

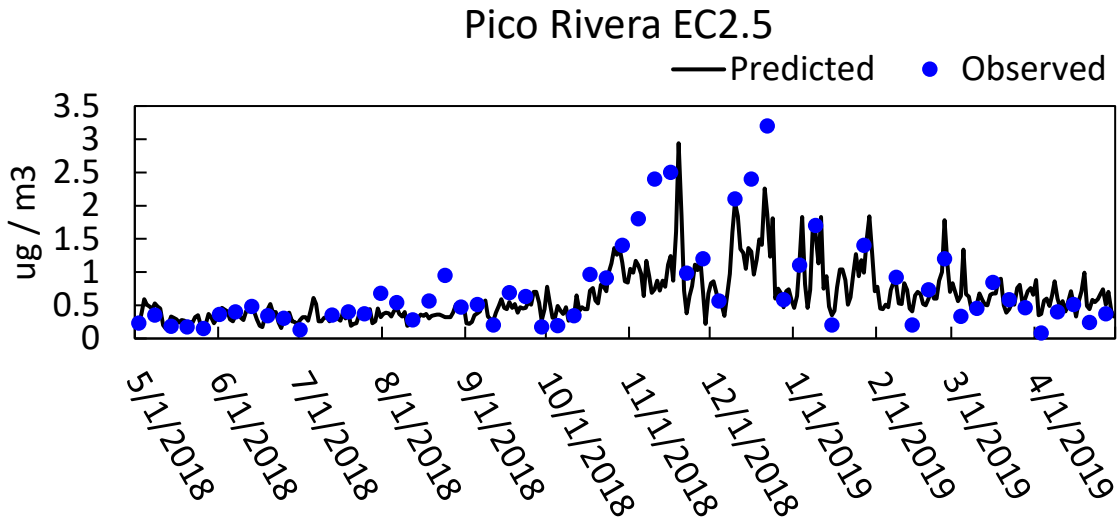

Figure IX-7-1h
$EC_{2.5}$ Time Series: Simulated vs. Measured at Pico Rivera

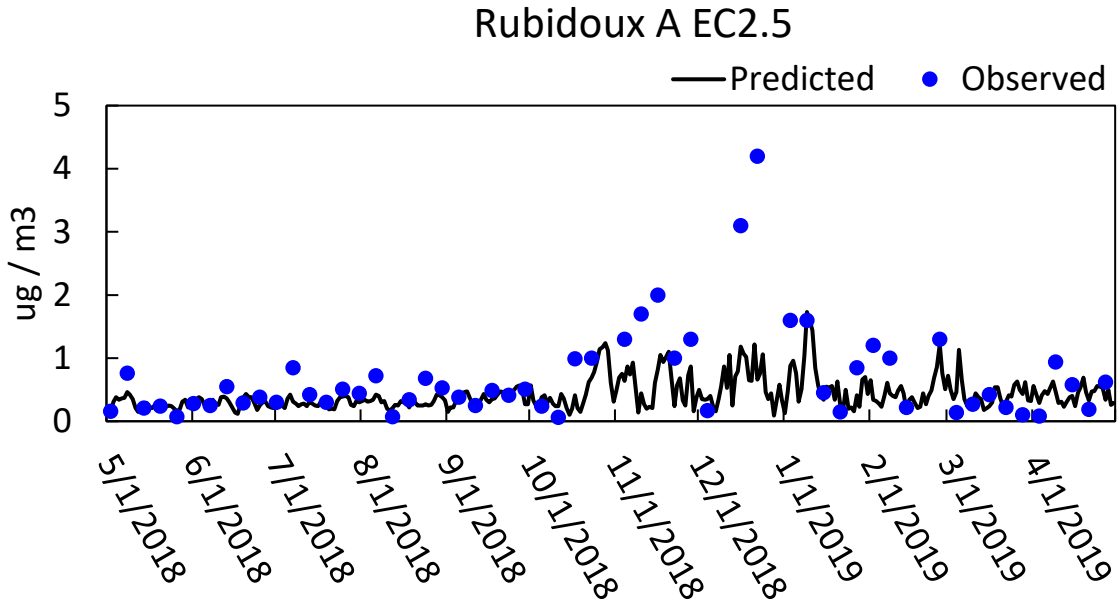

Figure IX-7-1i
$EC_{2.5}$ Time Series: Simulated vs. Measured at Rubidoux

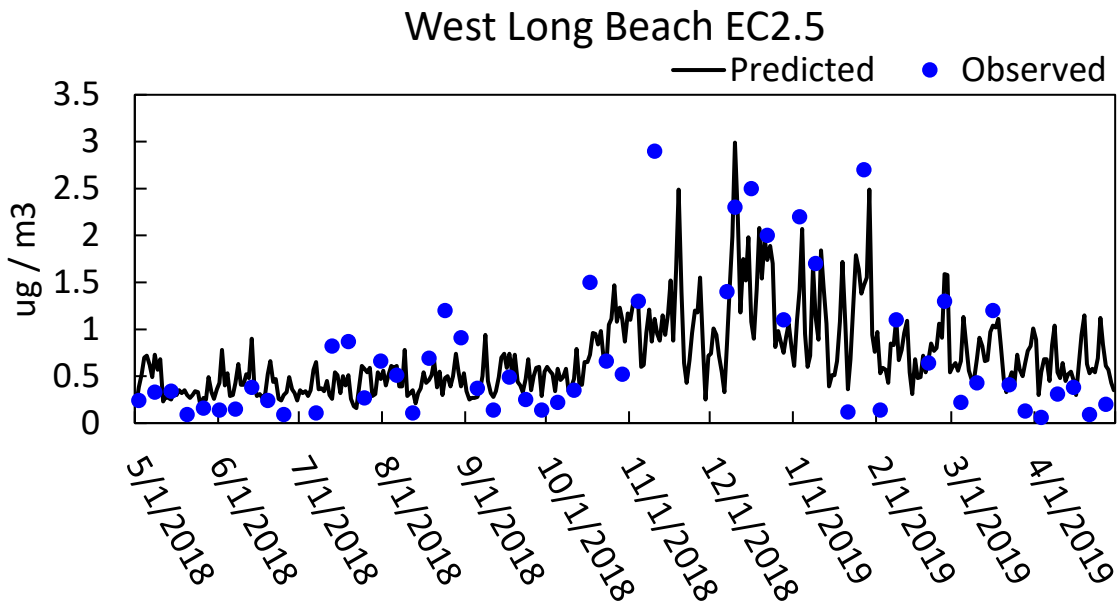

Figure IX-7-1j
$EC_{2.5}$ Time Series: Simulated vs. Measured at West Long Beach

IX.7.2 Comparison with MATES IV Simulation

Tables IX-7-4 and IX-7-5 provide a comparison of the 2018-2019 MATES V and 2012-2013 MATES IV model performance for $EC_{2.5}$ and benzene, respectively. Listed in each table are PA, bias, and mean error. As presented in tables, compared to MATES IV modeling, where modeling exhibited an overall tendency to overpredict $EC_{2.5}$. MATES V modeling does not show a significant under or over prediction tendencies. Historically, regional modeling in the SCAB showed under predictions in the Rubidoux and Burbank areas, as evidenced by the MATES IV results. MATES V modeling, while still shows underprediction in the Rubidoux area, it no longer underpredicts the Burbank Area, indicating changes in the behavior of meteorological modeling. Overall, the MATES V model performance is on par or better compared to MATES IV.

Table IX-7-4
Comparative Simulation Performance Statistics for **$EC_{2.5}$**

	MATES IV (2012-2013)					MATES V (2018-2019)				
Location	Observed Days ($\mu g/m^3$)	Modeled Sampling Days ($\mu g/m^3$)	PA	Bias ($\mu g/m^3$)	Mean Error ($\mu g/m^3$)	Observed Days ($\mu g/m^3$)	Modeled Sampling Days ($\mu g/m^3$)	PA	Bias ($\mu g/m^3$)	Mean Error ($\mu g/m^3$)
Anaheim	0.90	1.10	22	0.20	0.56	0.47	0.55	16	0.08	0.21
Burbank Area	1.32	1.19	-9	-0.12	0.64	0.50	0.67	33	0.17	0.33
Compton	1.06	1.48	39	0.42	0.76	0.80	0.66	-17	-0.14	0.42
Inland Valley San Bernardino	1.38	1.13	-18	-0.25	0.46	0.78	0.63	-20	-0.15	0.33
Huntington Park	1.30	1.70	31	0.40	0.67	0.68	0.66	-2	-0.02	0.32
Long Beach	0.91	1.45	59	0.53	0.80	0.52	0.62	19	0.10	0.28
Central L.A.	1.23	1.81	47	0.58	0.70	0.71	0.78	9	0.07	0.27
Pico Rivera	1.39	1.30	-6	-0.09	0.48	0.74	0.62	-16	-0.13	0.25
Rubidoux	1.11	0.98	-12	-0.13	0.40	0.69	0.42	-40	-0.27	0.35
West Long Beach	1.13	1.88	67	0.75	1.00	0.72	0.71	-2	-0.01	0.38

Table IX-7-5
Comparative Simulation Performance Statistics for Benzene

	MATES IV (2012-2013)					MATES V (2018-2019)				
Location	Observed Days (ppb)	Modeled Sampling Days (ppb)	PA	Bias (ppb)	Mean Error (ppb)	Observed Days (ppb)	Modeled Sampling Days (ppb)	PA	Bias (ppb)	Mean Error (ppb)
Anaheim	0.33	0.28	-14	-0.05	0.16					
Burbank Area	0.46	0.28	-38	-0.17	0.22	0.22	0.27	23	-0.06	0.08
Compton	0.50	0.28	-43	-0.21	0.26	0.38	0.24	-36	-0.14	0.20
Inland Valley San Bernardino.	0.29	0.22	-24	-0.07	0.09	0.23	0.22	--4	-0.01	0.06
Huntington Park	0.53	0.33	-38	-0.20	0.22	0.31	0.26	-17	-0.05	0.11
Long Beach	0.33	0.30	-10	-0.03	0.10	0.32	0.24	-24	-0.08	0.15
Central L.A.	0.40	0.37	-8	-0.03	0.12					
Pico Rivera	0.35	0.27	-21	-0.07	0.12	0.25	0.23	-8	-0.02	0.08
Rubidoux	0.28	0.21	-24	-0.07	0.10					
West Long Beach	0.36	0.41	15	0.05	0.20	0.30	0.27	-8	-0.03	0.13

IX.7.3 Simulation Evaluation Averaged Over the Monitoring Network

For this comparison, the monitored data for ten stations are combined to provide an estimate of average Basin-wide conditions for the two sampling periods. Table IX-7-6 summarizes the network average measured and predicted pollutant concentrations. For gaseous species concentrations, measurement data from Anaheim, Central Los Angeles and Rubidoux were missing, so only the data from the remaining seven monitoring sites were presented. Measured concentrations of naphthalene were available for Central Los Angeles, and Rubidoux. Each of the four counties is represented by at least one station. The stations' measured and simulated average concentrations provide an estimate of the regional profile but with a bias towards impacts to the coastal communities in the heavily transited areas of the Basin. Moreover, the assessment provides a direct comparison for model performance evaluation.

For MATES V, the model simulated concentrations of particulate matter species, such as $EC_{2.5}$ and TSP metals were consistent with measured data. The model was unable to predict the increased carbonyl concentrations, formaldehyde and acetaldehyde, compared to MATES IV. Concentrations of perchloroethylene, p-dichlorobenzene, trichloroethylene, 1,3-butadiene and naphthalene have become low enough that model performances for those pollutants are immaterial. Benzene and methylene concentrations were well simulated.

Table IX-7-6
Toxic Compounds Simulated and Measured Ten-Station Annual Average Concentrations
For MATES IV and MATES V periods using CAMX RTRAC

Compound	Units	2012-2013 MATES IV		2018-2019 MATES V	
		Measured Annual Average	Simulated Annual Average***	Measured Annual Average	Simulated Annual Average***
$EC_{2.5}$	$\mu g/m^3$	0.96	1.39	0.66	0.63
Cr 6 (TSP)	ng/m^3	0.05	0.18	0.040	0.032
As (2.5)	ng/m^3	N/A	0.66	N/A	0.27
As (TSP)	ng/m^3	0.44	1.07	0.52	0.51
Cd (2.5)	ng/m^3	N/A	0.38	N/A	0.55
Cd (TSP)	ng/m^3	0.13	0.56	0.32	0.64
Ni (2.5))	ng/m^3	N/A	4.58	N/A	2.83
Ni (TSP)	ng/m^3	2.98	6.64	3.14	4.15
Pb (2.5)	ng/m^3	N/A	2.10	N/A	1.52
Pb (TSP)	ng/m^3	4.69	5.26	4.80	3.51

Benzene*	ppb	0.33	0.29	0.29	0.25
Perchloroethylene*	ppb	0.03	0.08	0.03	0.02
p-Dichlorobenzene*	ppb	0.02	0.04	0.03	0.03
Methylene Chloride*	ppb	0.46	0.24	0.17	0.18
Trichloroethylene*	ppb	0.02	0.04	0.02	0.01
1,3-Butadiene*	ppb	0.09	0.04	0.06	0.02
Formaldehyde*	ppb	1.78	1.91	2.95	1.59
Acetaldehyde*	ppb	0.71	0.95	1.55	0.60
Naphthalene**	ppb	0.02	0.01	0.01	0.01

* Seven station average
** Two station average
*** Average of days with measurements

IX.7.4 Simulation Estimated Spatial Concentration Fields

Figures IX-7-2a through IX-7-2u depict the CAMx projected annual average concentration distributions of selected toxic compounds as well as the impacts of five emissions categories of diesel particulates in the Basin. The highest concentration (1.13 $\mu g/m^3$) was simulated to occur around the Ports of Los Angeles and Long Beach. In general, the distribution of diesel particulates is aligned with the transportation corridors including freeways, major arterials and rail rights-of-way. The peak diesel concentration is much lower than the previous MATES, due in a large part to emission reductions in various categories of on-road and other mobile sources. Figures IX-7-2h and IX-7-2i provide the distributions of benzene and 1,3-butadiene, respectively, whereby the toxic compounds are almost uniformly distributed throughout the Basin, reflecting patterns of light-duty vehicles fuel consumption since benzene and 1,3-butadiene emissions are mostly from gasoline combustion. Benzene emissions are primarily from on- and off-road mobile sources, with some portions emitted from refineries located near the coast. The modeled benzene concentrations mostly reflect patterns of the mobile sources with marginal enhancement near the coastal area. The 7 monitoring stations (Burbank Area, Compton, Huntington Park, Inland Valley San Bernardino, Long Beach, Pico Rivera and West Long Beach) showed the measured annual concentrations for benzene ranging from 0.22 ppb (at Burbank Area) to 0.38 ppb (at Compton), with a 7-station average of 0.29 ppb. Model prediction at those stations ranges from 0.21 to 0.28 ppb with a 7-station average of 0.25 ppb, which are in reasonable agreement with the measurements.

The ambient concentrations of formaldehyde in the Basin are attributed to direct emissions, combustion sources, and secondary formation in the atmosphere. The formaldehyde concentrations shown in Figure IX-7-2j depict a spatial distribution indicative of its sources, with measurable concentrations in the heavily-traveled western and central Basin, with additional elevated levels in the downwind areas of the Basin that are impacted by higher levels of photochemistry and ozone formation. While the emissions from primary combustion sources decreased by approximately 8% since MATES IV, the MATES V measurements indicated the ambient formaldehyde concentrations increased compared to MATES IV. This increase means

that the formaldehyde concentrations are being driven by secondary formation instead of direct emissions, indicating a complex chemistry involved in formaldehyde formation and depletion. It is also possible that uncertainties in emissions inventory and air quality modeling could contribute to the discrepancy. The modeled concentrations from the 7 monitoring stations averaged at 1.61 ppb, lower than the measured values averaged at 2.95 ppb.

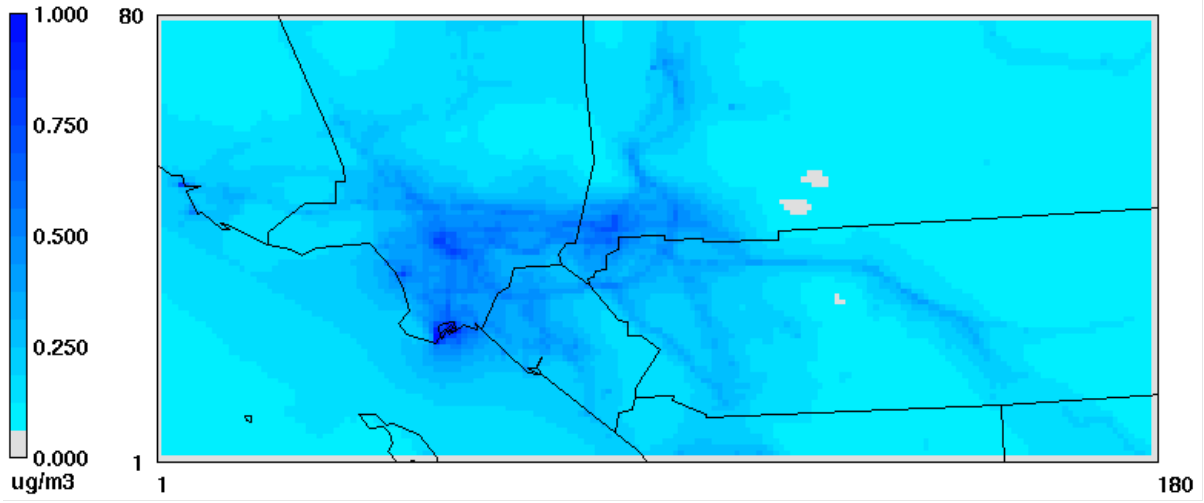

Figure IX-7-2a
CAMx simulated 2018 annual average Diesel PM

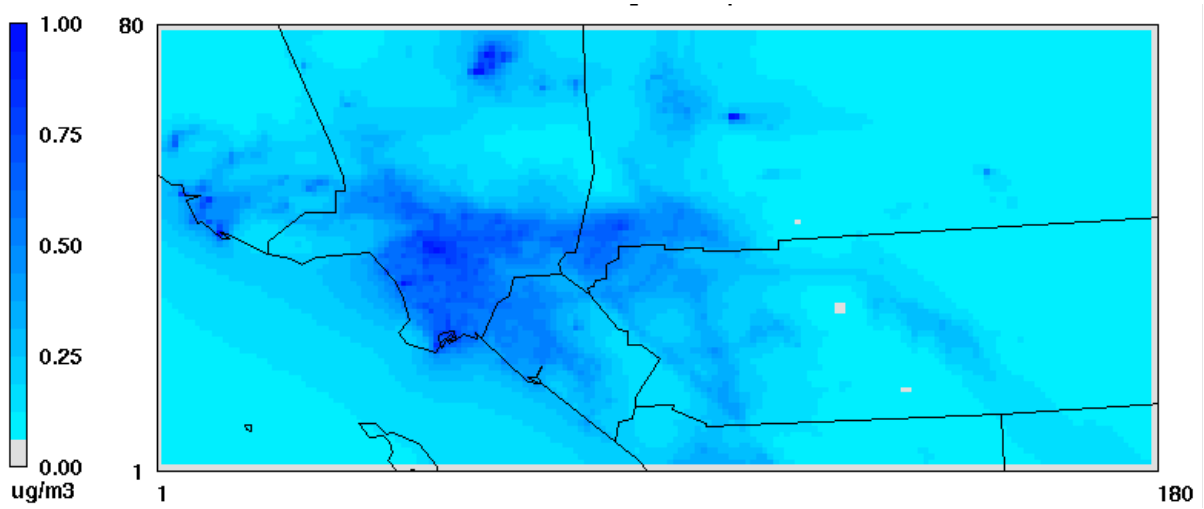

Figure IX-7-2b
CAMx simulated 2018 annual average Elemental Carbon $PM_{2.5}$

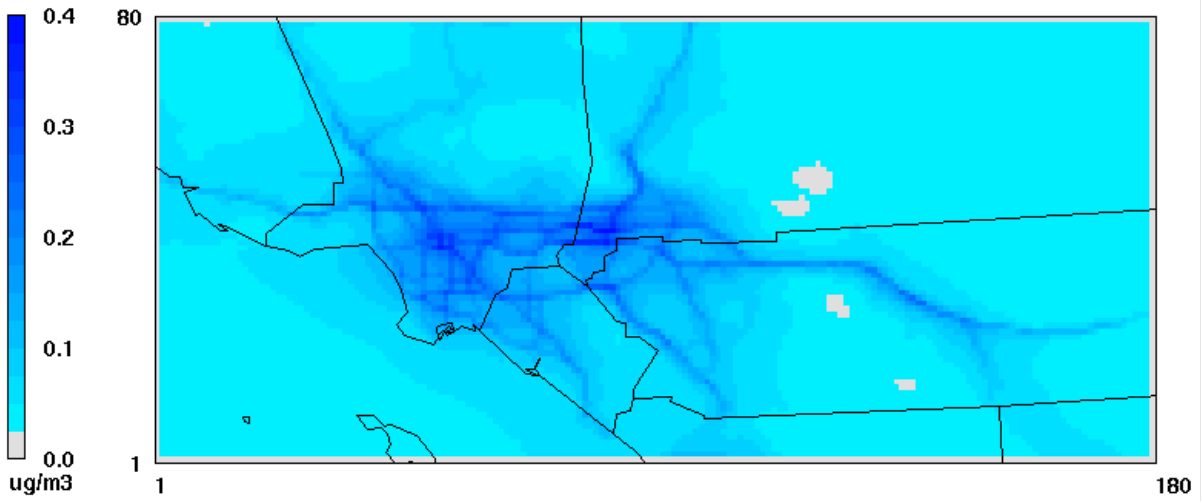

Figure IX-7-2c
CAMx simulated 2018 annual average On-Road Diesel PM

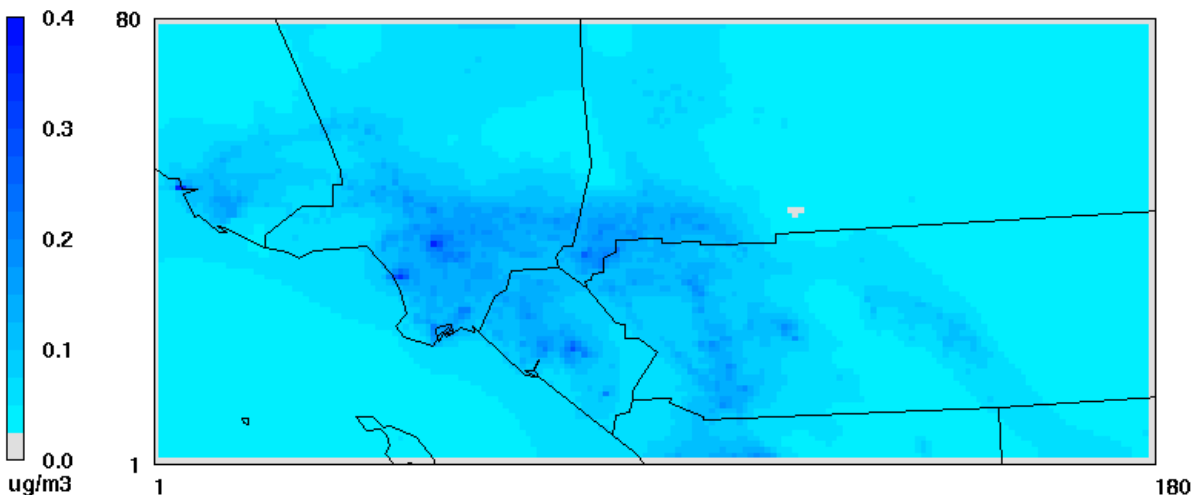

Figure IX-7-2d
CAMx simulated 2018 annual average Off-Road Diesel PM

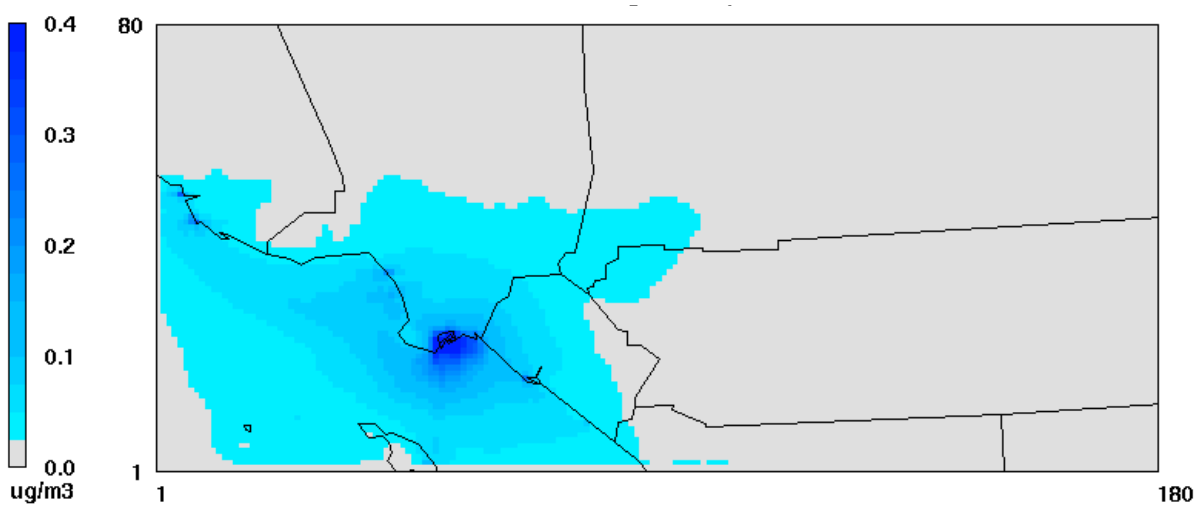

Figure IX-7-2e
CAMx simulated 2018 annual average Diesel PM from OGV and CHC

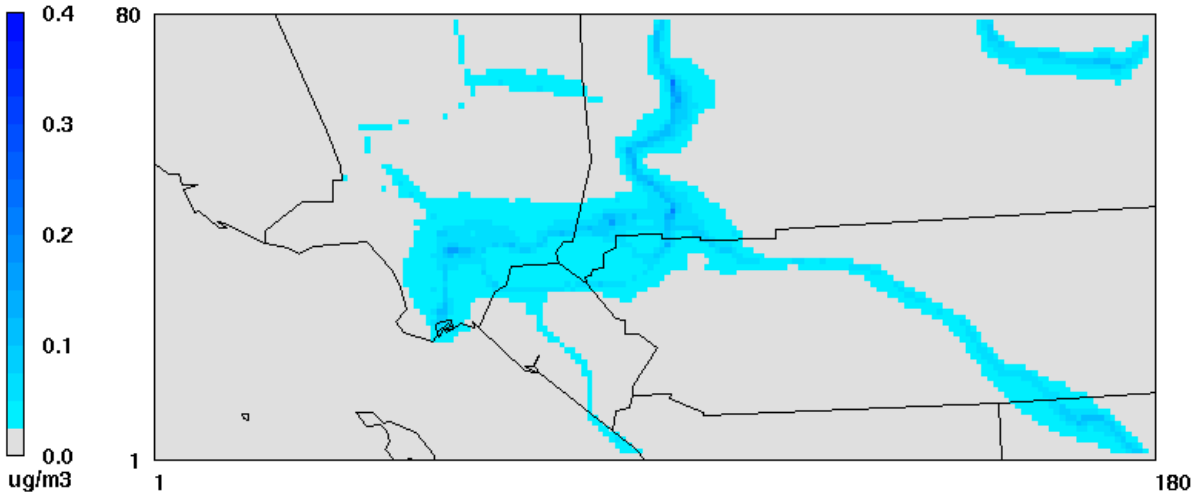

Figure IX-7-2f
CAMx simulated 2018 annual average Diesel PM from Trains

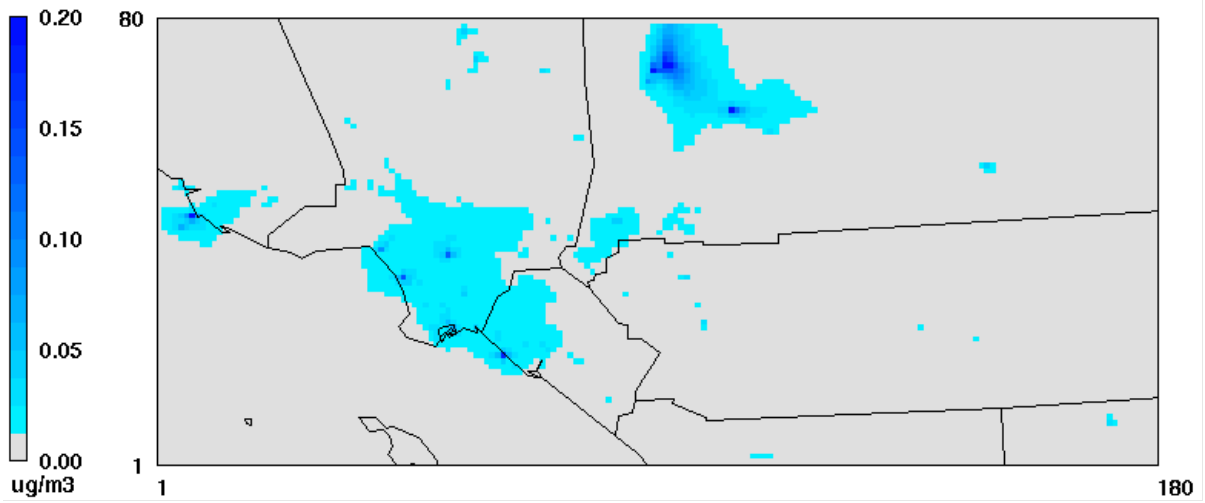

Figure IX-7-2g
CAMx simulated 2018 annual average diesel PM from stationary sources.

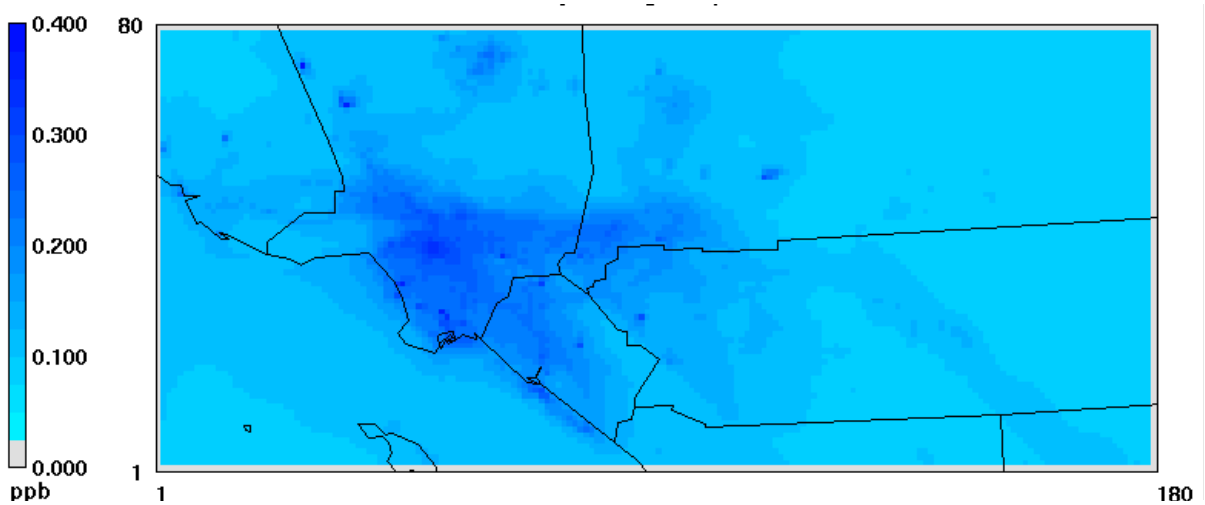

Figure IX-7-2h
CAMx simulated 2018 annual average benzene

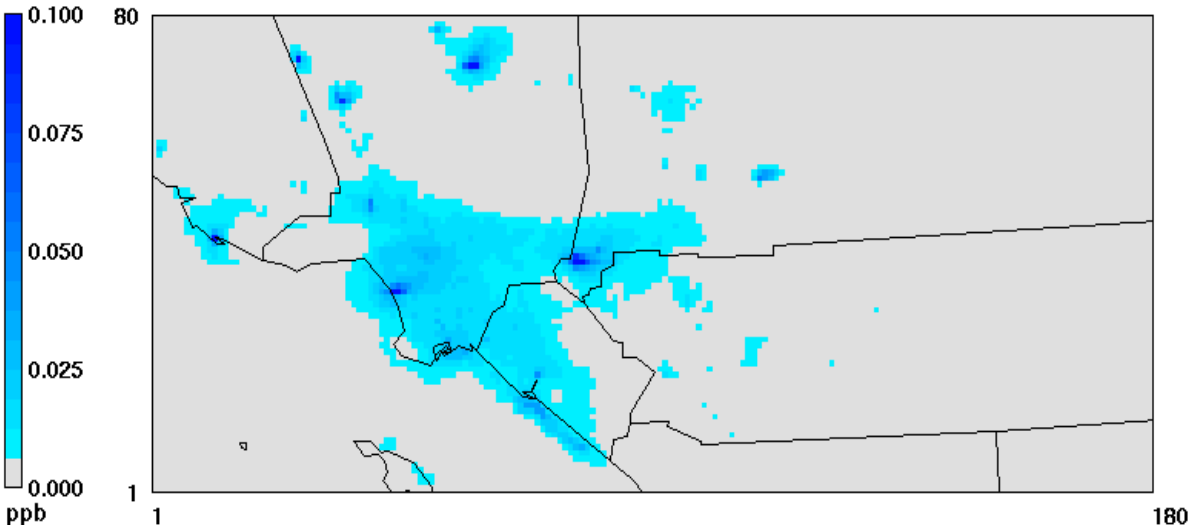

Figure IX-7-2i
CAMx simulated 2018 annual average 1,3-butadiene

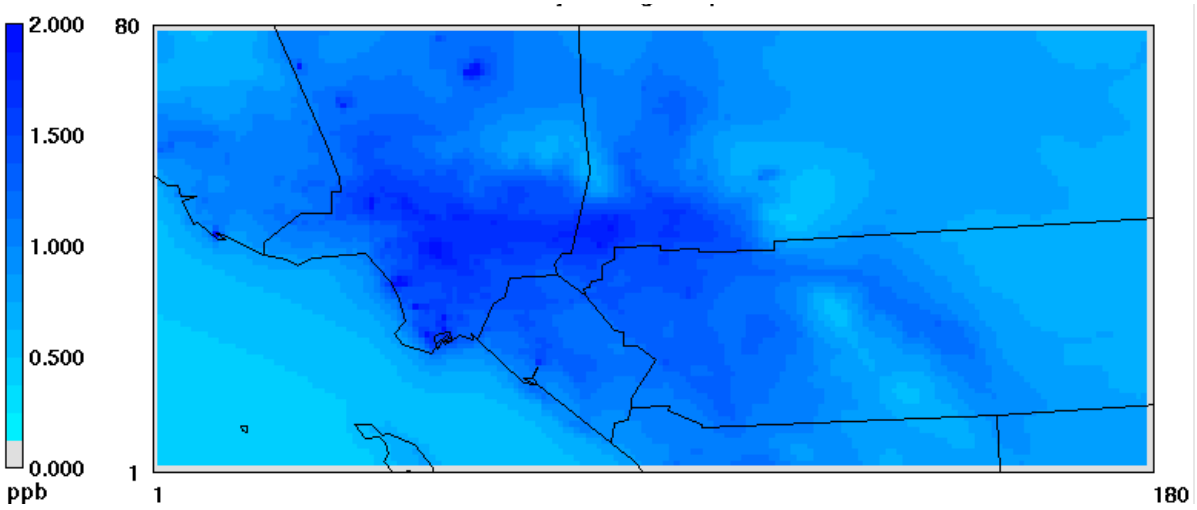

Figure IX-7-2j
CAMx simulated 2018 annual average for total formaldehyde

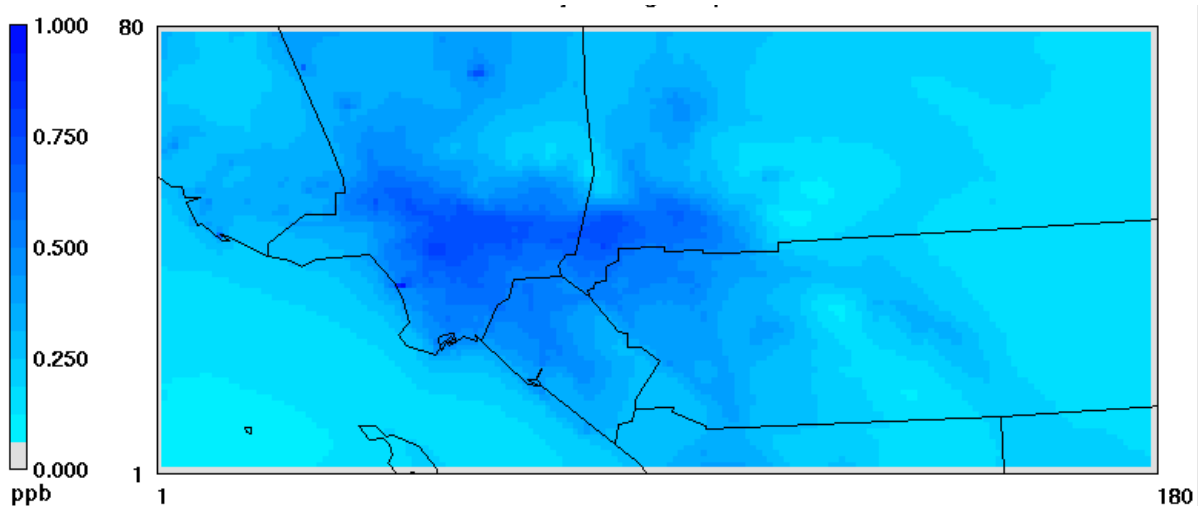

Figure IX-7-2k
CAMx simulated 2018 annual average acetaldehyde

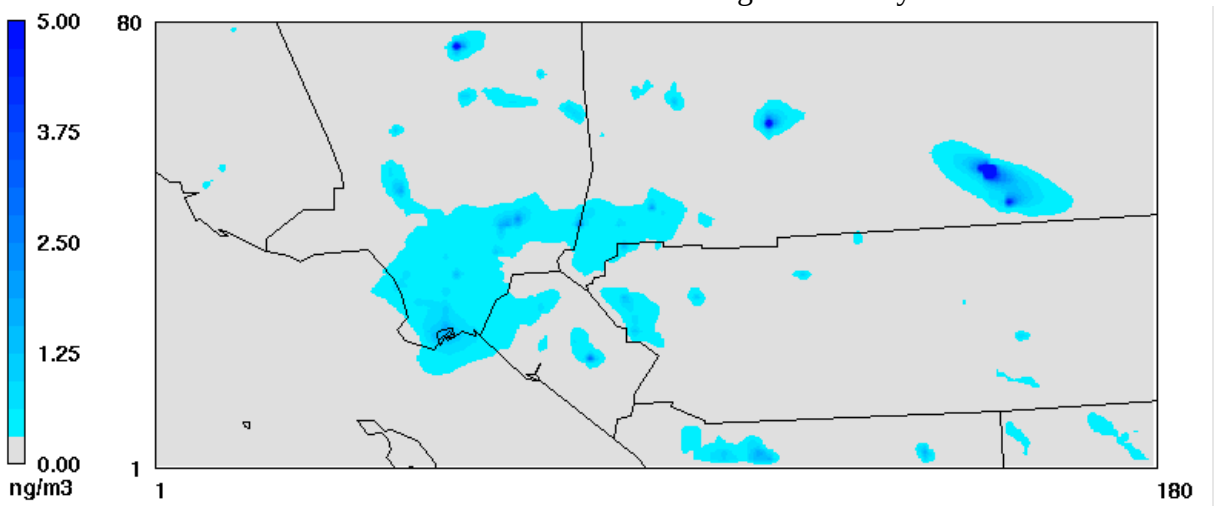

Figure IX-7-2l
CAMx simulated 2018 annual average arsenic TSP

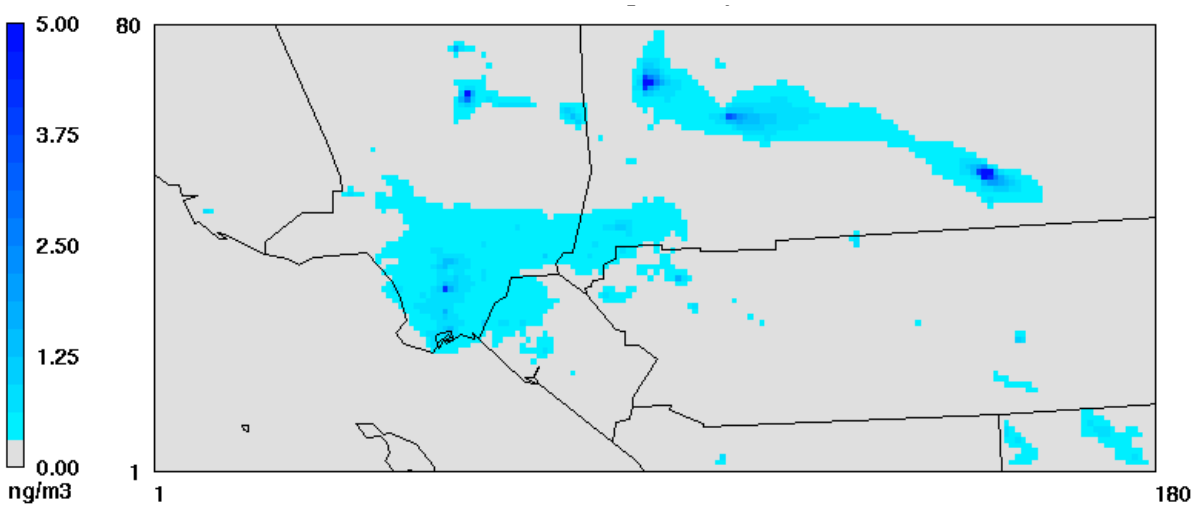

Figure IX-7-2m
CAMx simulated 2018 annual average cadmium TSP

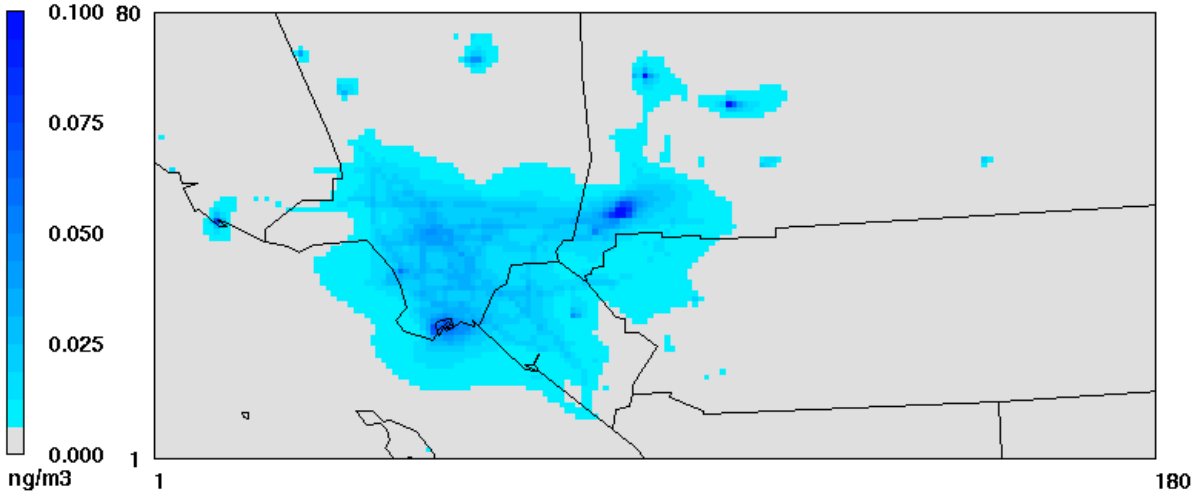

Figure IX-7-2n
CAMx simulated 2018 annual average hexavalent chromium TSP

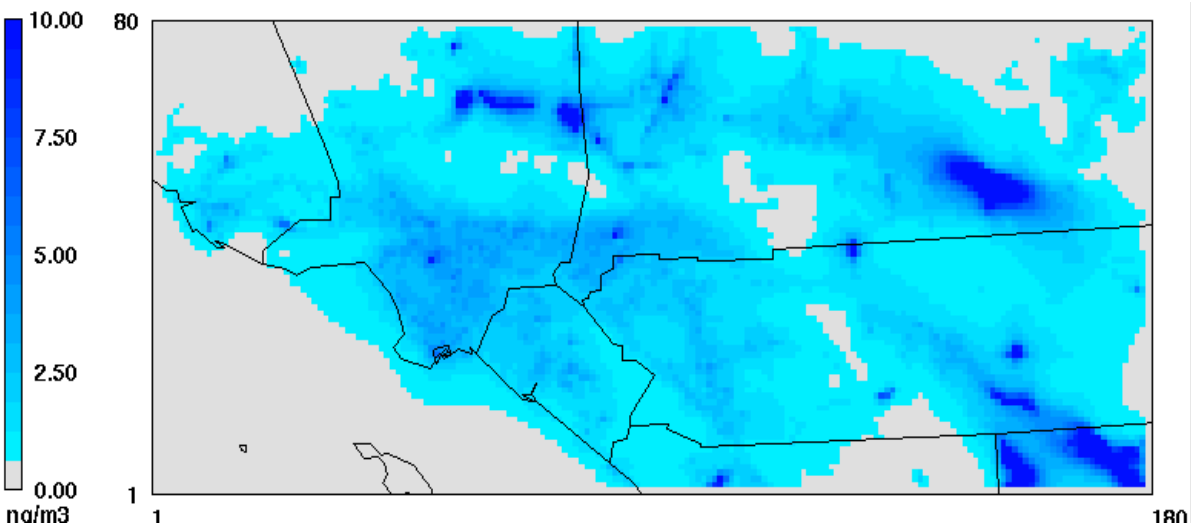

Figure IX-7-2o
CAMx simulated 2018 annual average lead TSP

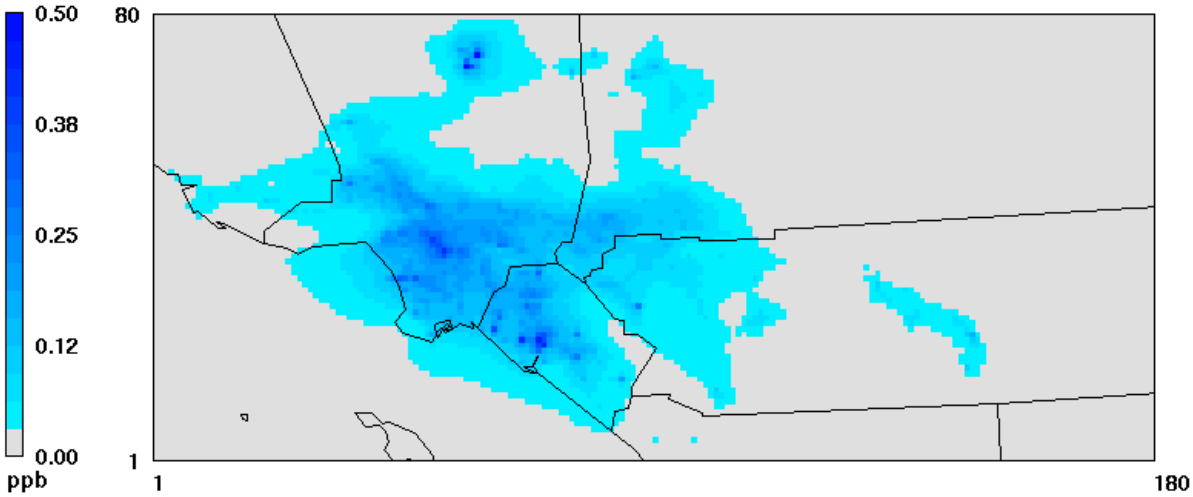

Figure IX-7-2p
CAMx simulated 2018 annual average methylene chloride

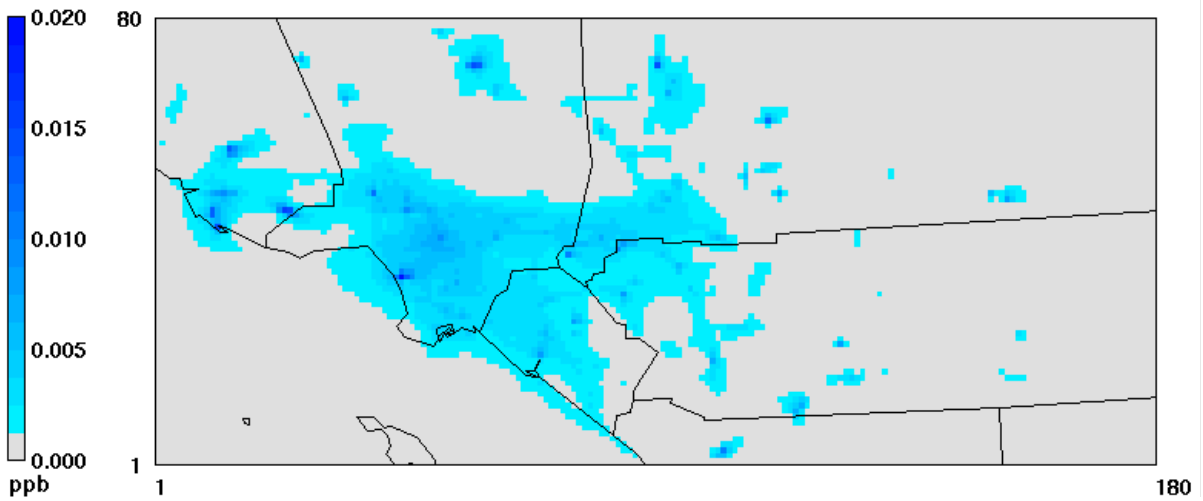

Figure IX-7-2q
CAMx simulated 2018 annual average naphthalene

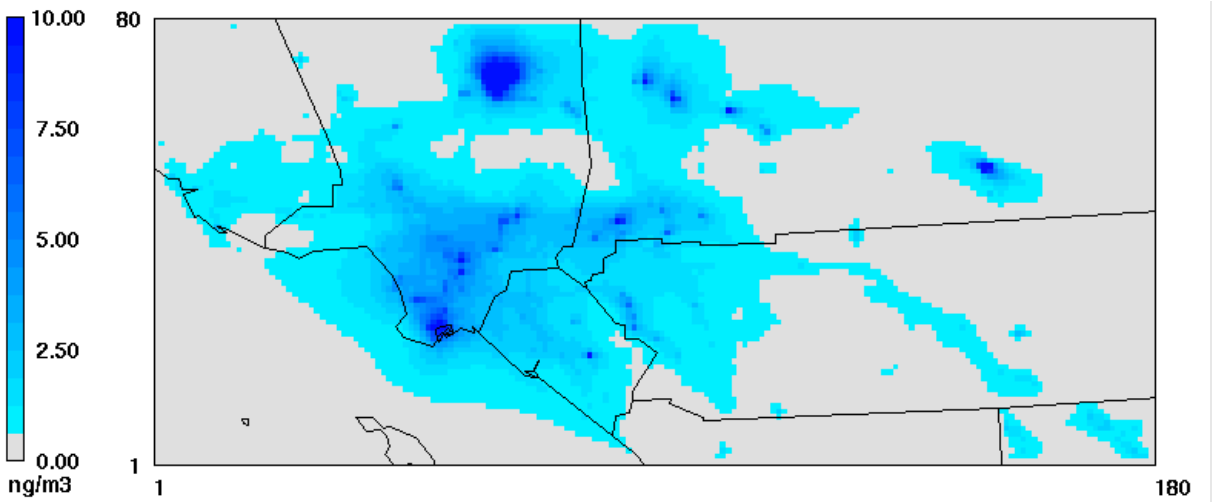

Figure IX-7-2r
CAMx simulated 2018 annual average nickel TSP

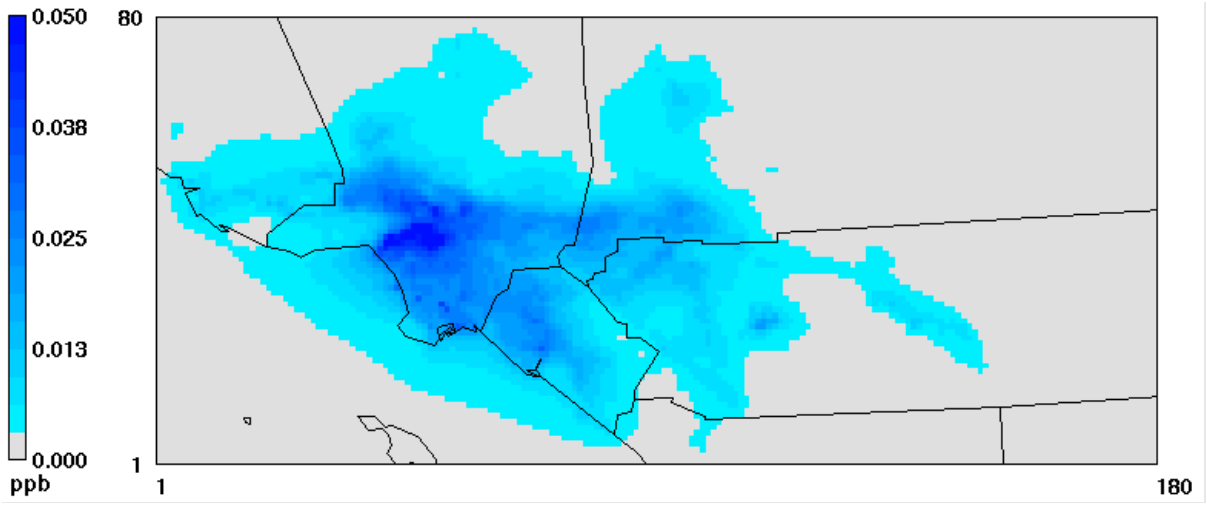

Figure IX-7-2s
CAMx simulated 2018 annual average p-dichlorobenzene

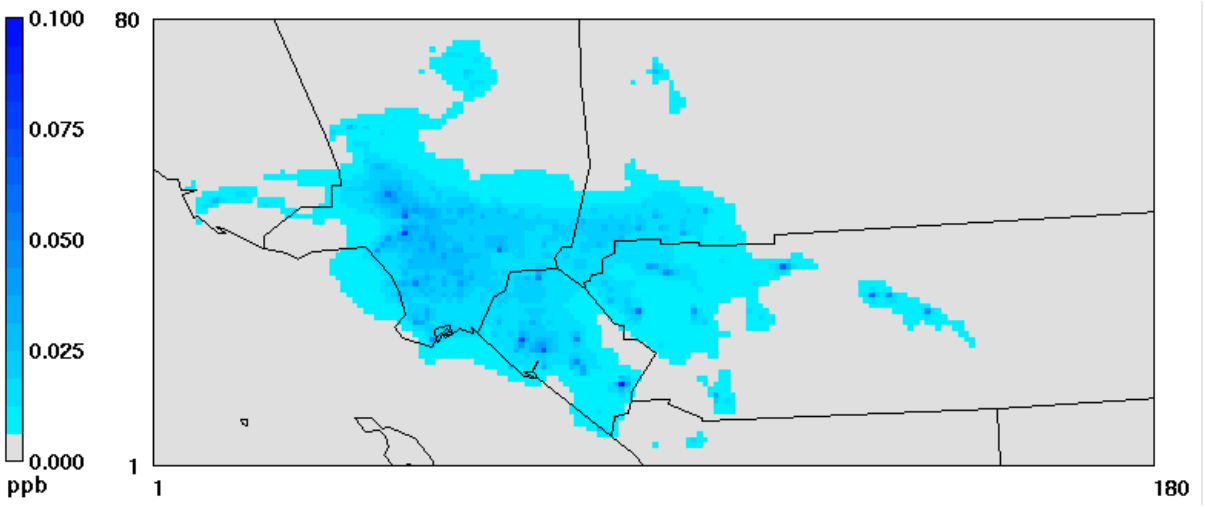

Figure IX-7-2t
CAMx simulated 2018 annual average perchloroethylene

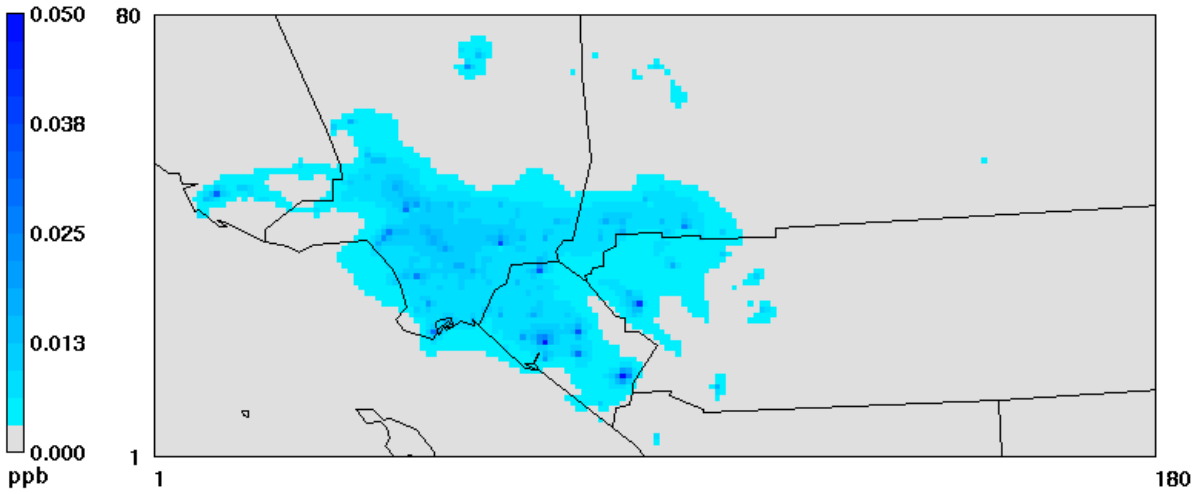

Figure IX-7-2u
CAMx simulated 2018 annual average trichloroethylene

IX.7.5 Estimation of Risk

Figure IX-7-3 depicts the distribution of risk estimated from the predicted annual average concentrations of the key toxic compounds. Risk is calculated for each grid cell as follows:

$$\text{Risk}_{i,j} = \Sigma\ \text{Concentration}_{i,j,k} \times \text{Risk Factor}_{i,j,k},$$

Where i,j is the grid cell (easting, northing) and k is the toxic compound. The risk factor for a given compound is derived from its inhalation slope factor following the 2015 OEHAA risk assessment guidelines. In addition to the inhalation exposure, which was the method to estimate cancer risk in the previous MATES, a multiple pathway factor was incorporated in the current cancer risk estimation. The multiple pathway factors include additional cancer risk from oral and dermal exposures from toxic metals.

The grid cell having the highest simulated cancer risk of 990-in-a-million was located near the Ports of Los Angeles and Long Beach. Another grid cell with a high risk value (963-in-a-million) was the grid where the Los Angeles International Airport is located. In addition to the clusters of cells around the seaports and the airport with high risk, a third cluster of high-risk area is centered around a railyard southeast of downtown Los Angeles. In general, as in the past studies, the higher-risk areas tend to be along transportation and goods movement corridors.

Figure IX-7-4 provides the CAMx RTRAC simulated air toxics risk for the MATES IV period. Figure IX-7-5 depicts the changes in risk from MATES IV (2012-2013) to MATES V (2018-2019) estimated from the CAMx RTRAC simulations. The greatest decrease in risk occurred in the ports area, where the peak risk value changed from 2,607 to 990, reflecting the emission reductions from OGV, CHC and other port operations including cargo handling equipment, port

trucks and locomotives. Overall, air toxics risk improved significantly, consistent with air toxic emissions reductions that occurred over the period.

The MATES V period Basin-average population-weighted inhalation-only cancer risk summed for all the toxic components yielded a cancer risk of 424 in a million. The average risk included all populated land cells that reside within the Basin portion of the modeling domain. The MATES IV Basin average inhalation-only risk was 897 per million. Between the MATES IV and MATES V periods, the simulated risk decreased by 53%. The 53% reduction in Basin risk can be attributed to several factors, most notably, changes in diesel emissions between 2012 and 2018. As shown in Chapter 3, the toxic emissions between the two MATES periods decreased by 46%, including the on-road source emissions decreasing by 59% and the off-road source emissions decreasing by 39%. Modeling using the MATES IV emissions with the MATES V meteorology indicates that, under the same meteorological conditions, the risk reduction based on the changes in the emissions between MATES IV and MATES V would have been 49%. Therefore, a small portion of the modeled risk reduction is due to the difference in the meteorological dispersion potential.

Figures IX-7-6a through IX-7-6f depict risk associated with diesel and its specific emissions categories. Figure IX-7-7 provides the risk excluding the contribution of diesel PM. On and off-road diesel impacts are spread throughout the Basin following the transportation corridors and off-road facilities such as the intermodal transfer sites. The shipping impacts are concentrated in the vicinity of the Ports of Los Angeles and Long Beach and the adjacent downwind communities.

Regional risk from non-diesel sources (Figure IX-7-7) is also uniformly distributed throughout the Basin with values typically around 100 -200 in one million, with only a few selected cells showing values exceeding 200 in one million risk.

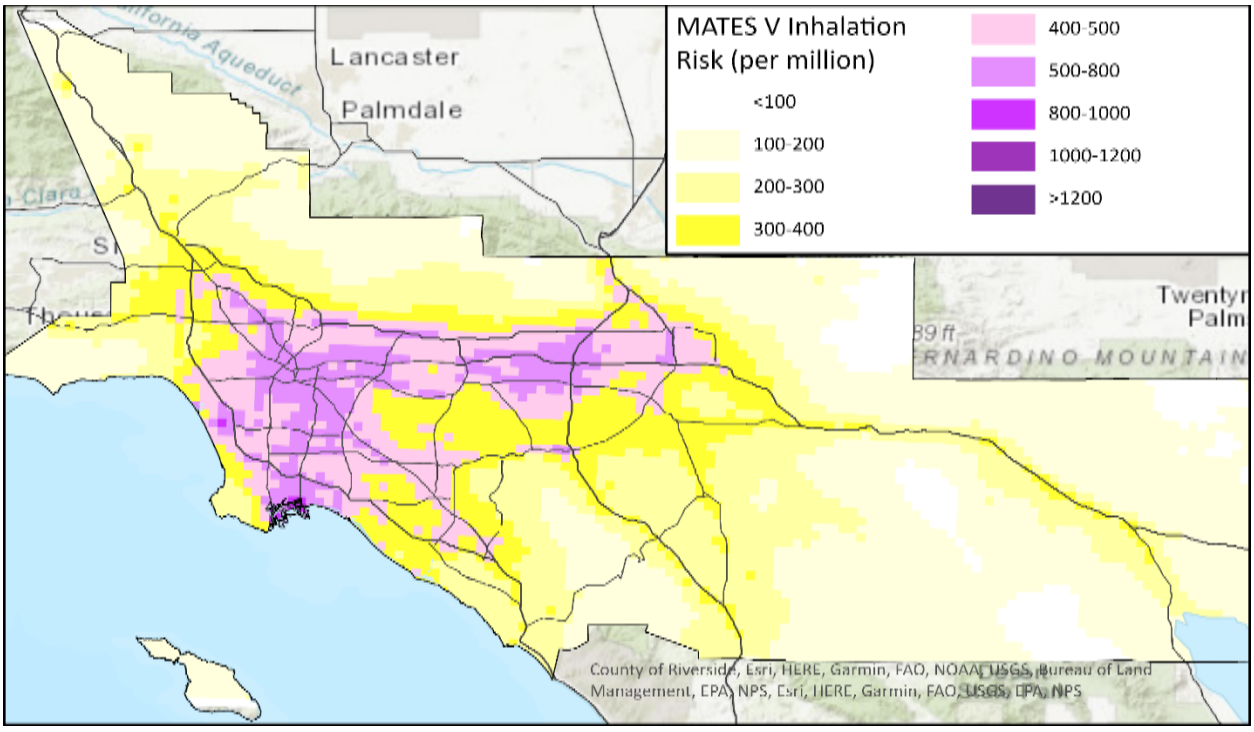

Figure IX-7-3
2018 MATES V CAMx RTRAC Simulated Inhalation Air Toxics Cancer Risk

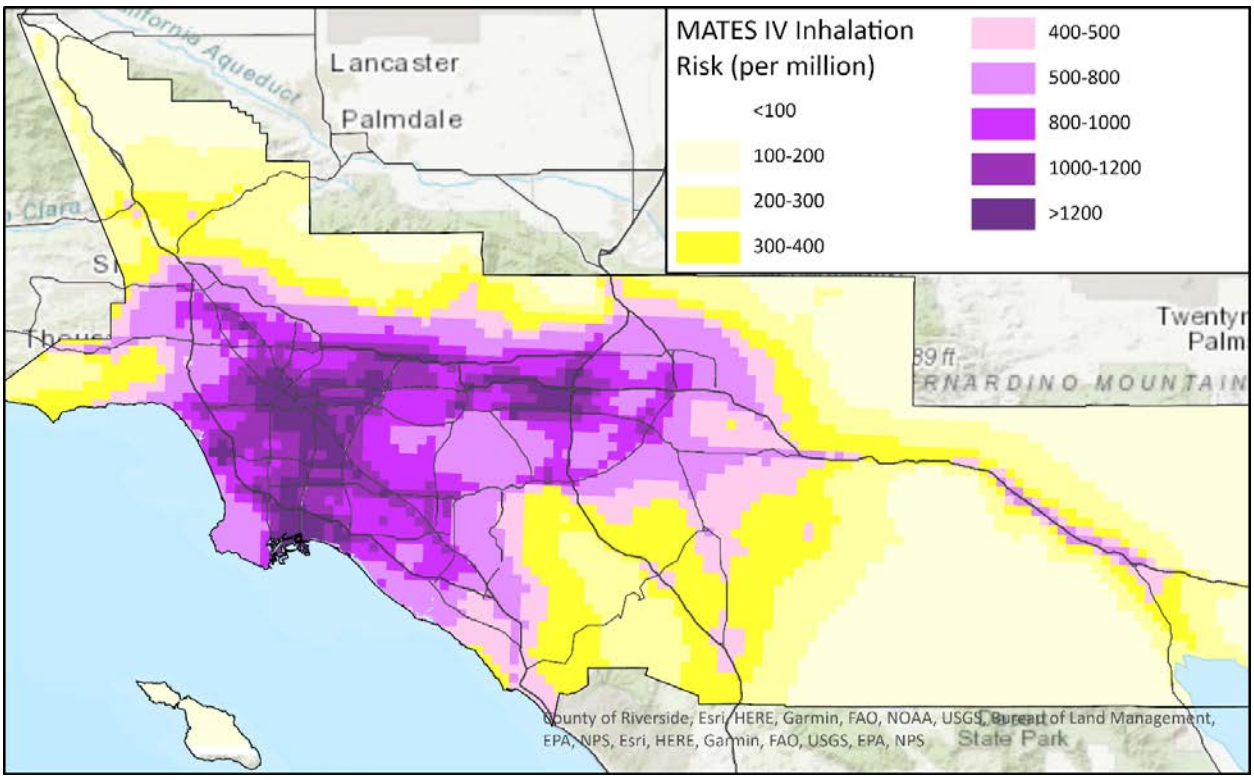

Figure IX-7-4
2012 MATES IV CAMx RTRAC Simulated Inhalation Air Toxics Cancer Risk.

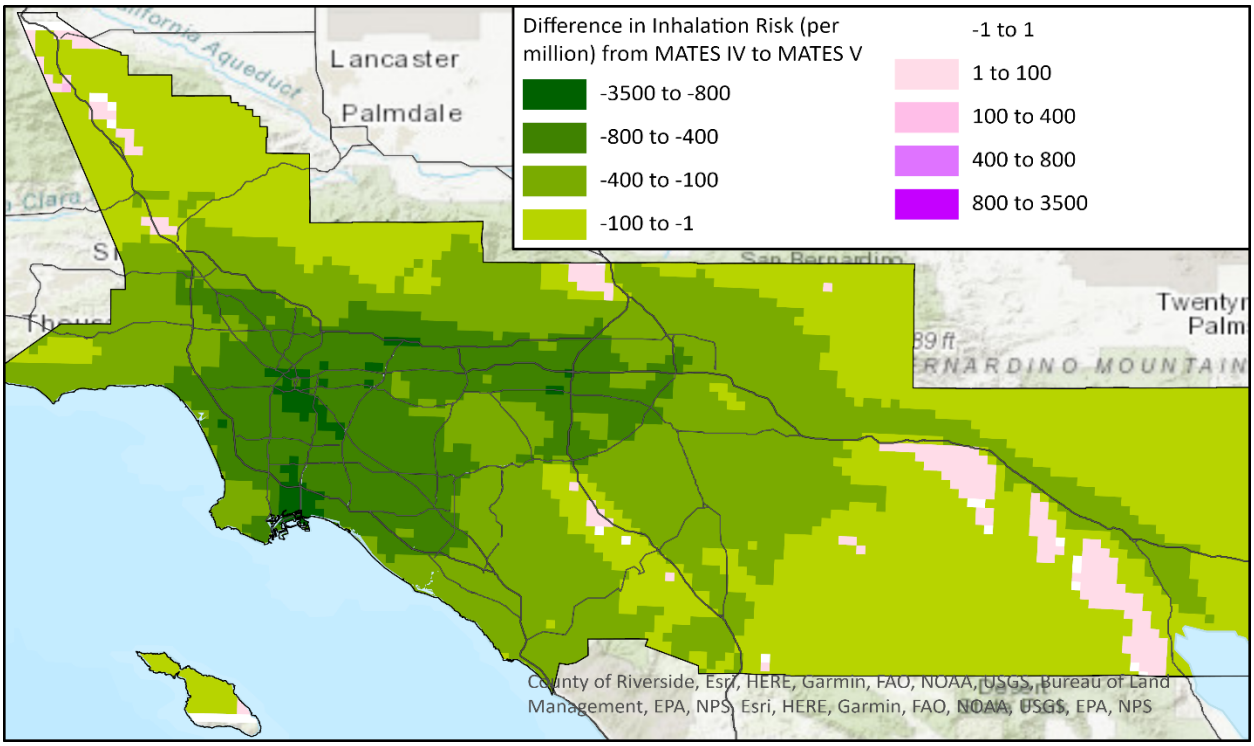

Figure IX-7-5
Change in CAMx RTRAC simulated Inhalation Air Toxics Cancer Risk from 2012 to 2018

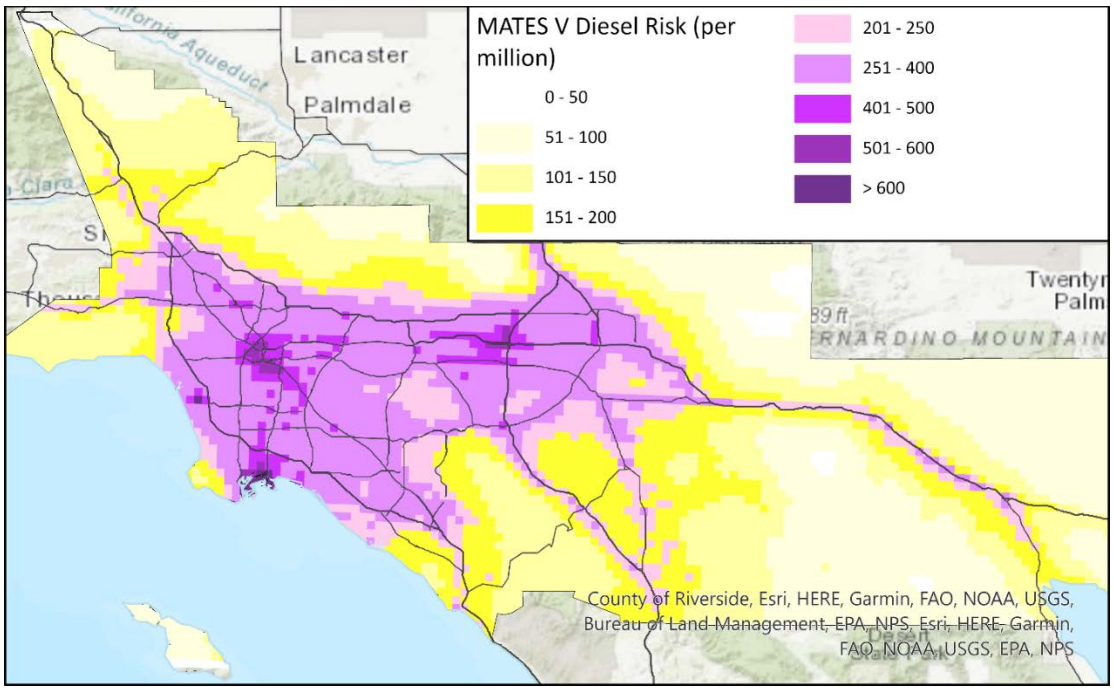

Figure IX-7-6a
MATES V Inhalation Cancer Risk from Diesel PM from All Categories

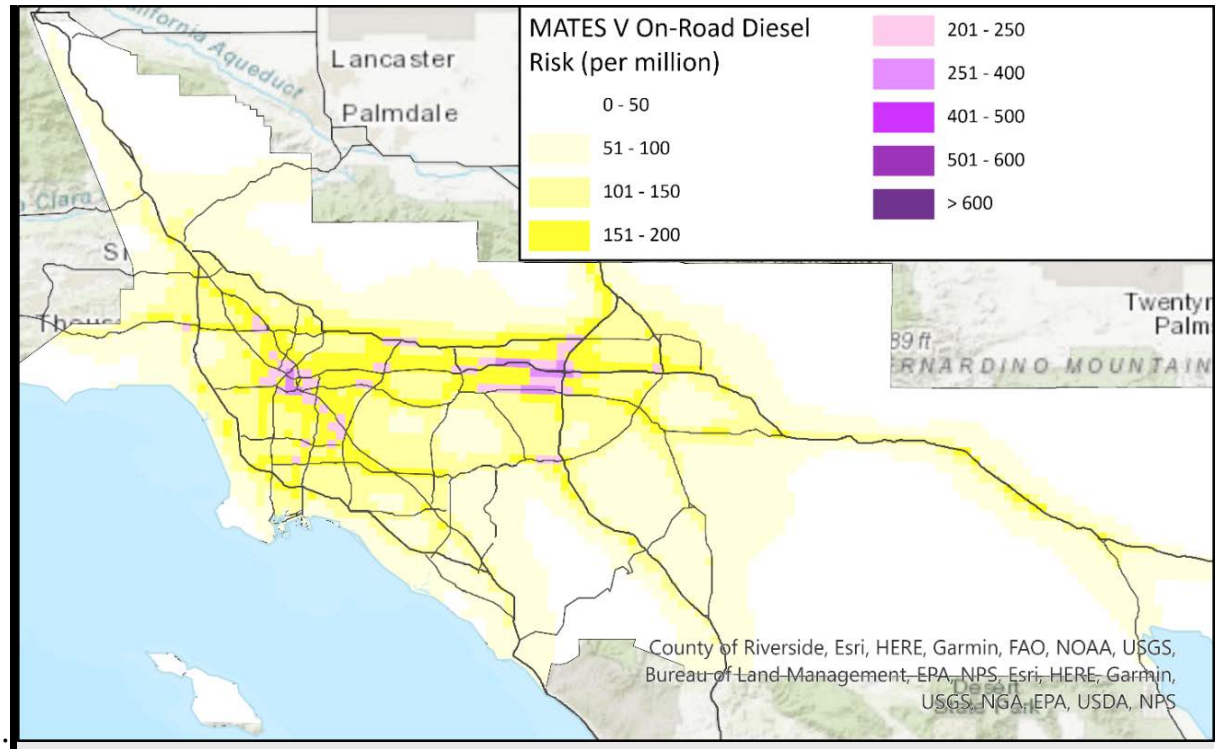

Figure IX-7-6b
MATES V Simulated Inhalation Cancer Risk from On-Road Diesel PM.

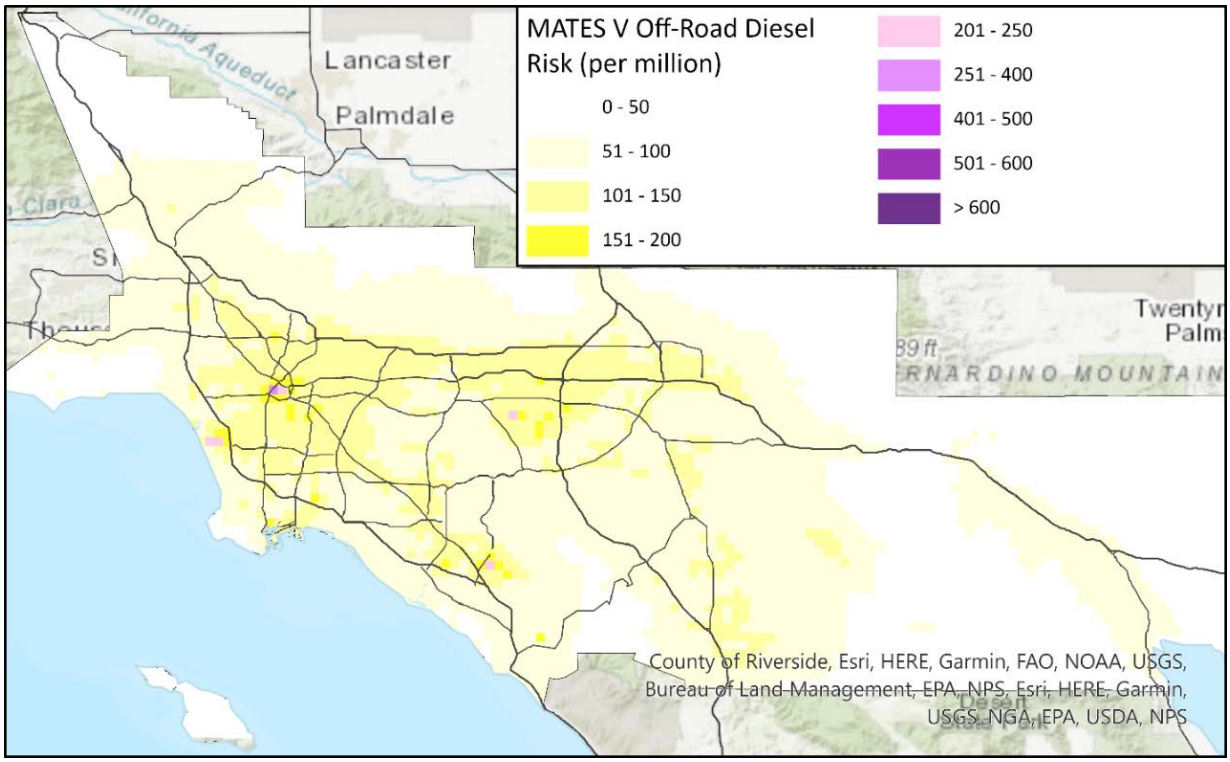

Figure IX-7-6c
MATES V Simulated Inhalation Risk from Off-road Diesel (including railyards but excluding trains and ships).

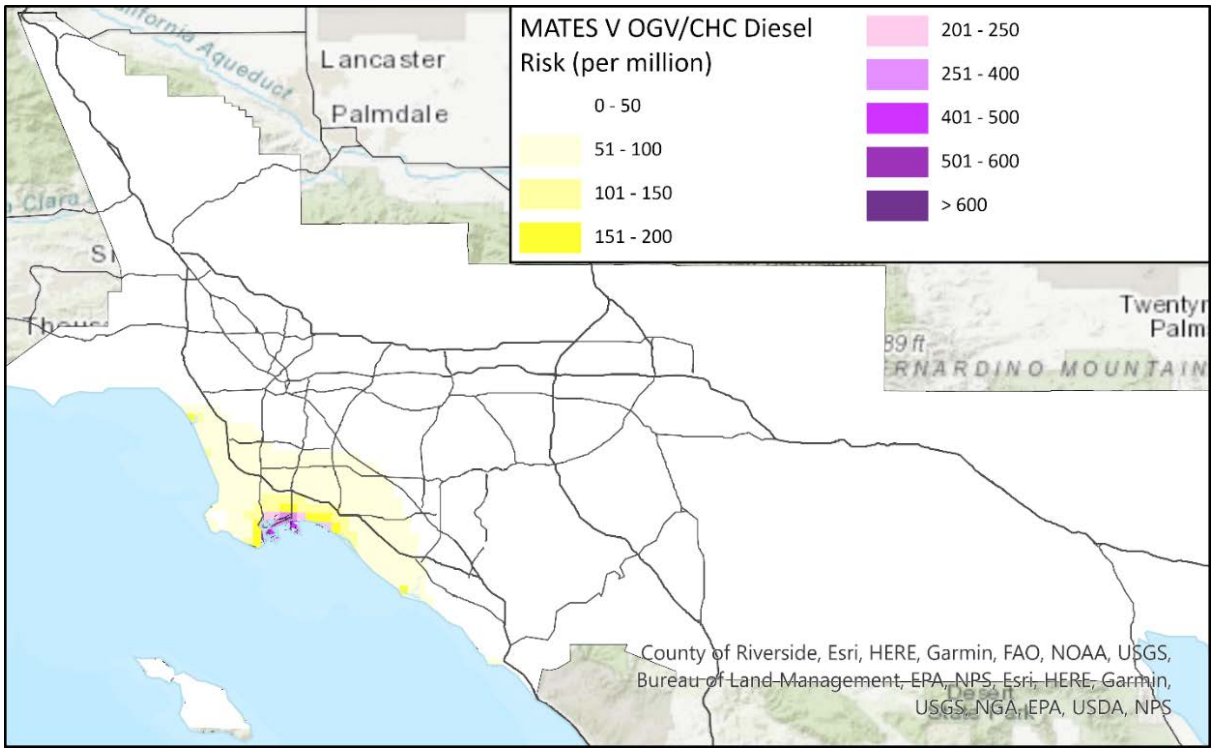

Figure IX-7-6d
MATES V Simulated Inhalation Cancer Risk from Ship Diesel PM.

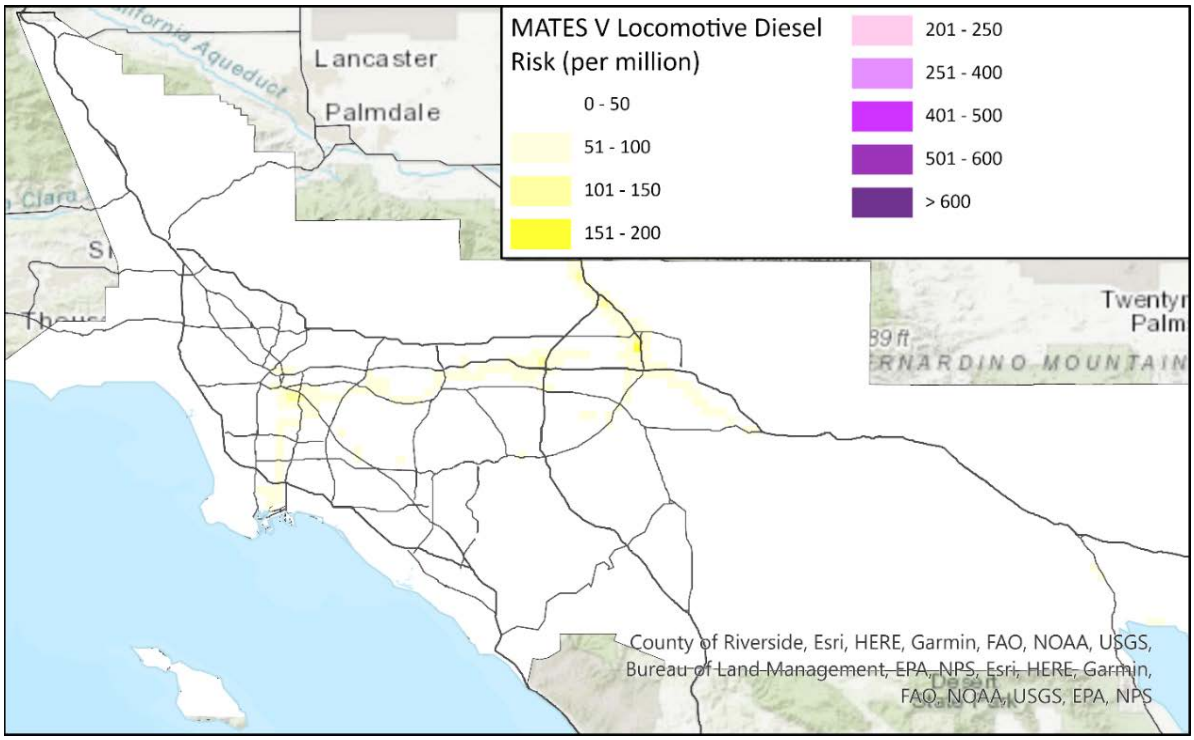

Figure IX-7-6e
MATES V Simulated Inhalation Cancer Risk from Locomotive Diesel PM (Excluding Railyard Equipment).

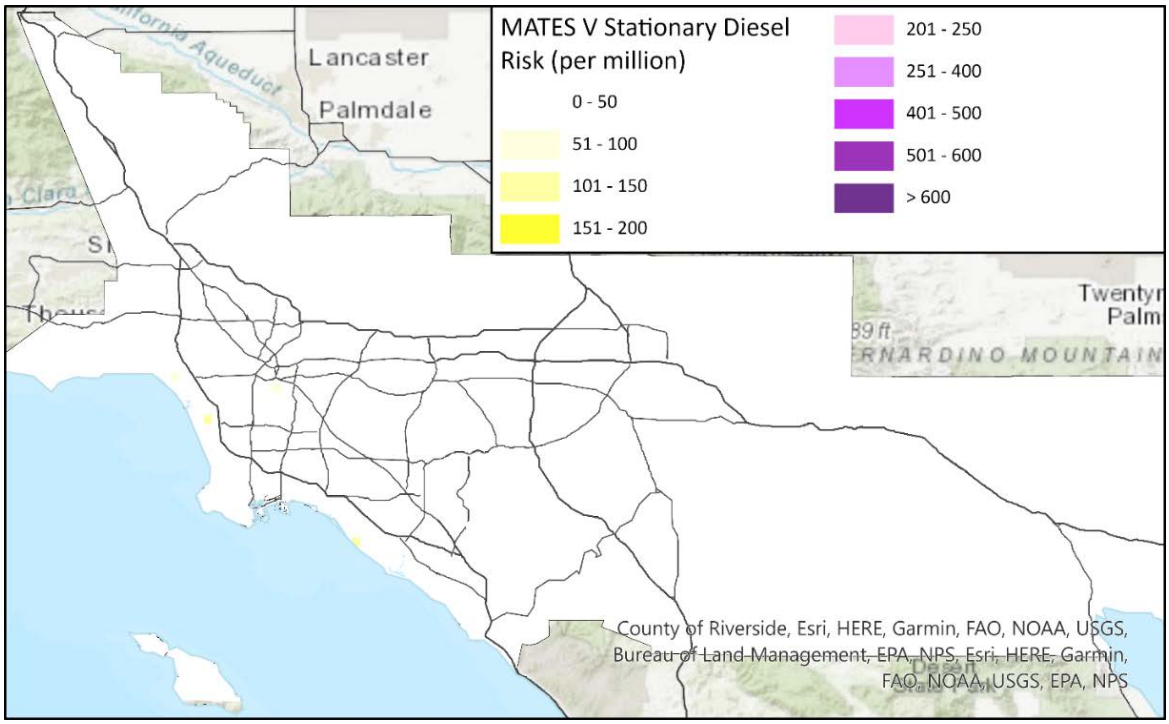

Figure IX-7-6f
MATES V Simulated Inhalation Cancer Risk from Stationary Diesel PM.

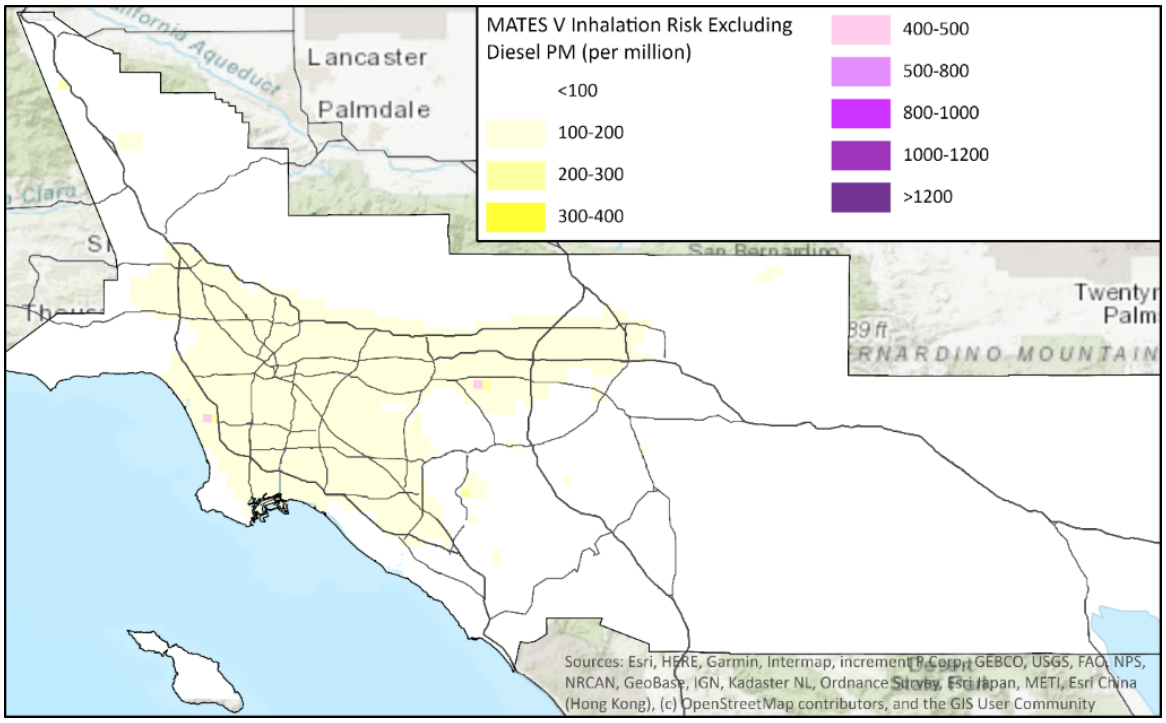

Figure IX-7-7
MATES V Simulated Inhalation Cancer Risk from all air toxics excluding diesel emissions

Figure IX-7-8 provides a close-up plot of the air toxics cancer risk in the Ports area. Table IX-7-7 provides a summary of the air toxics cancer risk estimated for the Basin, for the Ports area, and for the Basin excluding the Ports area. For this assessment, the Ports area includes the populated cells roughly bounded by the Interstate 405 to the north, San Pedro to the west, Balboa Harbor to the east, and Pt. Fermin to the south. The MATES V average population-weighted air toxics risk in the Ports area (as defined above) was 504 in one million. The Basin average population-weighted air toxics risk, excluding the grid cells in the Ports area, was 418 in one million. The downwind impacts resulting from Port area activities are still reflected in the toxics risk estimates for the grid cells categorized as "Basin minus Ports." Similarly, the MATES IV simulations indicated that the Ports area air toxics risk was 1,177 in one million; and the Basin minus the Ports area was 879 in one million. Overall, the Ports area experienced an approximate 57% decrease in risk, while the average population-weighted risk in other areas of the Basin decreased by about 52%.

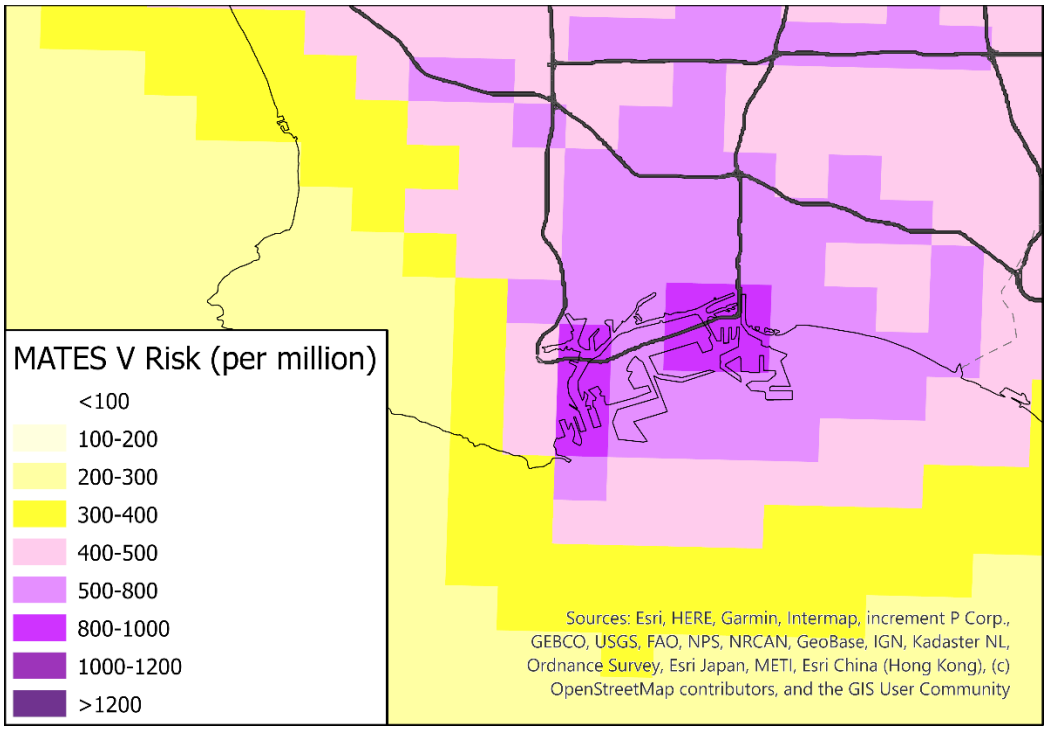

Figure IX-7-8
2018 Ports area MATES V Simulated Inhalation Air Toxics Cancer Risk

Table IX-7-7
Basin and Port Area Population Weighted Inhalation Air Toxics Cancer Risk

Region	MATES IV		MATES V		Average Percentage Change in Risk
	2012 Population	Average Risk (Per Million)	2018 Population	Average Risk (Per Million)	
Basin	15,991,150	897	16,599,786	424	-53
Ports Area	998,745	1,177	1,004,938	504	-57
Basin Excluding Ports Area	14,992,806	879	15,994,848	418	-52

IX.7.6 County Risk Assessment

Table IX-7-8 provides the county-by-county air toxics risk to the affected population. As presented in the spatial distribution, the Basin portion of Los Angeles County bears the greatest average cancer risk at 470 per one million. The Basin portion of San Bernardino County has the second highest projected risk at 449 per one million. The estimated risk for Orange County is 379 per million, and the Basin portion of Riverside County was estimated to have the lowest population-weighted risk at 321 per million. As expected, the Coachella Valley portion of Riverside County, which is outside of the Basin, has the lowest toxic risk at 241 per million. It should be noted that these are county-wide averages, and individual communities could have higher risks than the average if they are near emissions sources, such as railyards or intermodal facilities.

Comparison of the county-wide population-weighted risk shows that the greatest reduction occurred in Los Angeles County, with the amount of risk reduction per county being similar. Reductions in emissions from mobile sources including benzene, 1,3-butadiene, and diesel particulate are the primary contributors to the improved county-wide risk.

Table IX-7-8
County-Wide Population-Weighted Air Toxics Cancer Risk (Inhalation Only)

Region	MATES IV		MATES V		Average Percentage Change in Risk
	2012 Population	Average Risk (Per Million)	2018 Population	Average Risk (Per Million)	
Los Angeles*	9,578,586	1015	9,846,922	462	-54
Orange	3,067,909	770	3,223,763	365	-53
Riverside*	1,784,872	543	1,912,855	313	-42
San Bernardino*	1,560,183	827	1,616,247	439	-47
Basin	15,991,550	897	16,599,786	424	-53
Coachella Valley	465,064	339	479,055	239	-30

* Including the Basin portion only

IX.7.7 Risk from Key Compounds

Table IX-7-9 provides the Basin average breakdown of risk associated with each of the key compounds simulated in the analysis. Diesel particulate ranked highest (70%) as the toxic compound contributing to the overall inhalation cancer risk to the population. The next three highest contributors included benzene, 1,3-butadiene and formaldehyde. The four top toxic pollutants contribute over 90% toxic risk. Formaldehyde (primary and secondary) and acetaldehyde (primary and secondary) contribute 6% and 1.6%, respectively, while the remaining compounds combined accounted for less than 7% of the total.

Table IX-7-9
MATES V Inhalation Cancer Risk from Simulated Individual Toxic Air Contaminants

Toxic Compound	Risk Factor (µg/m^3)	Max Annual Average Concentration	Population Weighted Annual Average Concentration	Units	Risk (per million)	% Contribution
DPM	7.40E-04	1.13	0.41	µg/m$_3$	306.30	72.3
Benzene	6.80E-05	0.42	0.14	ppb	46.87	11.1
Formaldehyde	1.40E-05	3.60	1.49	ppb	25.78	6.1
1,3- Butadiene	4.10E-04	0.44	0.03	ppb	12.90	3.0
Hexavalent Chromium	3.50E-01	0.00025	2.01E-05	µg/m 3	7.13	1.7
Acetaldehyde	6.80E-06	1.02	0.55	ppb	6.82	1.6
Cadmium	1.00E-02	0.019	4.69E-04	µg/m$_3$	4.08	1.0
p-Dichlorobenzene	2.70E-05	0.07	2.37E-02	ppb	3.86	0.9
Arsenic	8.10E-03	0.029	5.89E-04	µg/m$_3$	3.00	0.7
Perchloroethylene	1.40E-05	0.10	2.06E-02	ppb	1.97	0.5
Nickel	6.20E-04	0.18	2.82E-03	µg/m$_3$	1.78	0.4
Naphthalene	8.10E-05	0.025	3.46E-03	ppb	1.48	0.3
Methylene Chloride	2.40E-06	0.77	0.15	ppb	1.29	0.3
Trichloroethylene	4.70E-06	0.08	8.34E-03	ppb	0.21	<0.1
Lead	2.80E-05	0.038	3.21E-03	µg/m$_3$	0.08	<0.1

IX.7.8 Network Risk Evaluation

Table IX-7-10 provides the simulated air toxics risk at each of the 10 stations for the top three toxic compounds and the remaining aggregate contributing to the overall risk. Risk is calculated using each toxic component concentrations predicted for the specific monitoring station location. The model prediction comparison used the nine-cell average at the grid corresponding to a monitoring station and its surrounding 8 grid cells using an inverse distance squared weighting factor. The summary also provides the comparison between simulated average risk for the 10 stations and the average risk calculated using the annual toxic compound measurements. Since diesel PM cannot be measured directly, measurement-based risk is calculated using an $EC_{2.5}$ to diesel PM conversion as described in Chapter 2 to estimate the diesel PM contributions. The comparison to measured risk was conducted with the 7 stations which are listed in the previous section

Among the monitored locations, the highest risk was simulated in Central Los Angeles followed by West Long Beach and Huntington Park. The lowest modeled risk was simulated at Rubidoux. With diesel PM reductions in port operations, the West Long Beach is no longer the highest risk site as it was in the previous MATES. Additionally, the modeled risk at the Long Beach station is below the overall average risk across all stations, although the location of the Long Beach station was relocated from an area near the I-710 to a mostly residential location southeast of the previous location. The MATES V monitoring with the highest air toxics cancer risk was Inland Valley San Bernardino. This inland location is located in an area near major goods movement land uses.

Table IX-7-10
Modeled Inhalation Cancer Risk at Monitoring Locations and Measured Risk

Location	MATES V CAMX RTRAC Simulation				
	Benzene	1,3-Butadiene	Diesel	Others	Total
Anaheim	49	14	307	56	426
Burbank Area	58	16	381	72	526
Central Los Angeles	65	21	499	82	667
Compton	53	15	381	70	519
Inland Valley San Bernardino	46	12	362	86	506
Huntington Park	57	20	408	75	559
Long Beach	52	16	359	65	492
Pico Rivera	50	11	368	63	492
Rubidoux	39	9	295	48	390
West Long Beach	60	20	455	80	615
10-Station Average Modeled	53	15	382	70	519
7-station+ Averaged Modeled	54	16	387	73	530
7-Station+ MATES V Average Measured*	62	56	362	114	593

*Including modeled species only, Risk from some measured species, such as carbon tetrachloride, chloroform and PAHs are excluded. Measured $EC_{2.5}$ was converted diesel PM as described in the Chapter 2.

+ Among the 10 monitoring stations, 3 stations, Anaheim, Los Angeles and Rubidoux do not have complete data. Therefore 7-station averages are used.

Based on modeled concentrations, the inhalation-only air toxics cancer risk averaged over the 7 stations is 530-in-a-million, which is approximately 11% lower than the measurement-based risk as shown in Figure IX-7-9a.

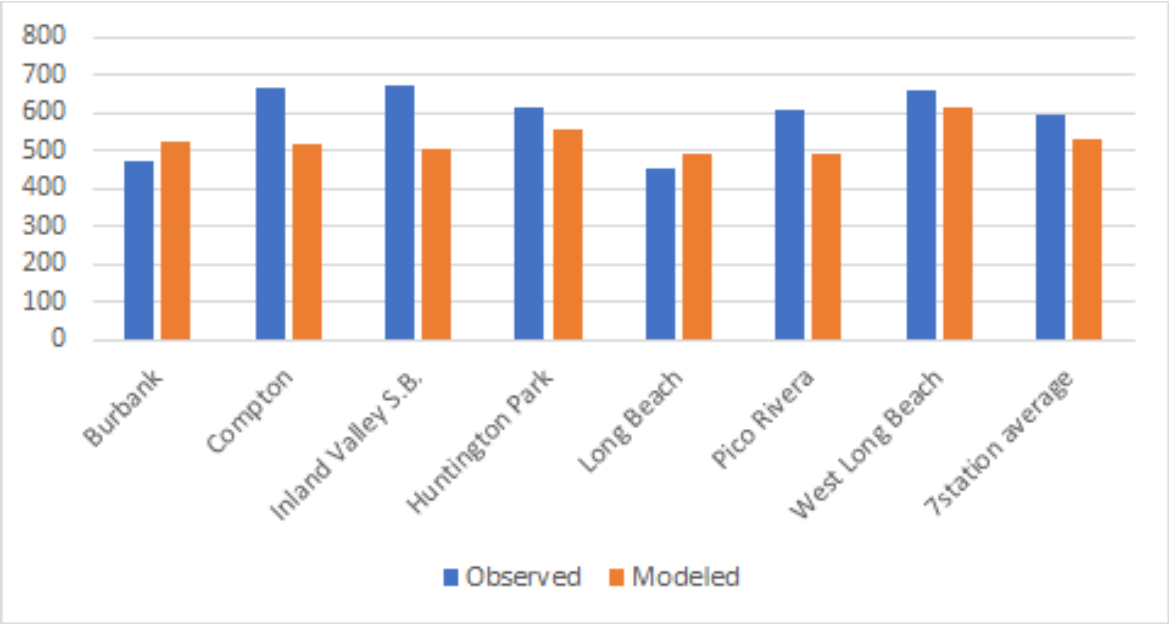

Figure IX-7-9a
MATES V Modeled vs. Measured Inhalation Air Toxics Cancer Risk (Per Million)

The portion of the simulated cancer risk attributed to air toxics other than diesel PM can be directly compared to risk calculated from the toxic compound measurements. Figure IX-7-9b presents a comparison of the model simulated and measurement-based non-diesel risk at each monitoring site, as well as the 7-station average. The modeled non-diesel risk at each station is 27 to 50% lower than the risk calculated based on measurement data, with the modeled 7-station average cancer risk being 39% lower than the measurement-based risk. This difference in non-diesel risk is primarily due to underprediction of concentrations of formaldehyde, acetaldehyde and 1,3-butadiene and, to a lesser extent, benzene.

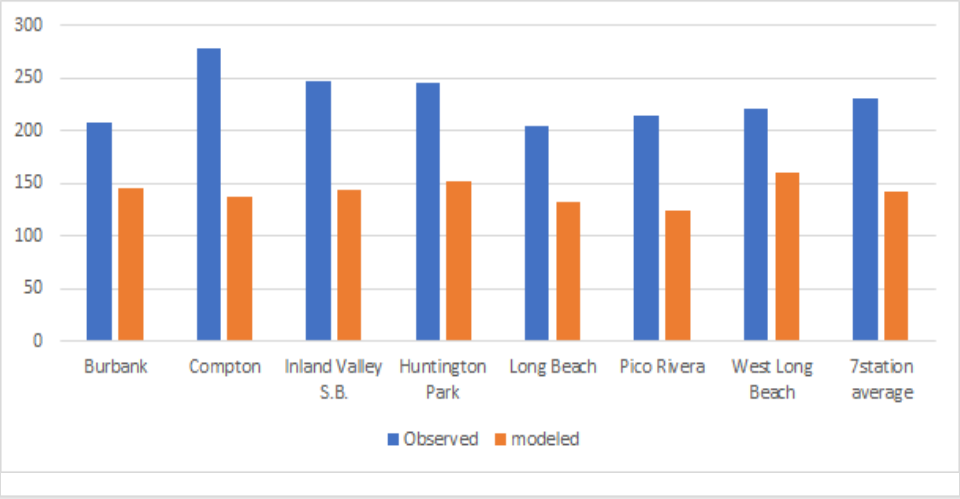

Figure IX-7-9b
MATES V Simulated vs. Measured Non-Diesel Air Toxics Risk (per million)

IX.7.9 Multiple-Pathway Cancer Risk

The cancer risk discussed in the previous section was based on inhalation exposure only, which was the practice used in previous MATES studies. Among the toxic species included in the modeling, arsenic, hexavalent chromium and lead have associated cancer risks from non-inhalation exposures. This additional cancer risk can be assessed by a multiple-pathway factor. For arsenic, hexavalent chromium and lead, the multiple-pathway factors are 9.71, 1.6 and 11.41, respectively. These factors account for oral and dermal exposures for these toxic metals. The overall multiple-pathway risk due to the inclusion of the three metals was estimated to be 455 per million, which is approximately 7.3% higher than the inhalation-only risk. Table IX-7-11 lists average risks for individual county and Coachella Valley. Figure IX-7-10 depicts the MATES V distribution of multiple-pathway cancer risk estimated from the predicted annual average concentrations of the modeled toxic compounds. Compared to Figure IX-7-3, where only inhalation toxic risk is depicted, additional risk from oral exposure of arsenic, hexavalent chromium and lead elevated the overall risk in some areas. County-wide and air basin level population weighted cancer risks are compared to MATES IV modeling results in Table IX-7-12. The reduction in the multiple-pathway risk is similar to the inhalation-only risk trends as shown in Table IX-7-8.

Table IX-7-11
County-Wide Population-Weighted Air Toxics Cancer Risk for Inhalation-Only and for Multiple-Pathway Factors

Region	2018 Population	Inhalation-Only	Multiple-Pathway
		Average Risk (Per Million)	Average Risk (Per Million)
Los Angeles*	9,846,922	462	497
Orange	3,223,763	365	390
Riverside*	1,912,855	313	332
San Bernardino*	1,616,247	439	471
Basin	16,599,786	424	455
Coachella Valley	479,055	239	250

* Data for these counties reflects the South Coast Air Basin portion only. Please note that all of Orange County is within the South Coast Air Basin.

*

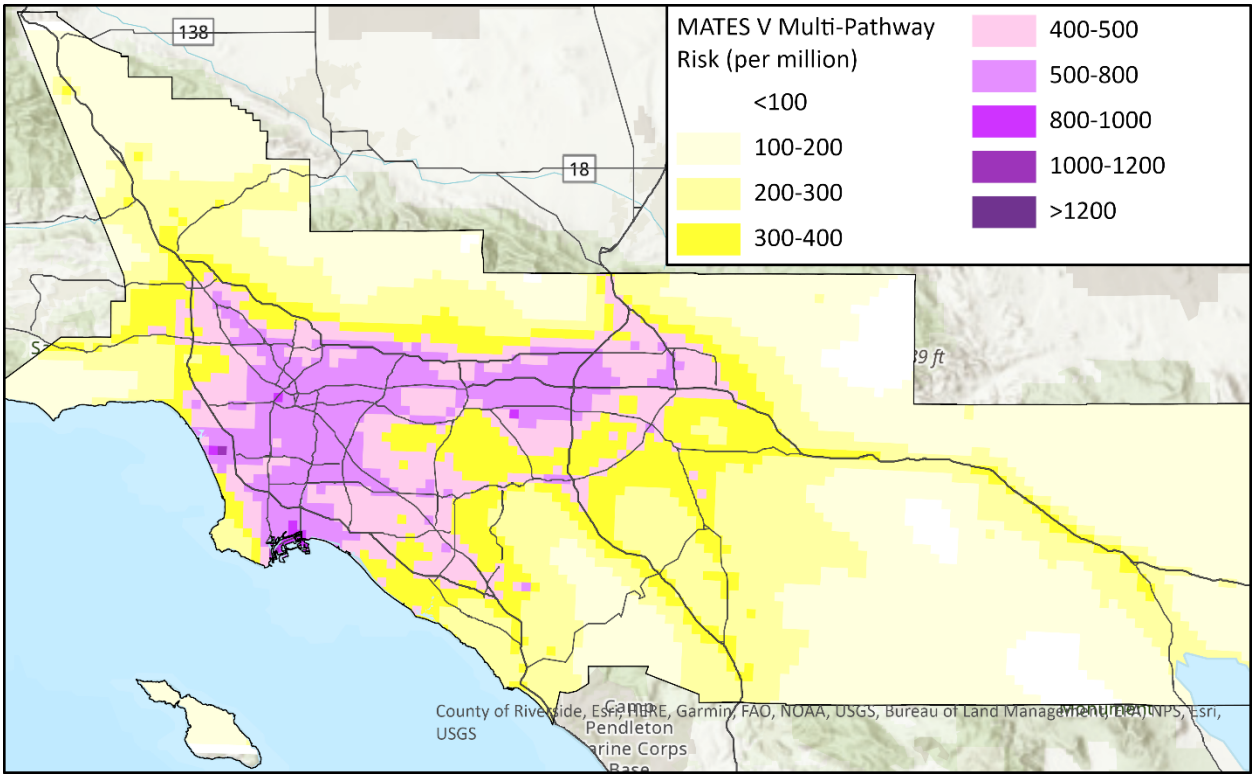

Figure IX-7-10
MATES V CAMx RTRAC Simulated Multiple-Pathway Air Toxic Cancer Risk

Table IX-7-12
County-Wide Population-Weighted Multiple-Pathway Cancer Risk

Region	MATES IV		MATES V		Average Percentage Change in Risk
	2012 Population	Average Risk (Per Million)	2018 Population	Average Risk (Per Million)	
Los Angeles*	9,578,586	1143	9,846,922	497	-57%
Orange	3,067,909	829	3,223,763	390	-53%
Riverside*	1,784,872	586	1,912,855	332	-43%
San Bernardino*	1,560,183	905	1,616,247	471	-48%
Port Area	998,745	1293	1,004,938	559	-57%
Basin Excluding Port Area	14,992,806	978	15,994,848	448	-54%
South Coast Air Basin	15,991,550	997	16,599,786	455	-54%
Coachella Valley	465,064	357	479,055	250	-30%

* Data for these counties reflects the South Coast Air Basin portion only. Please note that all of Orange County is within the South Coast Air Basin.

IX.8 Summary and Conclusions

A regional photochemical modeling system including CAMx with RTRAC algorithm, WRF, MEGAN and mobile source emissions model was employed to simulate air toxics cancer risk for the MATES V study. The population-weighted average Basin air toxics cancer risk is simulated to be 424 per million for inhalation-only risk and 455 per million for multi-pathway risk. The areas of the Basin that are exposed to the higher risk continue to be along the goods movement corridors. The MATES V inhalation-only cancer risk is estimated to be 53% lower than the corresponding risk during the MATES IV period, which was 897 in a million. Much of the risk reduction was due to the reductions of diesel particulate emissions which showed a 51% reduction from 2012 to 2018. The changes of other toxic compounds emissions marginally contribute to the overall reduction in the MATES V simulated risk. Overall carcinogenic emissions during the MATES V period are lower than the MATES IV by 46%. The simulated risk showed a greater rate of reduction than the corresponding risk derived from measurements, which showed 31% reduction since MATES IV.

IX.9 References

Byun, D.W., and Ching, J.K.S. (1999). Science Algorithms of the EPA Models-3 Community Multiscale Air Quality (CMAQ) Modeling system, U.S. Environmental Protection Agency, EPA/600/R-99/030

California Air Resources Board (CARB) (2017). EMission FACtor (EMFAC) 2017 model and its documentation can be obtained at the following link: http://www.arb.ca.gov/msei/modeling.htm

California Air Resources Board (CARB) (2018). SIP Update can be viewed or downloaded from the following CARB link: https://ww2.arb.ca.gov/resources/documents/2018-updates-california-state-implementation-plan-2018-sip-update

California Air Resources Board (CARB), (2020), Workshop on emissions inventory from small off-road engines (SORE). . https://ww2.arb.ca.gov/sites/default/files/2020-03/SORE2020%20Workshop%20Slides%20March%2025%202020_03302020_ADA_v2.pdf

ENVIRON, Inc.(2005). "METSTAT software for MM5 version 3 (02/11/05)," ENVIRON. Novato, CA 94945, http://www.camx.com/down/support.php

ENVIRON, Inc. (2006). "KVPATCH software for CAMx," ENVIRON. Novato, CA 94945, http://www.camx.com/down/support.php

Hong, S.-Y., and H.-L. Pan (1996). Nonlocal boundary layer vertical diffusion in a medium-range forecast model. Mon. Wea. Rev., 124, 2322–2339, doi:10.1175/1520-0493(1996)124,2322

Grell, G.A., Dudhia, J., Stauffer, D.R. (1994). A Description of the Fifth-Generation Penn State/NCAR Mesoscale Model (MM5), NCAR/TN-398+STR, NCAR Technical Note

Mason, R., Dolwick, P., Carey, P., Kinnee, E., Wilson, M. (2008). Emissions processing and sensitivity air quality modeling of category 3 commercial marine vessel emissions. In: Proceedings from 17th Annual International Emission Inventory Conference, Portland, OR.

O'Brien, J.J. (1970). A note on the vertical structure of the eddy exchange coefficient in the planetary boundary layer. J. Atmos. Sci., 27, 1213-1215

Ranboll Environment and Health. (2018). CAMx User's Guide Version 6.50. Novato, CA 94998. Available at https://camx-wp.azurewebsites.net/Files/CAMxUsersGuide_v6.50.pdf

Skamarock, W.C., Klemp, J.B., Dudhia, J., Gill, D.O., Barker, D.M., Duda, M.G., Huang, X.-Y., Wang, W., Powers, J.G. (2008). A Description of Advanced Research WRF version 3. NCAR/TN-475+STR, NCAR Technical Note

Southern California Association of Governments (SCAG) (2016). Information on the Southern California Association of Governments 2016 RTP/SCS Available at 2016-2040 RTP/SCS Transportation Conformity Determination - Southern California Association of Governments, https://scag.ca.gov/sites/main/files/file-attachments/f2016rtpscs.pdf?1606005557

South Coast Air Quality Management District (AQMD) (2000). MATES II Documents Available at http://www.aqmd.gov/home/air-quality/air-quality-studies/health-studies/mates-ii

South Coast Air Quality Management District (AQMD), (2008). MATES III Documents Available at https://www.aqmd.gov/home/air-quality/air-quality-studies/health-studies/mates-iii

South Coast Air Quality Management District (AQMD) (2015). MATES IV Documents Available at https://www.aqmd.gov/home/air-quality/air-quality-studies/health-studies/mates-iv

South Coast Air Quality Management District (AQMD) (2016). Air Quality Management Plan. Document available at https://www.aqmd.gov/home/air-quality/clean-air-plans/air-quality-mgt-plan/final-2016-aqmp

South Coast Air Quality Management District (AQMD) (2020). Draft Final South Coast Air Basin Attainment Plan for 2006 24-Hour PM2.5 Standard. Available at: http://www.aqmd.gov/docs/default-source/clean-air-plans/air-quality-management-plans/2022-air-quality-management-plan/draft-final-south-coast-air-basin-pm2-5-plan-110320.pdf?sfvrsn=6

U.S. EPA (2006). Guidance on Use of Modeled and Other Analyses for Demonstrating Attainment of Air Quality Goals for Ozone, $PM_{2.5}$ and Regional Haze NAAQS, U.S. EPA, Office of Air Quality Planning and Standards, Emissions, Monitoring, and Analysis Division, Air Quality Modeling Group, Research Triangle Park, North Carolina, September, 2006

WRAP (2007). Western Regional Air Partnership, Technical Support System, Emissions Method, Offshore Emissions, http://vista.cira.colostate.edu/